INVESTIGATION OF PHOTONIC CRYSTAL NANOBEAMS FOR RESONATOR COUPLING, MODAL FINGERPRINTING AND WAVELENGTH FILTERING

By

Francis O. Afzal

Dissertation

Submitted to the Faculty of the

Graduate School of Vanderbilt University

in partial fulfillment of the requirements

for the degree of

DOCTOR OF PHILOSOPHY

in

Electrical Engineering

December 12, 2020

Nashville, Tennessee

Approved:

Professor Sharon Weiss

Professor Joshua Caldwell

Professor Justus Ndukaife

Professor Jason Valentine

Professor Yaqiong Xu

To Sharon and Madison,

for challenging me to grow and supporting me along the way.

ACKNOWLEDGMENTS

This PhD work is the product of efforts exerted by a team which propelled my own ideas from hypothesis to thesis. While I had the privilege of leading the projects in this thesis, none of this work would be possible without the support I received along the way. For fabrication and characterization, I received monumental support from the staff at the Vanderbilt Institute of Nanoscale Engineering (VINSE) and at the Center for Nanophase Materials Sciences (CNMS) at Oak Ridge National Labs (ORNL). For my work on sub-wavelength grating filters, our collaborators at GlobalFoundries consistently promoted and supported my idea to explore this type of photonic device, resulting in designs being placed on a tapeout within days of me showing my manager simulation results and experimental measurements being taken days after hardware was available.

While our collaborators and the community at Vanderbilt played essential roles in my success, the single greatest resource I have had during my graduate studies was my advisor, Sharon Weiss. Sharon, in my mind, has demonstrated herself to be an exemplary graduate advisor and provided me with everything I needed to grow and succeed while I was conducting research. While I would like to discuss each contribution she made to my PhD, the comprehensive list of ways Sharon provided for me during my PhD is too long for a reasonable acknowledgments section. In lieu of this, I want to list some highlights of how Sharon supported me:

- She advocated for me during the recruitment process, helping me secure both IBM and HSV topping awards for my funding
- She coached me through the NSF GRFP application process, helping me secure an NSF fellowship which funded me generously for 3 years in graduate school
- She challenged me throughout my graduate career with difficult projects to build up my technical skills, but allowed me to control the direction of my research when I had other ideas I wanted to pursue

- She encouraged me to actively participate in conferences and fully funded my travel expenses, landing me a talk at SPIE, 3 talks at CLEO, 2 poster presentations at the CNMS user meeting, a poster at GlobalFoundries and a poster at VINSE NanoDay
- She allowed me the freedom to actively organize and lead my own outreach event with Overton High School and helped connect me with people who could support this project
- She included me in many of her classes, allowing me to both teach lessons she had created and design new lessons of my own
- She included me in an industry collaboration with Sensera Inc., giving me the opportunity to better understand industry work, network and design devices I was unfamiliar with
- She secured an internship for me with GlobalFoundries, allowing me to prove myself in the industry setting, network and better understand the photonics industry

Perhaps the most important part of working in Sharon's lab was that I felt like I could be myself while doing research. While a few of my personality traits may set off red flags for work ethic, Sharon respected that I had a life and hobbies outside of graduate school, and let my participation and results determine my dedication to research. In line with this, I have to thank all the graduate students that had to put up with me, both those senior graduate students who I made answer too many questions, and the younger ones, who also had to deal with me asking too many questions. I had a wonderful time doing research with all of you and I wish you the very best.

TABLE OF CONTENTS

LIST OF TABLES

LIST OF FIGURES

Chapter 1

Introduction

The interaction between light and matter has facilitated the realization of many modern technologies such as solar cells [1, 2], optical data communication [3], optical tweezers [4, 5], and optical biosensors [6]. By furthering our understanding on how light and matter interact, we are not only able to enhance existing technologies but also may enable the development of novel optical devices. In addition to commercially available products, state of the art technologies such as optical cloaks [7, 8], advanced lenses [9, 10], on-chip lasers [11, 12], optomechanical resonators [13, 14] and passive cooling elements [15, 16] have all resulted from an increased knowledge of how light and matter affect one another.

Among the devices which have been used to affect optical fields and enhance light-matter interaction, photonic crystals have demonstrated great potential for enhancing light-matter interaction at the nano-scale through optical resonances [17, 18]. A subset of photonic crystal devices, photonic crystal nanobeams (PCNs), have demonstrated similarly large enhancements in a compact device footprint (on the order of $\sim 10\mu m^2$) [19, 20].

1.1 Overview of Thesis

The work in this thesis focuses on how to efficiently implement evanescently coupled PCNs, characterize mode order in PCN cavities via resonant scattering, and apply PCNs as add/drop filters for optical signal processing. Chapter 1 introduces the concept of increasing the interaction between light and matter, relevant work on nanophotonic resonators, its applications and how photonic crystals can be utilized as a platform for enhanced light-matter interaction. Chapter 2 discusses how to implement PCN cavities in a side-coupled configuration for optimal device performance. Chapter 3 outlines how measurement of resonant scattering from optical cavities can be used to identify mode order and improve signal to noise ratio (SNR) of resonance detection

via demonstration of concept in a photonic crystal nanobeam. Chapter 4 demonstrates for the first time the use of a type of PCN, referred to as subwavelength gratings (SWGs), as thermally tunable, O-band, add/drop filters in a monolithic photonics technology. Appendix A goes into greater detail how the work in this thesis was conducted and provides some guidance to future graduate students either hoping to continue this work or pursue other research in nanophotonic devices.

1.2 Enhancing Light-Matter Interaction

Many applications are dependent on the interaction between light and matter. Photovoltaics [1, 2, 21], photochemistry [22], optical signal processing [23, 24], optical nanomanipulation [4, 5], optical biosensing [6], lasers [11, 25], and quantum optical information [26] processing all hinge on the ability to control light. In these applications, increasing the time the light and matter have to interact or confining light to a small region inside a material can improve performance. This may be achieved by confining optical fields in time and in space. In 1964, Edwin M. Purcell proposed that the enhancement of spontaneous emission of an atom inside of a resonant cavity could be represented by the equation

$$f = \frac{3Q\lambda^3}{4\pi^2 V_m}, \tag{1.1}$$

where Q is the quality factor of the resonator and V_m is the mode volume of the resonance mode [27]. In general, the quality factor, Q, and mode volume, V_m, are metrics which quantify the temporal and spatial confinement of optical fields by nanophotonic devices. While it is likely Purcell did not intend this equation to be as generally utilized to describe the increase in interaction between light and matter by an optical cavity, as it is today, it is now commonly agreed that the ability to enhance light-matter interaction is dependent on the ratio Q/V_m.

In order to quantify the potential of an optical platform to enhance light matter interaction, we must understand how to compute both the quality factor, Q, and mode volume, V_m, of a resonator. The quality factor of a resonator, Q, can be expressed as

$$Q = \omega_{res}\tau, \tag{1.2}$$

where ω_{res} is the angular resonance frequency of the optical cavity and τ is the lifetime of resonant photons in the cavity. The quality factor can be measured in experiment through the observation of Lorentzian resonance features from transmission of light through the cavity or reflection of light from the cavity. The Lorentzian line shape can be utilized to calculate the Q of the cavity by computing

$$Q = \frac{\omega_{res}}{\Delta\omega} = \frac{\lambda_{res}}{\Delta\lambda} - \frac{\Delta\lambda}{4\lambda_{res}} \approx \frac{\lambda_{res}}{\Delta\lambda}, \text{ for } \lambda_{res} \gg \Delta\lambda \tag{1.3}$$

where $\Delta\omega$ is the full-width-at-half-maximum (FWHM) of the Lorentzian resonance peak in frequency space, λ_{res} is the resonance wavelength and $\Delta\lambda$ is the full-width-at-half-maximum (FWHM) of the Lorentzian resonance peak in wavelength space. If the quality factor of the resonator is sufficiently high (> 10), we may accurately compute the resonator's quality factor from data in either wavelength space or frequency space.

The mode volume of a resonator, V_m, in its general form is still a debated topic despite its reference in Purcell's short letter over half a century ago [28, 29]. It is, however, agreed that for high Q resonators with modes well confined in a finite volume that the mode volume can be calculated by the following equation:

$$V_m = \frac{\int \varepsilon(\vec{r}) \left|\vec{E}(\vec{r})\right|^2 d^3r}{\varepsilon(\vec{r}_{max}) \left|\vec{E}(\vec{r}_{max})\right|^2}, \tag{1.4}$$

where $\varepsilon(\vec{r})$ and $\vec{E}(\vec{r})$ are the permittivity and electric field as functions of the spatial coordinate vector $\vec{r}$ and $\vec{r}_{max}$ is the spatial coordinate where $|\vec{E}(\vec{r})|$ is maximized.

1.3 Nanophotonic Structures for Optical Confinement

To maximize the enhancement of light matter interaction, we must realize platforms which can simultaneously realize large Q and low V_m to increase Q/V_m. Because the enhancement of light-matter interaction is dependent on the confinement of optical fields in space and time, optical resonance structures are popular platforms for enhancing light-matter interaction. This being said, devices with similar Q/V_m can perform quite differently, as the differences in modal energy dis-

tributions can lend themselves to being advantageous for different applications. Some properties which may be platform-dependent include non-linear performance, thermal actuation and mechanical flexibility. In general, considerations of application need to guide the choice of nanophotonic platform. The following section will discuss a few examples of optical resonance structures which have been used in the literature. Non-resonant devices which can enhance light-matter interaction will also be briefly discussed, as these structures are still relevant but not necessarily directly competing technologies with resonant optical structures.

1.3.1 Non-Resonant Methods

Non-resonant optical structures can be utilized to realize broadband enhancement of the interaction between light and matter by either increasing the optical path length of light through a particular area or by confining the light to a smaller region of space. A few popular methods of doing this include implementing randomized scattering of light [1, 2, 21], slow light modes [30–32], slotted waveguides [32–34], folded waveguides [35], and topological confinement [25, 36].

1.3.2 Whispering Gallery Resonators

Whispering gallery resonators work by circulating optical power via total internal reflection (TIR), as illustrated in Fig. 1.1 (a). This is often achieved through microtoroid or ring resonator geometries such as those in Fig. 1.1 (b,c) By circulating power through TIR, it is possible to achieve extremely low losses and high quality factors on the order of 10^8 or higher [38, 39]. Because of the large device footprint and design principle of power circulation, however, these devices have mode volumes which are many times the size of the wavelength ($> 100\ (\lambda/n)^3$) [39]. This leads to Q/V_m values from these devices up to $10^6\ (n/\lambda)^3$ being demonstrated in literature [39]. The extremely large Q from whispering gallery resonators often makes up for the relatively high mode volume from the platform in terms of overall Q/V_m metrics. This has led these devices to be utilized in many applications for enhancing light-matter interaction, such as lasing [40], sensing [37], optical modulation [23] and optomechanics [14]. It should be noted that while whispering gallery

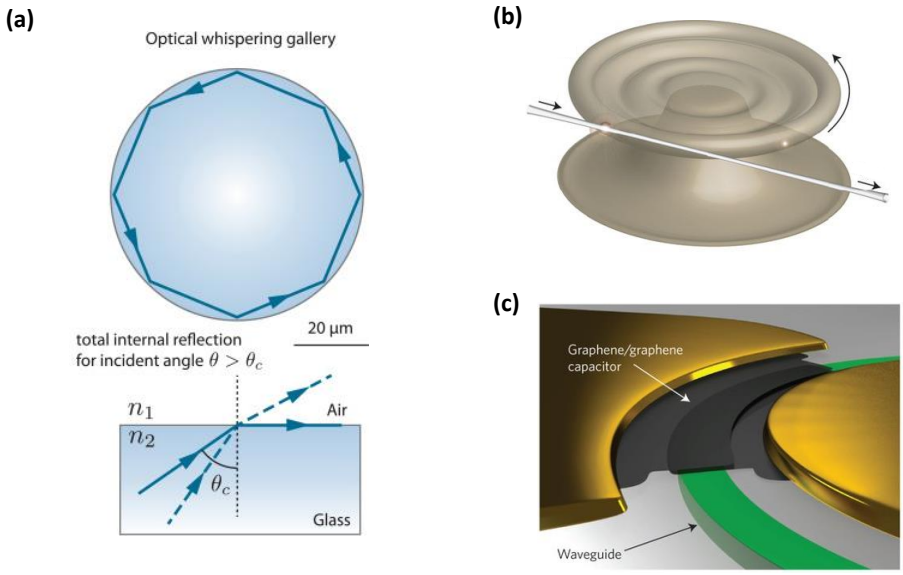

Figure 1.1: a) Diagram of whispering gallery mode circulating power through TIR [37]. b,c) Illustrations of whispering gallery resonators used for optomechanics (b) [14] and optical modulation (c) [23].

resonators are quite useful for a variety of applications, in general, due to their high Q, whispering gallery devices are very sensitive to changes in ambient environment. This sensitivity requires that environmental factors such as ambient temperature and humidity be precisely controlled to maintain stable device operation.

1.3.3 Plasmonic Resonators

Plasmonic resonators function by coupling the electromagnetic field oscillations from light to charge oscillations on conducting surfaces [41]. Surface plasmon resonance (SPR) and localized surface plasmon resonance (LSPR) function off of this same principle but at different length scales. In general, SPR refers to a propagating plasmon resonance in devices larger than the wavelength of light (Fig. 1.2 (a)) whereas LSPR refers to localized plasmonic effects observed in subwavelength nanostructures (Fig. 1.2 (b)). Because the nature of confinement is through coupling to charge oscillations, plasmonic resonances in general are more lossy and have low Q on the order of 10 [42] but hybrid plasmonic platforms can have significantly higher $Q > 100$ [43]. The real advantage

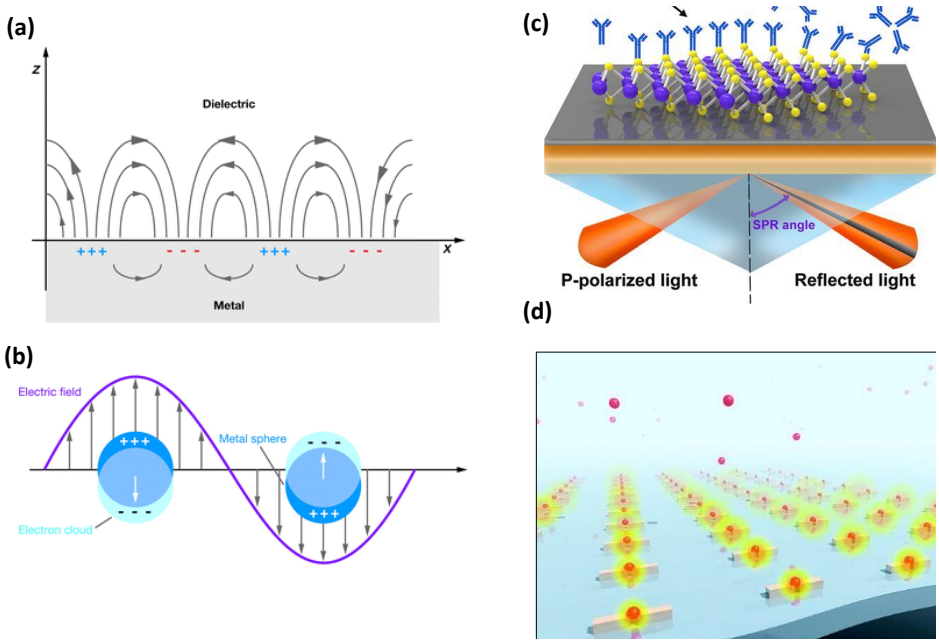

Figure 1.2: a) Illustration of surface plasmon resonance (SPR) in a metal dielectric interface [41]. Electromagnetic waves from light couple with surface charge oscillations to confine light to the interface. b) Illustration of localized surface plasmon resonance (LSPR) in metal nanoparticles [41]. The sub-wavelength nanostructures experience resonant charge oscillations which couple energy from the light to the surfaces of the nanostructures. c) SPR resonances can shift in wavelength with the introduction biomolecules near the resonant structure [6]. This shift can be utilized to detect the presence of various biomarkers depending on the surface functionalization used. d) LSPR resonance create large local field intensities which can be leveraged to trap and manipulate small particles [4].

of coupling to charge oscillations is an exceptionally small mode volume for plasmonic resonances which have been reported down to $10^{-4}\ \lambda^3$. This leads to maximum possible Q/V_m values on the order of $10^6\ (1/\lambda)^3$ where the mode is predominantly localized in air. The small mode volume of plasmonics allows them to achieve formidable Q/V_m metrics. Accordingly, they have been utilized in a variety of applications for enhancing light-matter interaction, such as optical trapping [4], sensing [6, 41], lasing [11] and metamaterials [9, 44]. It should be noted, however, that the intrinsic nature of coupling to charge oscillations introduces losses to electrical heating. This can be a disadvantage to thermally sensitve applications in biology or communications which involve require propagation distances. Some plasmonic applications are illustrated in Fig. 1.2 (c,d).

1.3.4 Photonic Crystal Resonators

The research in this proposal will focus on a subset of photonic crystal resonators. As such, the following subsection will attempt to present an intuitive picture of photonic crystals for further discussion. Rigorous discussion of photonic crystals is presented in [45].

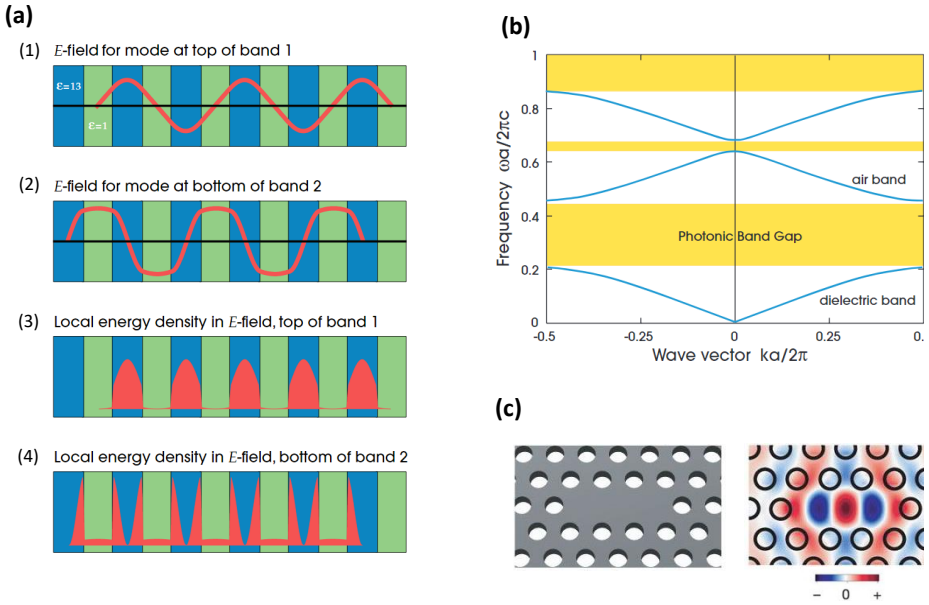

Figure 1.3: a) Illustration of different modes with same periodicity due to overlap of high field amplitudes with different index regions of the 1D stack [45]. b) Example photonic band structure for a 1D photonic crystal [45]. c) Illustration of defect in a 2D photonic crystal cavity created by removing holes from the lattice [46]. The defect mode is shown to the right. The color bar shows high field amplitude with deeper colors and phase denoted by red (+) and blue (-).

Photonic crystals utilize periodic variations in refractive index to manipulate the propagation and localization of photons. This periodic index variation serves analogously to the periodic potential in semiconductor materials which allow semiconductors to control the properties of electrons. In the simplest case of a 1-dimensional (1D) photonic crystal, we can think of the periodic index variation as restricting the translational symmetry of waves passing through the nanostructure. In Fig. 1.3 (a) (1, 2) a wave with the same periodicity as the optical lattice can be translated to have the highest amplitude in either the high index region of the 1D stack or the low region of the 1D stack. Doing this results in allowed states shown in Fig. 1.3 (a) (3, 4) having different spatial field profiles due to the overlap with high or low index regions of the stack. The difference in the spatial

field profiles results in different solutions for the oscillation frequencies of the modes, even though they have the same periodicity. Because the periodicity of a wave is directly linked to the wave vector (or k-vector, momentum vector, etc.) of the mode, we quickly see that multiple frequencies of light can have the same wave vector propagating through the nanostructured material.

As seen in Fig. 1.3 (b) the periodicity of the optical lattice results in a band structure which dictates the allowed states of photons in the lattice. This band structure specifies the allowed combinations of frequency, ω, and wave vector, k, which can propagate through the photonic crystal. In this case, as in many, the values of frequency and wave vector are normalized to the period of the lattice, a. While Fig. 1.3 (b) shows the band structure for a 1D photonic crystal, more complex band structures are also attainable by higher dimension crystals, such as 2D or 3D, enabling control of light in more dimensions.

Perhaps the most important feature in Fig. 1.3 (b) are the yellow highlighted regions labeled "Photonic Band Gap". The band gap is a range of frequencies for which there is no allowed state in the photonic crystal. This bandgap is created due to destructive interference of light as it propagates through the photonic crystal, resulting in light constructively interfering in back-reflections away from the device. The way we can utilize photonic crystals for confining light in space and time is by locally creating allowed states which exist in the band gap. Because light inside of these locally allowed states has nowhere to travel in the rest of the photonic crystal, it stays confined. Some reasons light does not practically stay confined forever is that light can escape through evanescent tails which extend into the cladding and substrate and via scattering off imperfections in the fabricated photonic crystal. These evanescent tails and imperfections work to couple light from confined modes into nearby, unconfined modes. The simple way we can locally create states inside of the band gap is by creating defects in the lattice, such as in Fig. 1.3 (c). By creating a defect, such as removing holes from a 2D photonic crystal, we can create a locally allowed state which can confine optical energy due to the presence of a band gap which localizes light within the defect region.

In practical applications, photonic crystals have been utilized for creating many optical com-

ponents, such as filters [47, 48], modulators [32, 49], waveguides [50], sensors [30, 51, 52] , photovoltaics [1, 2], lasers [12, 53], etc. This is in part due to their exceptional performance metrics, namely Q and V_m attainable. The highest Q value experimentally reported in a photonic crystal cavity is given at 10^7 [17]. The lowest V_m demonstrated in photonic crystals are on the order $10^{-4}\ (\lambda/n)^3$ measured in simulation [54] and $10^{-3}\ (\lambda/n)^3$ verified experimentally [20]. The highest combination of Q/V_m attained in a single photonic crystal is recorded at $\sim 10^{10}\ (n/\lambda)^3$ in simulation [54] and $\sim 10^8\ (n/\lambda)^3$ in experiment [20], which is orders of magnitude higher than what is possible with whispering gallery and plasmonic platforms.

1.4 Photonic Crystal Nanobeams

A subset of the photonic crystal platform which maintains the highest Q/V_m metrics possible with photonic crystals while minimizing device footprint is the photonic crystal nanobeam (PCN) [20, 54]. The maximum Q/V_m demonstrated from these devices is $\sim 10^{10}\ (n/\lambda)^3$ in simulation [54] and $\sim 10^8\ (n/\lambda)^3$ in experiment [20], currently making them the nanophotonic platform with the highest potential for enhancing light-matter interaction.

PCN devices, examples illustrated in Fig. 1.4, are essentially 1D photonic crytals embedded inside of waveguides. The waveguides (often nanobeams of silicon or another dielectric) act to confine light laterally to the direction of propagation while the embedded photonic crystal may confine light in the direction of propagation. As illustrated in Fig. 1.4 (d) tailoring of the unit cell which makes up the photonic crystal lattice can be utilized to confine light further [54, 58].

Because of their small device footprint and high Q/V_m metrics, photonic crystal nanobeams are perhaps one of the most promising nanophotonic platforms for densely integrated on-chip photonic applications. This has led them to be implemented in applications such as optomechanics [13, 56, 59], optical modulation [49], sensing [51, 60], optical trapping [5], and light emission [12, 53] as well as being researched for potential quantum computing applications [26]. Their performance has also fueled work to make their fabrication CMOS compatible for mass production (Fig. 1.4(c))[57]. A few of these applications are illustrated in Fig. 1.4 (b).

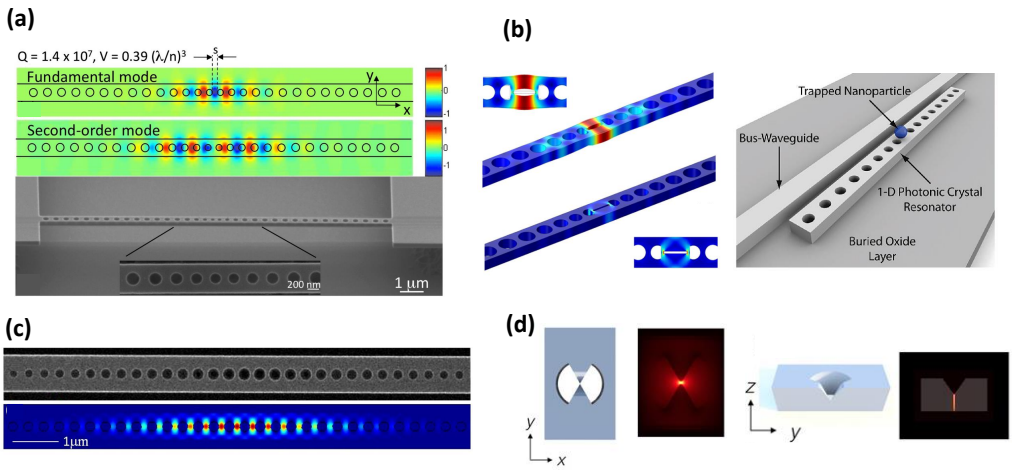

Figure 1.4: a) Simulated field profile and SEM of high Q/V ($\sim 10^7$ simulated PCN with standard circular hole unit cells [55]. b) Examples of PCN cavities used for optomechanics [56] (left) and nanomanipulation [5] (right) applications. c) SEM and field profile of a PCN cavity that was fabricated using CMOS compatible methods [57]. d) Bowtie PCN unit cell design for extreme subwavelength confinement. This unit cell geometry has been implemented in the PCN cavities with highest Q/V achieved to date [20, 54]

.

1.4.1 Implementation Challenges and Motivation for Solutions

Despite the high performance metrics of photonic crystal nanobeams, there are important challenges to address for their practical implementation. One of the most important challenges is accessing the fundamental resonance mode of these devices, which is illustrated in Fig. 1.4 (a,c). The fundamental resonance mode of PCN cavities is generally the mode with the highest Q/V_m metrics, which is most useful for applications. Accessing this mode in on-chip coupling configuration, however, can be difficult due to the tradeoff between Q and transmission intensity, lowering the practicality of PCN devices for integrated photonics. Some work circumvents on-chip coupling when characterizing PCN cavities with high signal-to-noise measurements from out-of-plane [13, 55, 59]. Most work does not rigorously prove a spectral peak corresponds to the fundamental resonance through direct spatial field profile measurements such as NSOM and choose to use modeling to estimate the peak position. Consequently, it is often difficult to find experimental verification of mode order [20] or find rigorous analysis of coupling efficiency [61].

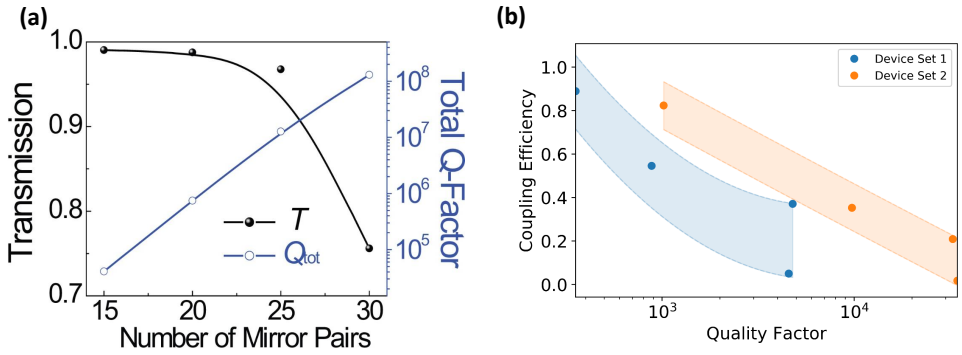

Figure 1.5: a) Graph of transmission and Q-factor for PCN cavities with differing numbers of unit cells (mirror pairs) inside of the cavity taper [61]. Results from this data were simulated using FDTD methods. Note that as the resonance Q increases the transmission decreases. Imperfections from fabrication could additionally reduce the total Q and transmission from simulated results. b) Graph of resonant transmission vs resonance quality factor for the same resonance order in devices with varied tapering. Increasing the mirror strength used in the PCN increases the Q but consequently lowers the resonance transmission as it isolates the cavity from the feeding waveguide. Dashed lines are exponential fits for the uncertainty bounds for each device set presented.

Figure 1.5 illustrates the issue of coupling efficiency in an on-chip configuration where resonances are excited from the edge of the cavity. In both graphs from [61] (Fig. 1.5 (a)) and our own device measurements (Figure 1.5 (b)) we can see that with increasing Q we see lower transmission on resonance which corresponds to lower coupling efficiency, η, to resonant modes. η will be rigorously defined later in Chap. 2. One work notes that the resonant transmission of the fundamental resonance mode in their devices is so low that it cannot be detected in their experiments [60].

Figure 1.6 illustrates the issue of mode identification in an on-chip configuration where resonances are excited from the edge of the cavity and resonant transmission is small for lower order modes. Using a dipole source allows us to easily excite resonance modes in simulation so we can characterize their performance metrics connected to the mode order. In experiment, however, we often do not have tools to quickly identify resonance mode order. In Figure 1.6 (a) we excite resonant modes by a dipole source (blue) and alternatively by injecting light from the edge of the cavity (red). We can see in the normalized spectrum from each method in Figure 1.6 (b) that there are

modes strongly excited by the dipole that are undetectable by the edge excitation. When we look at the first visible peak from the edge coupling method, we see that the excited mode is of a much higher order than the fundamental mode excited by the dipole. Consequently, the two different modes have very different spatial field extends and mode volumes. This raises the question of how to determine mode order from a transmission spectrum when resonances can be suppressed.

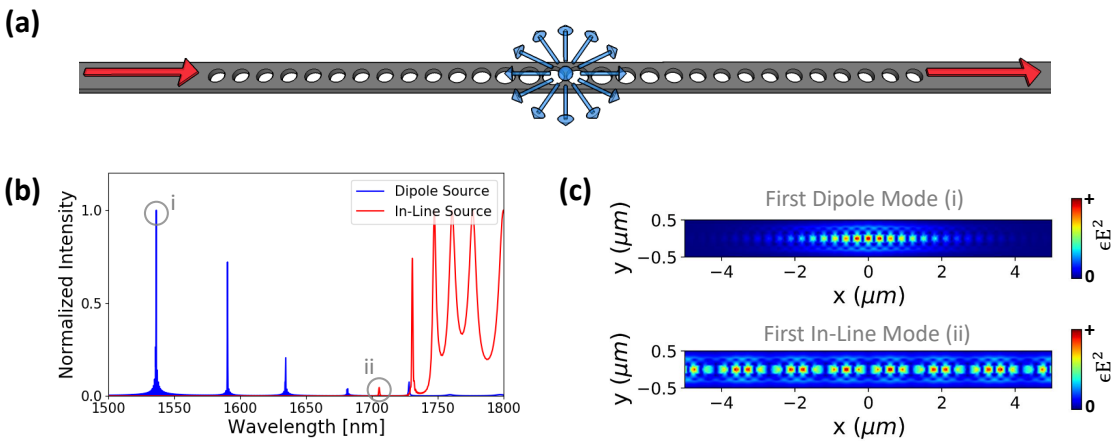

Figure 1.6: a) Schematic illustration of a PCN cavity being excited via dipole coupling (blue) and coupling from cavity edge (red). b) Normalized intensity spectrum for both the dipole power enhanced by the cavity (blue) for dipole coupling and transmitted optical power through the cavity (red) from edge coupling. The lowest order resonance with intensity above the baseline level excited via each excitation method is circled. c) Electric field profiles for resonances labeled (i) and (ii) in (b). It can be clearly seen that the fundamental resonance mode excited via dipole coupling does not match the lowest order mode observed from in-line coupling in mode profile.

Chapter 2

Implementation of Side-Coupled Photonic Crystal Nanobeams

The following chapter is taken from a publication in JOSA B titled *"Efficient side-coupling to photonic crystal nanobeam cavities via state-space overlap"* [62]. This work addresses the issue of coupling efficiency in exciting the fundamental resonance mode of photonic crystal nanobeam (PCN) cavities. By evanescently coupling to PCN resonance modes via a straight bus waveguide, we demonstrate in simulations and experiment that we may improve coupling efficiency by considering the overlap of the two modes in state-space (the generalization of physical space, frequency space and k-space for optical systems). The coupling analysis is rigorously and practically presented via the intrinsic and coupling losses of the resonator. We additionally outline how to experimentally extract the values of these losses from measurements of physical devices. Excitation of fundamental PCN resonance modes are verified experimentally via the band edge of a PCN consisting of unmodulated unit cells with geometry identical those used in the center of the fabricated PCN cavities. We additionally define the over-, under- and critically-coupled regions of performance for a side-coupled PCN. Using the formalism presented and concepts of state-space, show that designing efficiently side-coupled PCN cavities is as simple as controlling the overlap of the bus waveguide and cavity resonance modes in both physical and k-space.

2.1 Introduction

Optically resonant nanophotonic structures hold great promise in applications including optical signal processing [23, 24, 63], nanomanipulation [4, 5, 64], photovoltaics [2], imaging [9], and sensing [51, 65]. On-resonance, these structures support high, localized optical field intensities that can be leveraged for enhancing various types of interactions between light and matter. Resonant field enhancements in photonic and plasmonic devices result directly from the confinement of light both spatially, as characterized by the mode volume (V), and temporally, as characterized by the

quality factor (Q). Most resonant nanophotonic structures have the ability to attain either high Q or low V_m, but lack the ability to simultaneously demonstrate significant spatial and temporal confinement (i.e., high Q/V_m) [4, 38, 39, 66]. Photonic crystal nanobeam (PCN) cavities are the exception [19, 20, 56, 58]. PCN cavities have the design flexibility necessary to achieve low V while maintaining ultra-high Q, and they have the highest Q/V_m metrics reported to date [19, 20]. Hence, PCNs are one of the most promising nanophotonic building blocks for realizing on-chip photonic devices with improved performance metrics, lower power consumption, and smaller footprint.

Previous work on PCN cavities has shown these devices may be resonantly excited in various coupling configurations. Out of plane excitation methods such as the resonant scattering technique have proven useful for measuring exceptionally high quality factors [55, 67], leveraging optical forces [13, 59] and sensing changes to environmental refractive index [68]. While out-of-plane functionality is useful for many applications, in-plane functionality is a requirement for on-chip integration of PCN cavities with other photonic components. One of the most widespread and well-understood configurations for PCNs with in-plane functionality is in-line coupling, where light is coupled to resonant PCN modes from the edge of the cavity [19, 20, 56, 58]. This configuration produces spectral peaks at resonant wavelengths, low transmission at non-resonant wavelengths in the PCN band-gap, and high transmission outside the band-gap. The importance of sharp, high-contrast spectral features for signal processing applications in combination with the relatively small device footprint of PCN cavities makes them an attractive element for dense, on-chip optical circuits. While in-line coupling to PCN cavities has demonstrated promise for on-chip signal processing, utilization of in-line coupling in compact multiplexing schemes (e.g. serial integration and add/drop filtering) is generally not feasible. This is due to low baseline transmission and limited input and output ports in an in-line coupling configuration. Multiplexing functionality can be greatly improved by evanescently side-coupling to PCN cavities [51, 69].

Side-coupling to PCN cavities has not been as intensively studied for design principles as the in-line coupling configuration. Prior work implementing simple bus waveguides for side-coupling

into PCN cavities has briefly mentioned basic design concepts without detailed study [48, 70]. We note that design analysis of PCN cavities laterally coupled to a waveguide Fabry-Perot resonator [71–73], waveguides laterally coupled to ring resonators [74], fibers coupled to phase matched photonic crystal waveguides [75], and generalized optical coupling formalisms [45, 76] have all been discussed in depth. Evanescent coupling to PCN cavities has also been discussed with greater detail in relation to lasing applications [53, 77]. In this work, we show through simulation and experiment how tuning the overlap in state-space between a simple bus waveguide mode and PCN cavity resonances can be carried out as a straightforward approach to efficiently excite high Q PCN resonances.

2.2 Design Considerations

2.2.1 Evanescent Coupling and State-Space Overlap

Evanescent coupling between two optical devices, such as waveguides and resonant cavities, occurs when energy is transferred from a photonic mode in one device to a photonic mode in the other device by means of the evanescent tails of the electric field distributions. The rate of energy exchange between a resonant cavity and its environment can be characterized by two connected metrics: the quality factor, Q, and the cavity field decay rate, Γ. In this paper, both of these terms will be used. The relationship between Q and Γ is

$$Q \propto \frac{1}{\Gamma}, \tag{2.1}$$

as Q is proportional to the average photon lifetime in the cavity and Γ is inversely proportional to the lifetime of the cavity. Both Q and Γ can be used to describe the overall losses of the cavity or particular categories of cavity loss, such as losses due to resonator coupling (Q_c, Γ^c) or intrinsic resonator losses (Q_0, Γ^0).

The efficacy of evanescent coupling, or extent of energy exchange between optical devices as defined by the coupling decay rate, Γ^c, is dependent on the overlap of the two modes in state-space

(e.g., physical space, k-space, ω-space). In physical space, the overlap of the modes is controlled by adjusting the size of the physical gap separating the evanescently coupled optical devices. In k-space, the modal overlap may be adjusted by offsetting the wave-vectors supported between the two devices. In the case of an optical device with discontinuous values allowed in state-space, such as a resonator where limited combinations of optical frequencies and wave-vectors are supported, coupling between the resonant device and a feeding device, such as a waveguide, may only occur when the mode of the feeding device is similar to an allowed mode in the resonator. Considering one of the most common evanescently coupled photonic components, a ring resonator, coupling between a straight bus waveguide and a resonant ring occurs when the bus waveguide mode is of the same frequency as the resonant mode in the ring. Generally, the wave-vectors of the bus waveguide mode and resonant mode in the ring are very similar in the coupling region when the bus and ring waveguides have similar widths. Consequently, the rate of energy exchange between the bus waveguide and resonant ring is almost entirely determined by the gap spacing between the bus waveguide and the ring. Hence, to approach critical coupling for ring resonator devices, usually a small parameter sweep of coupling gap sizes, in experiment or simulation, is sufficient to realize an optimal device configuration.

For evanescent coupling between a bus waveguide and a PCN cavity, however, it cannot be assumed that the wave-vectors of the bus waveguide and PCN cavity are similar. Additionally, the optical coupling efficiency, η, in evanescently coupled PCN cavities and ring resonators is described by different solutions of the scattering-theory of waveguide-resonator coupling [76]. Different solutions for η exist between ring resonators and PCN cavities because ring resonator modes are degenerate, two distinct modes exist at the same frequency, while PCN cavity modes are non-degenerate and only one resonance mode exists at a particular frequency. PCN modes are generally non-degenerate unless otherwise engineered to display degenerate behaviour [48, 76]. Therefore, additional design considerations are necessary to maximize η through properly balancing the intrinsic losses, Q_0 and Γ^0, and the coupling losses, Q_c and Γ^c, of the cavity. This may be achieved by ensuring that the modes of the bus waveguide and PCN cavity have the appropriate

overlap in both physical and k-space.

2.2.2 Calculating Wave-Vectors of Bus Waveguide and PCN Cavity

As a first step toward tuning the degree of k-space overlap between a PCN cavity mode and bus waveguide mode, we define the wave-vectors of these modes. Assuming the PCN cavity mode is designed to be at the edge of the Brillouin zone, the wave-vector of the resonant cavity mode is given by

$$k_{cav} = \frac{0.5}{a}\left(\frac{1}{\text{nm}}\right), \tag{2.2}$$

where a is the period of the air holes comprising the PCN. In this work, the PCN cavity mode is a dielectric mode. The band structure of the PCN, which depends on the dimensions of the unit cell, determines the dielectric band edge frequency and, thus, the dielectric cavity mode resonance frequency, as discussed in Sec. 2.3. In order to couple light from a bus waveguide to the PCN cavity mode, there must exist a bus waveguide mode that has the same frequency as the PCN cavity mode. The wave-vector of such a bus waveguide mode is given by

$$k_{wg} = n_{eff-wg} \cdot \frac{1}{\lambda_{res}}\left(\frac{1}{\text{nm}}\right), \tag{2.3}$$

where $n_{eff-wvg}$ and λ_{res} are the effective index of the propagating waveguide mode and the free-space wavelength corresponding to the PCN cavity resonance frequency, respectively. The condition necessary for maximum overlap in k-space, or phase matching, between the bus waveguide and PCN cavity modes can be obtained by setting $k_{cav} = k_{wg}$, as shown in Eqn. (2.4).

$$n_{eff-wvg} = \frac{0.5}{a} \cdot \lambda_{res} \tag{2.4}$$

Therefore, in order to control the rate of energy exchange rate, Γ^c, between a side-coupled bus waveguide and PCN cavity, we can adjust *(1) the coupling gap between the bus waveguide and the cavity* as well as *(2) the offset between the k-vector of the cavity and the k-vector of the bus*

waveguide. By tuning these parameters, Γ^c can readily be altered. With the proper choice of Γ^c with respect to Γ^0, we can realize large η for resonance modes, which is discussed in the next section. Additionally, a computationally efficient method to quickly determine a functional combination of bus waveguide width and coupling gap for practical devices is presented in Sec. 2.4.

2.2.3 Coupling Efficiency for In-Line vs Side-Coupled Devices

In discussing the design of side-coupled PCN cavities, it is important to outline differences in coupling which alter optimal PCN geometric parameters for use in a side-coupled configuration from those for use in an in-line configuration. For in-line coupling to PCN cavities, the resonant coupling efficiency of the PCN cavity to the coupled waveguides, η, and transmission coefficient, T, on resonance can be calculated by the equation

$$\eta_{(in-line)} = T_{(in-line)} = \frac{(\Gamma^c)^2}{(\Gamma^0 + \Gamma^c)^2}\,, \tag{2.5}$$

where Γ^c is the coupling decay rate and Γ^0 is the intrinsic decay rate of the cavity [76]. In the in-line case, Γ^c refers to of the decay rate of the resonance field into the coupling waveguides at the edges of the cavity [76]. Γ^0 represents the decay rate of the resonance field that is not coupled into the waveguides present at the edges of the cavity. The loss associated with Γ^0 is coupled into free-space or the underlying substrate (if present) through scattering. These losses are schematically described in Fig. 2.1(a). When designing cavities for in-line operation with transmission peaks on resonance, it is important to note that Γ^0 and Γ^c are, in general, entangled quantities. By increasing the length of tapering or the number of mirror pairs in a PCN cavity, it is possible to significantly decrease the scattering decay rate, Γ^0, as longer taper lengths and extra mirror pairs more gradually and strongly confine the resonance modes. Longer taper lengths and mirror pairs, however, also work to decrease the rate of energy exchange with the feeding waveguide, Γ^c, as the mode becomes less coupled to the surrounding waveguides by a spatially

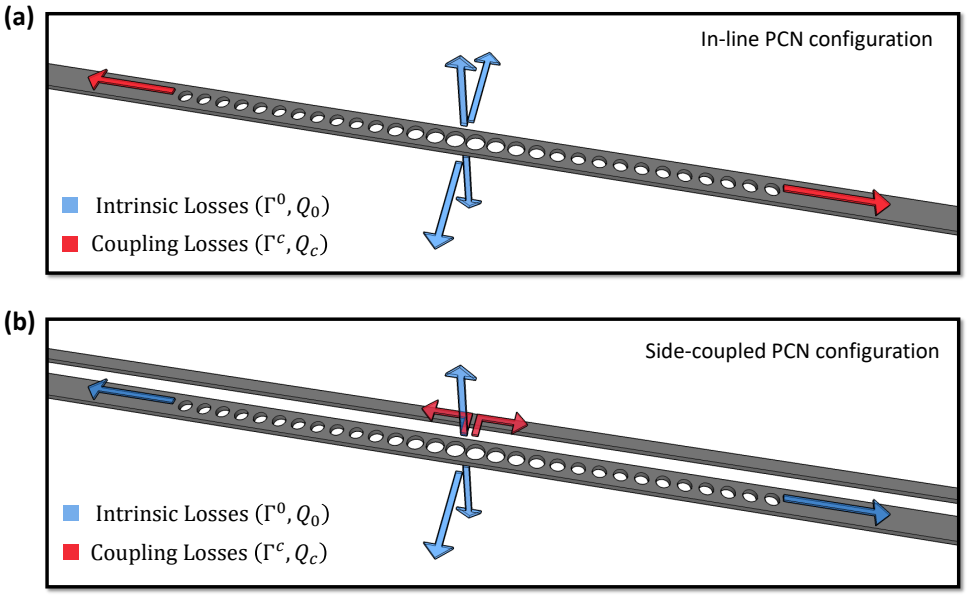

Figure 2.1: Schematic illustration of coupling losses associated with (a) in-line and (b) side-coupled PCN cavities. a) Intrinsic losses (blue) correspond to resonant fields decaying into modes which scatter into free-space surrounding the device. Coupling losses (red) correspond to resonant fields decaying into modes guided by the waveguides present at the edges of the cavity. b) Intrinsic losses (blue) correspond to resonant fields decaying into modes which scatter into free-space surrounding the device and through the edges of the cavity. Coupling losses (red) correspond to resonant fields decaying into modes guided by the lateral bus waveguide.

larger potential barrier induced by added taper and mirror segments. Previously reported results on in-line devices show that the competing rates of increase between Γ^0 and Γ^c can lead to decrease in on-resonance transmission and resonance coupling efficiency for in-line PCN cavities with higher Q [61]. Thus a proper compromise between Q and η must be made for any in-line application.

In side-coupled devices, resonance conditions cause dips in transmission. The equations for transmission and coupling efficiency defined by low resonance transmission are

$$T_{(side-coupled)} = \frac{\left(\Gamma^0\right)^2}{\left(\Gamma^0+\Gamma^c\right)^2} \tag{2.6}$$

$$\eta_{(side-coupled)} = 1 - T_{(side-coupled)} = \frac{2\left(\frac{\Gamma^c}{\Gamma^0}\right)+\left(\frac{\Gamma^c}{\Gamma^0}\right)^2}{\left(1+\frac{\Gamma^c}{\Gamma^0}\right)^2}. \tag{2.7}$$

Equation (2.7) is written as a function of Γ^c/Γ^0 for utility when calculating theoretical transmission from simulations, which will be discussed further in Sec. 2.4.4. *It is important to note that* Γ^0 *and* Γ^c *refer to different decay mechanisms in side-coupled and in-line configurations* [76]. These differences are illustrated in Fig. 2.1. For side-coupling, Γ^c refers to the coupling decay rate of the resonance field into the side-coupled bus waveguide and Γ^0 refers to the decay rate associated with the resonance field decaying both through free-space scattering and through the edges of the cavity. The utilization of a side-coupler allows decoupling of intrinsic and coupling losses to the PCN cavity. So long as the introduction of the bus waveguide is realized in a way to not significantly perturb the cavity mode, the intrinsic losses result solely from the cavity geometry, whereas the coupling losses are determined by the overlap of the cavity and bus waveguide modes in physical and k-space. The decoupling of intrinsic and coupling losses could potentially enable larger coupling efficiency, η, at high quality factors than what is possible in an in-line configuration. The loaded Q of a system with high η is then determined by the ratio of the decay rates, Γ^c/Γ^0. As described in Sec. 2.2.2, Γ^c may be directly controlled by tuning the overlap of the two optical modes in state-space. Γ^0 may be controlled by altering the cavity taper length and number of extra mirrors at the edges of the cavity.

2.3 Simulations

2.3.1 Simulation Specifications and PCN Design

Two-dimensional (2D) finite-difference time-domain (FDTD) simulations were carried out in Lumerical to design and characterize side-coupling effects on PCN cavities. Two-dimensional analysis was chosen due to the significant computational resources required to simulate parameter sweeps for high Q cavities. Because two dimensional simulations allow for separation of coupled optical modes in both physical and k-space, they allow sufficient degrees of freedom to probe effects of proximity in state-space on coupling and performance of PCN cavities. These degrees of freedom consist of (1) *the spatial dimension along which the bus waveguide and PCN cavity*

are separated and (2) *the dimension in k-space by which the two optical modes are offset*. While the exact distributions of optical modes in physical and k-space may differ between 2D and 3D simulations along the axes of separation, the trends in PCN cavity resonance depth as a function of bus waveguide width and coupling gap size are expected to be similar for 2D and 3D analysis because of the similar degrees of freedom utilized in both cases. It is also important to note that the coupling formalism used here, which is detailed in [76], is independent of device dimensionality.

The deterministic design approach for PCN cavities was followed in order to reduce scattering losses and increase the intrinsic quality factor of the PCN cavities[61, 78]. The specific dimensions utilized for the PCN cavities to achieve a fundamental resonance mode near $\lambda = 1550$nm are as follows. The width of the silicon nanobeam was selected to be $nw = 600$nm and the air-hole period was set to $a = 300$nm with deterministic tapering from a hole radius of 103nm in the mirror segments to a radius of 130nm in the cavity region. We chose $nw = 600$nm in the 2D simulations to tailor the lateral confinement of the optical mode to better mimic the performance of 3D devices. The modes of fabricated PCN devices (i.e. 3D devices with finite thickness), such as those studied in Sec. 2.4, are less well confined compared to those of a 2D PCN device in simulation with the same *nw*. Using a smaller *nw* in 2D simulations helps to maintain a similar level of lateral field confinement. To maintain the cavity resonance frequency near 1550nm with this *nw*, a relatively short period of $a = 300$nm was employed. A taper length of 20 unit cells was utilized along with 10 identical unit cells in the end mirror regions to yield a well-confined resonance mode. The band structure of the unit cells comprising the PCN and a schematic of the PCN are shown in Fig. 2.2(a,b). By gradually modifying the unit cell band structure from the ends of the mirror region to the cavity center, a locally allowed state is created at the edge of the Brillouin zone. Figure 2.2(a) shows that in a PCN designed for a dielectric cavity resonance mode, the resonance frequency is determined by the dielectric band edge frequency for unit cells in the cavity center, where the cavity resonance wave-vector is $k_x = {}^{0.5}/_{a}$ (i.e., at the edge of the Brillouin zone). The profile of the fundamental cavity resonance mode of the designed PCN cavity is shown in Fig. 2.2(c) and has a simulated $Q_0 = 1.7 \times 10^8$. This calculated quality factor is the intrinsic quality factor and is

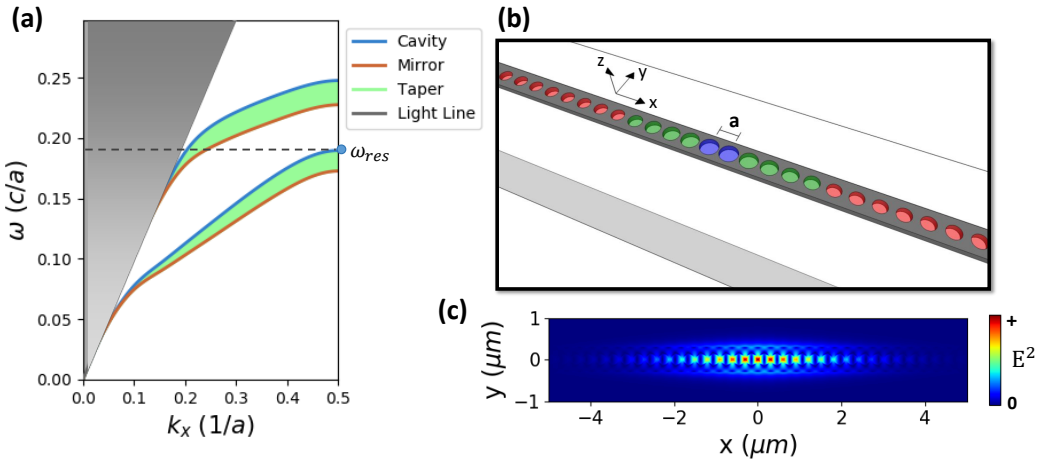

Figure 2.2: a) Band diagram of TE modes associated with end mirror (red), taper (green), and cavity (blue) regions of the photonic crystal cavity shown in b). These bands were calculated via 2D FDTD simulations. b) Schematic illustration of deterministically designed PCN with cavity resonance state within the band gap of the end mirror segments. c) Mode profile of fundamental resonance of designed PCN cavity.

associated with the intrinsic losses, Γ^0, due to the absence of a side-coupler in these simulations.

2.3.2 Simulating Modal Distribution of Wave-Vectors

To explore the properties of evanescent coupling discussed in Sec. 2.2, we carried out simulations to examine how tuning the overlap in k-space between modes of a straight bus waveguide and a PCN cavity affects side-coupled performance. We first examined the Fourier transform of the electric field profile of the PCN cavity fundamental mode (Fig. 2.2(c)) to visualize the cavity resonance profile in k-space, as shown in Fig. 2.3(a). The wave-vectors are localized at $|k_x| = 0.5/a$, as expected for a deterministically designed cavity. Next, in order to tune the wave-vector of light evanescently coupled from the bus waveguide, the effective index of the bus waveguide was altered by adjusting w, the width of the bus waveguide. Lumerical MODE Solutions was used to calculate the effective index of the fundamental TE-mode in the bus waveguide for different values of w. Increasing w leads to an increase in the wave-vector of the guided mode. Fig. 2.3(c) shows the Fourier transform of the electric field distribution in the bus waveguide for three different waveguide widths, w = 250nm, 290nm, and 400nm, corresponding to k-space distributions

centered around wave-vectors that are less than, nearly equal to, and greater than the wave-vector of the resonant PCN cavity mode, respectively. FDTD simulations of the waveguide mode profile in k-space were done with a 5000fs pulsed mode source at the resonant wavelength of the PCN cavity and measured by a 2D electric field monitor extending through the waveguide. The long mode source was utilized to minimize transient effects and to ensure guided optical fields extended throughout the full waveguide region monitored.

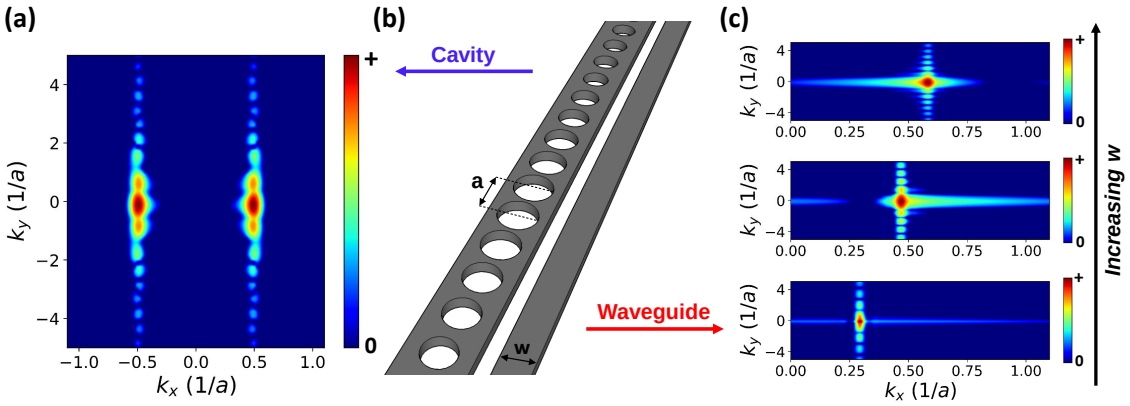

Figure 2.3: a) k-space plot of optical cavity resonance taken from the Fourier transform of the field profile shown in Fig. 2.2(c). b) Schematic illustration of side-coupling configuration for PCN cavity. c) k-space plots of bus waveguide modes of various waveguide widths (w = 250nm, 290nm, and 400nm). By increasing the waveguide width, it is possible to increase the k-vector of the waveguide mode due to an increase in the modal effective index.

2.3.3 Computational Results of State-Space Overlap on Coupling

As stated previously, controlling the overlap of the bus waveguide and cavity resonance modes in both k-space and physical space allows control of the rate of energy exchange due to coupling, Γ^c. To investigate the effect of modal overlap in state-space on the efficacy of resonance excitation in PCN cavities, 2D calculations in Lumerical FDTD Solutions were carried out. These simulations calculated the transmission spectrum of the PCN specified at the beginning of Sec. 2.3 when side-coupled using different bus waveguide and coupling gap dimensions. As discussed previously, we believe the results of the less computationally intensive 2D simulations are able to sufficiently illustrate trends in the physical behavior of the side-coupled PCN system, and we show this to

be the case in comparison to experimental results in Sec. 2.4. The three aforementioned bus waveguide widths were considered and the coupling gap size was varied between $100 - 600$nm. The resulting transmission spectra of these simulations are shown in Fig. 2.4(a).

The most pronounced resonances occur when the wave-vector of the bus waveguide mode closely matches that of the PCN cavity resonance (i.e., $w = 290$nm). For the side-coupled PCN with the narrowest bus waveguide width, the transmission features that appear for small coupling gap size are most likely Fabry-Perot fringes that result from the finite size of the bus waveguide used in the simulation and the large evanescent tail of the electric field that extends from the narrow waveguide. Two narrow, but rather shallow resonances appear in the transmission spectra of the side-coupled PCN with the widest bus waveguide width and smaller coupling gaps. Overall, the data in Fig. 2.4(a) suggest that the coupling decay rate, Γ^c, between the PCN cavity and bus waveguide modes is strongly affected by the wave-vector mismatch between the bus waveguide and cavity resonance modes.

It is important to note that in the case where the waveguide width, w, is narrowest ($w = 250$nm), the evanescent tail of the electric field extending from the bus waveguide is the largest due the mode being more delocalized and having a lower effective index. However, despite the fact that the 250nm wide bus waveguide has the largest field overlap in physical space with the PCN cavity, coupling from the bus waveguide of width $w = 290$nm is significantly improved. Although the spatial field overlap between the bus waveguide with $w = 290$nm and the PCN cavity is not the largest of the three bus waveguides considered, the wave-vector of the bus waveguide is the most closely matched to that of the PCN cavity resonance. Therefore, we conclude that the effect of modal overlap in k-space may, at times, dominate the effect of field overlap between devices in physical space.

Next, we simulated transmission spectra for side-coupled PCNs with constant $g = 150$nm and variable w between $240\text{nm} - 350\text{nm}$ to further explore the dependence of the k-space overlap on the energy exchange rate between the bus waveguide and PCN cavity. Figure 2.4(b) shows that the width and depth of the fundamental transmission resonance is highly dependent on the

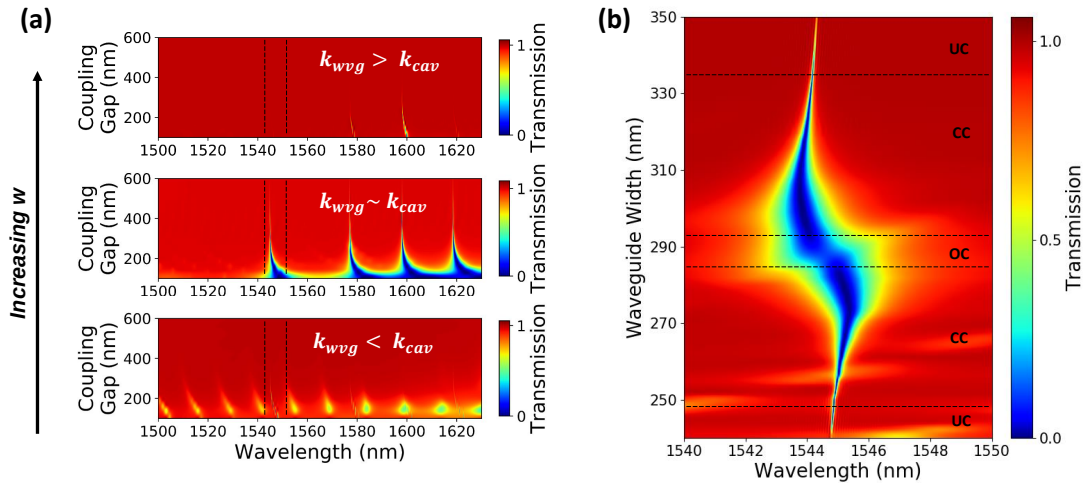

Figure 2.4: a) Simulated transmission from side-coupled PCN cavities with bus waveguide widths of 250nm (Bottom), 290nm (Middle) and 400nm (Top) and different coupling gap sizes. b) Simulated transmission from side-coupled PCN cavities with fixed coupling gap (g = 150nm) and various waveguide widths. Under-coupled, over-coupled and critically coupled regions are denoted by **UC**, **OC** and **CC**, respectively.

bus waveguide width, and, hence, its supported wave-vector. We note that the slight change in resonance wavelength as a function of w is likely due to the different levels of interaction between the bus waveguide mode and the PCN cavity resonance mode, which affects the cavity resonance frequency. By increasing w, at a constant g, the modal overlap between the bus waveguide and PCN cavity is altered in k-space and the coupling regime is altered.

2.3.4 Coupling Regimes in Side-Coupled PCN Cavities

To categorize the effectiveness of a side-coupled geometry, it is important to define coupling regimes which describe the device performance. In Fig. 2.4(b), we label different side-coupled geometries as under-, over- and critically-coupled, borrowing the common terminology used to identify different coupling regimes for ring resonators. While the transmission spectra of evanescently coupled photonic crystals and ring resonators are not described by the same equations, similar physical features can be observed in each case.

The conventional use of the terms over-coupled, under-coupled, and critically coupled in ring resonators can be summarized as follows:

(Ring, 1) Critically coupled ring resonators have $\eta = 1$, meaning $T = 0$ on resonance.

(Ring, 2) Under-coupled ring resonators have $\eta < 1$ and higher Q than the critically. coupled case

(Ring, 3) Over-coupled ring resonators have $\eta < 1$ and lower Q than the critically coupled case.

In this work we utilize the terms over-coupled [*o.c.*], under-coupled [*u.c.*], and (near) critically coupled [(*n.*)*c.c*]. Here, critical coupling in evanescently coupled PCN cavities is defined by the following criteria:

(PCN, 1) Critically-coupled PCN cavities are characterized by $\eta \approx 1$, meaning $T \approx 0$ on resonance.

(PCN, 2) If critical coupling cannot be achieved in a particular parameter space, we utilize the term near-critical coupling to define the local maximum in η observed in that parameter space, $\eta_{max} \leq 1$. This definition is particularly relevant to results in Sec. 2.4.

Under-coupled and over-coupled regimes for evanescently coupled PCN cavities are identified based on the Q_{total} and η of the side-coupled PCN cavity. Q_{total} and η can be directly determined from the transmission spectrum of the side-coupled PCN cavity. The over-coupled and under-coupled regimes are defined as:

(PCN, 3) Under-coupled cavities have narrow, shallow resonance dips ($Q_{u.c.} > Q_{c.c.}$ and $\eta_{u.c.} < \eta_{max}$).

(PCN, 4) Over-coupled cavities have broad, shallow resonance dips ($Q_{o.c.} < Q_{c.c.}$ and $\eta_{o.c.} < \eta_{max}$).

Utilizing Eqn. (2.7), we directly connect the coupling regimes to the ratio of Γ^c/Γ^0 in the system.

(PCN, 5) Critical coupling occurs when $\Gamma^c \gg \Gamma^0$, meaning $\Gamma^c/\Gamma^0 \gg 1$.

(PCN, 6) Over-coupling and under-coupling occur when $\Gamma^c \lesssim \Gamma^0$, meaning $\Gamma^c/\Gamma^0 \lesssim 1$.

With the criterion $\Gamma^c \gg \Gamma^0$, critical coupling for side-coupled PCN cavities occurs over a range of Γ^c/Γ^0. This allows critical coupling to occur over a range of w values instead of at a single w as shown in Fig. 2.4(b). The distinction between over-coupling and under-coupling PCN cavities lies in the value of Γ^0 and consequently Q_0. In the under-coupling and critically coupled regime,

Γ^0 and Q_0 do not change significantly. In the over-coupled regime, Γ^0 is larger and Q_0 is smaller than what is observed in the critically coupled and under-coupled case. The heightened intrinsic losses of the cavity when over-coupled are due to the large modal overlap between the PCN cavity and the feeding bus waveguide. The increased interaction in the over-coupled regime significantly increases unguided scattering from the cavity resonance and consequently reduces both η and Q_{total} from the critically coupled case. Over-coupling phenomena in PCN cavities has also been observed in [77].

We note the over-coupled region in Fig. 2.4(b) is centered around $w \sim 290$nm, near where data from Fig. 2.3(c) suggests $k_{cav} = k_{wg}$. This observation suggests that phase matching to PCN cavities may disproportionately increase Γ^0 compared to Γ^c, reducing the ratio Γ^0/Γ^c and increasing the potential to over-couple the cavity.

The over-coupling phenomenon results from the introduction of the bus waveguide increasing Γ^0. Solutions to avoiding this phenomenon include (1) *offsetting the two optical mode distributions in k-space* and (2) *ensuring a large enough coupling gap is used to control the evanescent field overlap between the cavity and bus waveguide*. In the cases probed through simulations and experiments in this paper, we show optimal configurations using non phase-matched conditions, but PCN cavities with phase-matched conditions could potentially operate with high η if a sufficient coupling gap is implemented to properly balance Γ^c and Γ^0.

2.4 Experiments

2.4.1 Photonic Crystal Nanobeam Cavity Design

As mentioned in Sec. 2.2.3, it is desirable to use a PCN cavity with high Q_0 for efficient side-coupling. Accordingly, we implemented a PCN design with sufficient taper length and mirror strength to realize a simulated $Q_0 \sim 10^6$. The fabricated PCN design had a target width of $nw =$ 700nm and period of $a = 350$nm with deterministic hole tapering from a radius of 105nm in the mirror segments to a radius of 127nm in the cavity region. The taper regions on either side of the

cavity center consisted of 20 unit cells each, and the mirror regions consisted of 10 unit cells each.

Differences in the bus waveguide and PCN dimensions between the 2D FDTD simulations (Sec. 2.3) and fabricated structures were required to compensate for the different mode confinement in a 2D simulation compared to a fabricated (i.e., 3D) structure. As stated earlier, the PCN width was decreased in simulation to nw = 600nm to better mimic the modal confinement in a fabricated PCN cavity with a traditional nw = 700nm width. The period a and radii of the PCN holes were accordingly adjusted in the fabricated PCN cavities to follow the deterministic design approach for a PCN with nw = 700nm in a 220nm thick SOI device layer [61, 78].

2.4.2 Method for Testing Effect of Wave-Vector Overlap

The sensitivity of device performance to variation in k_{wvg} demonstrated in Sec. 2.3 suggested the most practical way to measure the effects of k-vector mismatch and fabricate functional devices is to sweep the feeding bus waveguide width while maintaining a constant coupling gap size and PCN cavity geometry. Conceptually, this means we are holding k_{cav} constant while varying k_{wvg}. In this way, our experiments are able to tolerate deviations in the PCN cavity resonance conditions that arise from fabrication variation by having several side-coupled devices, each with a bus waveguide supporting a mode with a slightly different k-vector. We note that this type of empirical process optimization is commonly performed with resonant silicon photonic structures to account for device variation and additional loss factors that arise due to fabrication imperfections (e.g. roughness, size bias) that are not incorporated into simulations. We chose to sweep the waveguide width in a range around the $k_{cav} = k_{wvg}$ condition in order to experimentally observe all coupling regimes defined earlier. This fixed condition helps to constrain our side-coupler design and influences the choice of coupling gap in Sec. 2.4.4.

2.4.3 Side-Coupling Design Strategy

In order to efficiently side-couple from a straight bus waveguide into a PCN cavity, $\Gamma^c/\Gamma^0 \gg 1$ must be realized to achieve critical coupling. As described in this section, a practical method for

optimizing a side-coupling geometry to achieve this condition is the following:

(1) Simulate the PCN cavity without a side-coupled bus waveguide to obtain Q_0

(2) Identify practical design constraints on the bus waveguide coupling gap and waveguide width

(3) Set either the waveguide width or coupling gap as a constant value

(4) Sweep the free parameter and compute Q_{total} for each side-coupled system to determine Γ^c/Γ^0

(5) Choose a value of the free parameter which achieves large η and sufficient Q_{total}

Due to the manifestation of coupling and intrinsic losses in a side-coupled PCN, we can accurately estimate Q_0 in step (1) by simulating the cavity without the bus waveguide present. Step (1) can be used to verify that the PCN cavity design realizes high Q_0 for efficient side-coupling.

In step (2), constraints such as the resolution of lithography and fabrication tolerances can limit the parameter space for sweeping device design. A result of this could be limiting the smallest g used or the tolerance/resolution of w and k_{wvg} achievable.

Making either g or w a constant value in step (3) can further limit the parameter space for optimization. A good choice for this constant value should be where Γ^c is high compared to Γ^0. A small value of $g > 0$ compared to the evanescent tail length or a choice of w to place $k_{wvg} \sim k_{cav}$ but $k_{wvg} \neq k_{cav}$ would be adequate for satisfying this condition. Experimental data in Sections 2.4.6 and 2.4.7 shows that a value of k_{wvg} 1.5% larger or smaller than k_{cav} was sufficient to avoid over-coupling. Greater k-space offsets further reduce the chance of over-coupling the cavity.

By sweeping the free parameter in step (4), we can measure Q_{total} for the resonance mode and determine Γ^c/Γ^0 for each value of the free parameter. After the parameter sweep, each value of Γ^c/Γ^0 can be utilized to calculate η for the corresponding dimension of the free parameter. For the design of devices used in this paper, we sweep the coupling gap from 100nm to 500nm. The minimum coupling gap of 100nm was considered as it was slightly larger than what is feasible for fabrication. The maximum coupling gap of 500nm was considered as it is approximately one third of the wavelength of the fundamental resonance mode. The interaction region of an evanescent field may be approximated as one third of the wavelength in many cases as a rule of thumb. In

experiment we alter the k-space overlap by sweeping the bus waveguide width through a range 100nm larger and smaller than the width which satisfies the $k_{wvg} = k_{cav}$ condition determined by MODE Solutions calculations. We, however, experimentally observe measurable resonance peaks within a 7% offset range between k_{wvg} and k_{cav} which occurs within a waveguide range 50nm wider or narrower than the k-vector matched geometry. These results are discussed in greater detail in Sec. 2.4.4.

We note that a more precise and general way to simulate Γ^c/Γ^0 for each side-coupled cavity can also be computed using similar methods to those in [78]. In [78], the simulated flux and output modes at each field decay port are computed to directly extract Γ^c/Γ^0 in each simulation without utilizing a separate calculation of Q_0. The method in [78] is not used here as it requires greater computational resources to implement than the method proposed in this work.

2.4.4 Estimating Device Performance

We followed the design strategy outlined in Sec. 2.4.3 to determine a coupling gap which yields high η for $k_{cav} \sim k_{wvg}$. The discussed simulations considered the PCN cavity geometry detailed in Sec. 2.4.1. Simulations were completed via 3D FDTD methods using Lumerical FDTD. A non-uniform meshing parameter of 2 in Lumerical FDTD was used in these 3D calculations to reduce simulation resources. It is important to have the substrate present in these simulations if the substrate is present in experiment, as it can strongly affect both Γ^0 and Γ^c.

The steps from our design strategy were executed as follows:

(1) We excited resonant modes in the PCN cavity with a TE dipole source in the center of the cavity and monitored the field decay rate. From this field decay rate, we calculated $Q_0 = 1.0 \times 10^6$ for the fundamental PCN resonance mode without the bus waveguide present.
(2) Our simulation space was constrained to $g > 50$nm and we specified a step size for w no smaller than 10nm to be used in fabrication.
(3) The constraint $k_{wvg} \sim k_{cav}$ was set so we might use the platform to explore the effect of offsetting k_{wvg} from k_{cav} in experiment. This constraint led to a constant value of w = 480nm used for the

bus waveguide while sweeping g. In high resolution MODE Solutions calculations, w = 480nm set $k_{wvg} = k_{cav}$. The difference in meshing between the MODE Solutions simulations and FDTD computations, however, created a non-zero offset between k_{cav} and k_{wvg} in the FDTD simulations. The slight k-vector offset yielded $k_{cav} \sim k_{wvg}$ but $k_{cav} \neq k_{wvg}$. The k-vector offset between the high resolution MODE solutions simulations and low resolution FDTD simulations was large enough to avoid the over-coupling regime in these simulations, but using a more similar resolution between MODE solutions and Lumerical FDTD would lead to less of an offset between k_{cav} and k_{wvg}. We reiterate that experimental data in Sections 2.4.6 and 2.4.7 shows that a value of k_{wvg} 1.5% larger or smaller than k_{cav} was sufficient to avoid over-coupling. For utilization of high resolution in both effective index calculations and Q simulations, we recommend this minimum offset be observed. In the over-coupling regime, the approximation that Q_0 is constant does not apply. A more detailed method to calculate Γ^c/Γ^0, such as a method similar to what is used in [78], is necessary for estimating η in over-coupled PCN cavities.

(4) A small, relatively quick ($\sim$ 1 - 2 hours per simulation), parameter sweep of g was performed for $g = 100$nm to $g = 500$nm in 100nm increments. For each value of g, Q_{total} was computed. To calculate Γ^c/Γ^0 we utilized the equations

$$\frac{1}{Q_{total}} = \frac{1}{Q_0} + \frac{1}{Q_c} \Rightarrow Q_c = \frac{Q_{total}}{\left(1 - \frac{Q_{total}}{Q_0}\right)} \tag{2.8}$$

$$\frac{\Gamma^c}{\Gamma^0} = \frac{Q_0}{Q_c} = \frac{Q_0}{Q_{total}} - 1\,, \tag{2.9}$$

where Eqn. (2.8) is re-arranged from [78] and Eqn. (2.9) follows from Eqn. (2.1) with utilization of the result from Eqn. (2.8). After extracting Q_{total} for each simulated value and using the initially computed Q_0, we can easily find Γ^c/Γ^0 for each value of the swept parameter.

(5) For the bus waveguide present at g = 400nm with w = 480nm we measured $Q_{total} = 7.5 \times 10^4$, which corresponds to a calculated value of $Q_c = 8.1 \times 10^4$. Using the computed Q_{total} and Q_0 we see $Q_0/Q_{total} = 13.3$. Plugging this ratio into Eqn.(2.9), we see Γ^c/Γ^0=12.3. With this value of Γ^c/Γ^0, we can calculate the ideal coupling efficiency of this combination of bus waveguide width and

coupling gap to be $\eta \sim 0.995$ using Eqn. (2.7), fulfilling the requirements for critical coupling.

An important part of the decision to use a high ratio of Γ^c/Γ^0 in designing side-coupled cavities for fabrication is noting that fabrication imperfections can drastically alter performance from ideal metrics. We explicitly show in Sec. 2.4.7 that our experimental devices have significantly lower Q_0 than the simulated value presented above while the measured Q_c is close to the calculation detailed here. In general, fabrication imperfections will result in greater un-coupled scattering losses, lowering Q_0 and increasing Γ^0. Thus it is best to design a system with proper Q_c to work for a range of Q_0 lower than simulated values.

2.4.5 Experimental Device Fabrication

Side-coupled PCNs were fabricated to enable experimental verification of the simulated trends describing the effect of k-space overlap on coupling efficiency shown in Sec. 2.3. The devices were processed on a silicon-on-insulator (SOI) wafer with a 220nm thick silicon device layer and a 3μm thick buried oxide layer (SOITEC). Chips cleaved from these SOI wafers were coated with 300nm ZEP520A photoresist by spinning at 6000rpm for 45s. A JEOL93000FS tool was utilized to perform electron beam lithography. The photoresist was patterned with an electron beam at 100kV and 400 $\mu C/cm^2$ areal dosage. Patterns were developed after exposure with gentle agitation in xylenes for 30s followed by a rinse in isopropyl alcohol. The photoresist pattern was then transferred to the SOI device layer via reactive ion etching using an Oxford PlasmaLab100. Reactive ion etching was carried out with $C_4F_8/SF_6/Ar$ gases. Samples were cleaved after fabrication to expose the edges of the feeding waveguides to enable characterization in an end-fire coupling setup which is described in Sec. 2.4.6. Figure 2.5(a) shows a scanning electron microscope (SEM) image of one of the side-coupled PCNs studied in this work.

To efficiently couple into PCN cavities with $k_{wvg} \sim k_{cav}$ and explore the effects of k-space overlap on coupling, we fabricated two, nominally identically, sample sets consisting of uniformly designed PCN cavities with feeding bus waveguide widths ranging from $w = 380$nm to $w = 580$nm in 10nm increments, and a fixed coupling gap size of $g = 400$nm. The range of w fabricated cen-

tered around the value of $w = 480$, where high resolution MODE Solutions simulations predicted $k_{cav} = k_{wvg}$. A 100nm range of widths greater and less than $w = 480$ were fabricated to account for fabrication deviations. The coupling gap g = 400nm was chosen as a result of the preliminary simulations described in Sec. 2.4.4.

2.4.6 Experimental Transmission Data

The transmission spectra of the side-coupled PCN cavities were measured by coupling near-infrared light from a tunable laser (1500 to 1630nm, Santec TSL-510) into and out from the bus waveguides using polarization-maintaining lensed fibers (OZ Optics Ltd.), and detecting the output light intensity with a fiber-coupled avalanche photodiode photoreceiver (Newport 2936-C). TE optical polarization was utilized for resonance excitation and to acquire measured transmission spectra. Reflections at the ends of the waveguides from the fiber-coupled measurement method are the main source of noise in the transmission spectra of Fig. 2.5(b) due to Fabry-Perot interference.

In order to verify that the fundamental resonance of the PCN cavities was measurable in the transmission spectra, a separate PCN structure was fabricated to determine the approximate location of the band edge corresponding to the central cavity unit cell of the PCN cavities. This separate PCN comprised an array of air holes possessing the same unit cell geometry as that of the central cavity unit cell of the PCN cavities under test. The band edge of this PCN was located near 1520nm as seen in Fig. 2.5(b) for the spectrum labeled "MS = 0 Unit Cell Array". According to the deterministic design method, the fundamental resonance of a PCN cavity is located near the band edge wavelength corresponding to its central cavity unit cell. Experimental measurement of this band edge allows us to predict and verify the fundamental resonance position despite deviation in the fabricated PCN geometry from simulated design.

The metrics of η and Q_{total} of the side-coupled PCN cavities with different bus waveguide widths are summarized in Fig. 2.5(c). η was characterized by the relative transmission intensity of the resonance compared to the local baseline transmission intensity. Q_{total} was extracted from transmission spectra via Lorentzian peak fitting; we note that the fundamental resonance

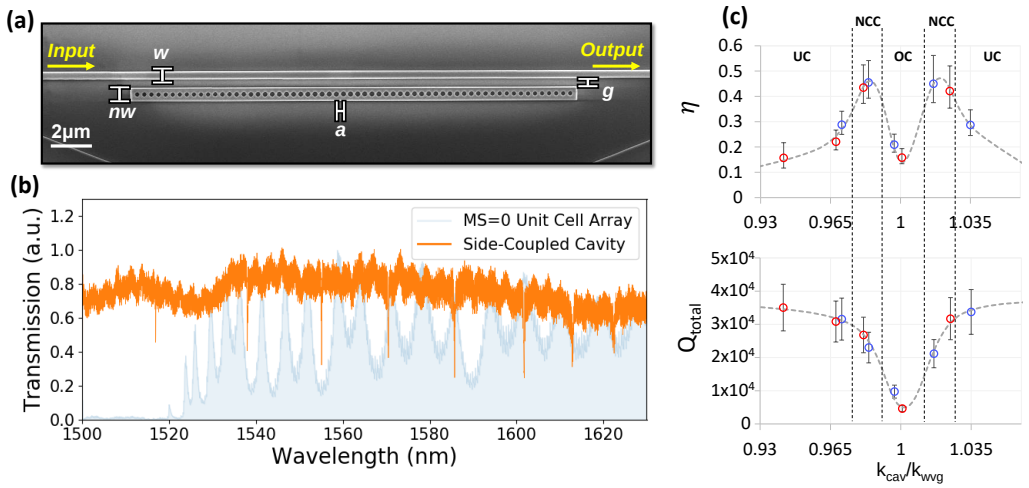

Figure 2.5: a) SEM image of side-coupled PCN cavity fabricated for experimental testing. b) Experimental transmission spectra for a side-coupled PCN cavity and MS=0 unit cell array. The band edge of the MS=0 unit cell array lies close to the side-coupled cavity resonance at $\lambda = 1518$nm, identifying it as the fundamental PCN resonance mode. c) Experimental data for η and Q_{total} of the fundamental resonance in side-coupled PCN cavities. Blue and red data points represent data taken from two separately fabricated sample sets. The dashed grey lines are cubic spline interpolated fits to act as a guide to the eye. Under-coupled, over-coupled and near critically coupled regions are denoted by **UC**, **OC** and **NCC**, respectively.

wavelength was similar for all measured PCN cavities fabricated on the same chip, varying from $1513\text{nm} - 1521\text{nm}$ and $1518\text{nm} - 1530\text{nm}$ for the devices represented by the red and blue data points, respectively, in Fig. 2.5(c). These slight resonance wavelength variations are due to minor fabrication variations between devices, but all resonance wavelengths are near the expected band edge position. In order to highlight the importance of k-space overlap, the relative resonance depth and Q of each of the measured side-coupled PCN cavities was plotted against the ratio of k_{cav} to k_{wvg}. Following Eqns. (2.2) and (2.3), k_{cav} was calculated from the PCN period, a, and k_{wvg} was calculated from the measured resonance wavelength and the effective index estimated from Lumerical MODE Solutions simulations that considered bus waveguides with the designed widths, w.

The data in Fig. 2.5(c) show that tuning of the bus waveguide wave-vector via a change in w enables control of the coupling regime of the side-coupled PCN cavity independent of coupling gap. As expected, large wave-vector mismatch, $k_{cav}/k_{wvg} \gg 1$ or $k_{cav}/k_{wvg} \ll 1$, leads to low energy

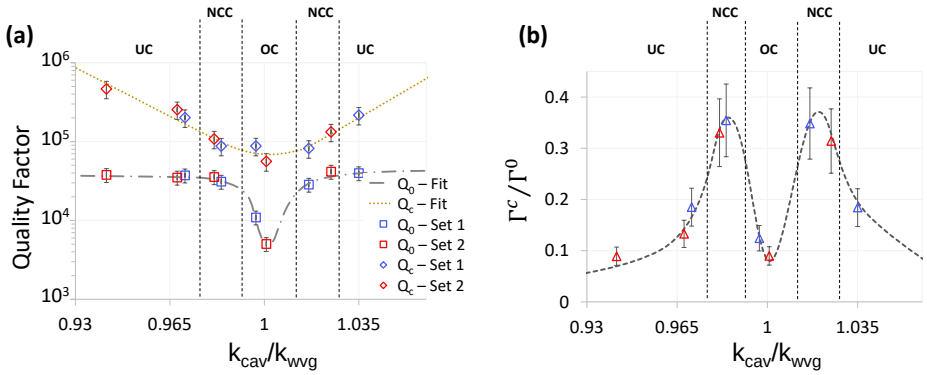

Figure 2.6: Plots of Q_0, Q_c and Γ^c/Γ^0 calculated from experimental data. Blue and red data points represent data taken from two separately fabricated sample sets. Under-coupled, over-coupled and near critically coupled regions are denoted by **UC**, **OC** and **NCC**, respectively. a) Data for Q_0 and Q_c. A clear decrease in Q_0 can be observed near $k_{cav}/k_{wvg} = 1$. b) Data for Γ^c/Γ^0. The trend in Γ^c/Γ^0 mimics the trend in η plotted in Fig. 2.5(c)

exchange and under-coupling of the resonator, as characterized by a low η and high Q_{total} of the measured fundamental transmission resonance. Close wave-vector matching, $k_{cav}/k_{wvg} \approx 1$, leads to drastically increased energy exchange; however, the lowered Q_{total} and small η are indicative of the over-coupled regime. A slight mismatch between k_{cav} and k_{wav} is necessary in this case to achieve near-critical coupling conditions.

The experimental trends shown in Fig. 2.5(c) are in excellent agreement with the simulated data in Fig. 2.4(b). The transmission spectrum of a near-critically coupled, side-coupled PCN cavity (k_{cav}/k_{wvg} = 0.98, w = 410nm) with multiple high contrast resonances is shown in Fig. 2.5(b). The resonance at $\lambda = 1518$nm corresponds to the fundamental mode of the PCN cavity with measured $Q_{total} = 2.6 \times 10^4$ and $\eta = 0.45$.

2.4.7 Calculation of Experimental Device Losses

We attribute the difference in the experimentally acquired η for near critically coupled devices and the value acquired from simulations in Sec. 2.4.4 to increased intrinsic losses in fabricated devices. The higher intrinsic losses most likely stem from fabrication imperfections. We can confirm this assumption by back-calculating Q_0 and Q_c from the experimentally measured Q_{total}

and η. By using the quadratic equation on Eqn. (2.7) to solve for Γ^c/Γ^0 and re-arranging Eqn. (2.9) to solve for Q_0, we get the expressions

$$\frac{\Gamma^c}{\Gamma^0} = \frac{-2\cdot(1-\eta)+\sqrt{4\cdot(1-\eta)^2+4\eta\,(1-\eta)}}{2\,(1-\eta)} \tag{2.10}$$

$$Q_0 = Q_{total}\left(\frac{\Gamma^c}{\Gamma^0}+1\right). \tag{2.11}$$

Utilizing these equations and Eqn. (2.9), we can calculate Γ^c/Γ^0, Q_0 and Q_c for the devices measured in our experimental data. This data is plotted in Fig. 2.6.

Fabricated devices in the under-coupled and near-critically coupled regime are calculated to have $Q_0 \sim 3\times10^4$ - 4×10^4. For these configurations, Q_c varies from 4.3×10^5 at the most under-coupled down to 8.2×10^4 in the near critically coupled region. The lowest value of Q_c in the near critically coupled region closely matches the simulated $Q_c = 8.1\times10^4$ from the calculation in Sec. 2.4.4. The data points in the over-coupled region show a drop in Q_0 to between 5×10^3 and 1×10^4 while the Q_c goes down to a minimum of 5.6×10^4. This data explicitly shows over-coupling phenomena as defined in Sec. 2.3.3.

The importance of the metric Γ^c/Γ^0 can also be clearly seen in Fig. 2.6(b) as its trend closely matches the trend in η from Fig. 2.5(c). By increasing the ratio of Γ^c/Γ^0, we can directly improve η for the the side-coupled PCN.

The calculation of experimental losses additionally shows that fabricated devices demonstrate lower Q_0 than simulated values while Q_c are measured at values close to simulated results in Sec. 2.4.4. We believe that fabrication imperfections which increase roughness and disorder reduce Q_0 more significantly than Q_c, making it more important to not only (1) *design side-coupled PCN cavities to have high* Q_0 but also (2) *make* Q_c *low enough to work with the range of* Q_0 *attainable by fabrication so a usable* η *may be achieved.*

2.5 Conclusion

Side-coupled PCN cavities demonstrate attractive capabilities such as serial integration, add/-drop filtering and multiplexing which are not readily attainable from in-line devices. To improve the utilization of side-coupled PCN cavities, we outline design guidelines (Sec. 2.4.3) that can enable critical coupling by appropriately tuning the ratio of coupling losses to intrinsic losses in a side-coupled PCN cavity.

By adjusting the coupling gap and bus waveguide width we are able to practically change the overlap between the PCN cavity and bus waveguide modes in both physical and k-space. Changing this overlap enables tuning of both the coupling and intrinsic losses of the resonator with a significant degree of independence, enabling high η. While most work assumes that maximal k-space overlap, or phase matching, of devices should enable optimal device coupling efficiency, we show for our particular devices that phase matching leads to over-coupling phenomena, as k-space matching reduces Q_0 compared to Q_c, lowering Γ^c/Γ^0. Therefore, a slight offset in k-space between the cavity and bus waveguide can yield the maximum coupling efficiency. By introducing a small offset in k-space, we realize a critically coupled PCN with calculated $\eta \sim 0.995$ and $Q_{total} = 7.5 \times 10^4$ in simulation and a near-critically coupled PCN with $\eta = 0.45$ and $Q_{total} = 2.6 \times 10^4$ in experiment. The generality of the analysis presented in this work should enable its application toward highly efficient coupling between other types of advanced photonic devices.

Chapter 3

Resonant Scattering in Photonic Crystal Nanobeams and Modal Identification

The following chapter is taken from a publication in Optics Express titled *"Camera detection and modal fingerprinting of photonic crystal nanobeam resonances"* [79]. This work focuses on using the resonant scattering profile of optical cavities as a form of "fingerprint" to identify the mode order of each resonance. To prove this concept, we demonstrate the following capabilities using scattering from a PCN cavity:

(I) Modal fingerprinting of resonances

(II) Scattered optical profile invariance to resonance peak shifts

(III) Improvement in SNR from spatial isolation of resonance structure

We also detail additional measurement considerations such as measurement triggering, camera detection range and data point density for improving the quality of the resonance scattering measurement.

3.1 Introduction

Nanophotonic devices such as ring resonators, photonic crystals, plasmonic structures and Fabry-Perot cavities enable numerous optical applications, including signal processing [11, 23, 80], optical nanomanipulation [4, 5], sensing [6, 37, 65], quantum computing [81, 82] and optomechanics [13, 14, 83], in platforms compatible with dense integration and on-chip implementation. The appeal of these devices largely hinges on their ability to spatially and temporally localize light. As this ability of nanophotonic devices to confine light in time (given by the quality factor, Q) and space (given by the mode volume, V_m) is dependent on the properties of their available optical modes, it is crucial that optical modes be reliably identified so the appropriate mode(s) may be utilized for a given application.

Currently, experimental identification of mode order in nanophotonic devices has been done by

either relating measured modal features (such as resonant peaks in transmission or reflection) to simulated results [78, 84], or through direct, near-field measurements such as near-field scanning optical microscopy (NSOM) [20]. While comparison of measured modal features to simulated results is widely used for determining mode order, devices with high spatial or temporal optical confinement are highly sensitive to small changes in device dimensions such that small deviations between simulated and fabricated geometric dimensions can lead to large shifts in resonant features. Furthermore, in some cases, the lowest order modes may not be measurable [85]. Hence, the comparison between simulation and measurements for mode identification is less reliable for devices with low V_m or high Q. NSOM is able to circumvent these issues through direct field measurements of excited optical modes; however, it is a relatively complex technique which is not yet widely available for measurement of guided wave photonic structures.

This work aims to show it is possible to gain information about the mode order of nanophotonic devices by taking advantage of the portion of the mode which couples to free-space propagation and then utilizing the resulting resonant scattering measured in the far-field as a "fingerprint" for identifying mode order. To this end, we analyze the out-of-plane scattering from a photonic crystal nanobeam (PCN) cavity with a standard infrared (IR) camera and demonstrate identification of mode order via modal fingerprinting. We additionally show that it is possible to realize an improved signal-to-noise ratio for PCN resonance features from camera measurements. Utilization of a camera instead of a single photodetector enables spatial isolation of resonance features from noise in the optical signal line. The spatial information provided by camera measurements allows for improved resonance characterization and higher sensitivity measurements of PCN cavities when fabrication imperfections generate significant signal noise. We note that previous work has shown IR cameras may be used for sensing in coupled-resonator optical waveguide (CROW) systems [86], characterizing optical propagation in side-coupled integrated spaced sequence of resonators (SCISSOR) and photonic crystal waveguides [87, 88], and detecting scattering from Fabry-Perot and photonic crystal cavity modes [58, 89].

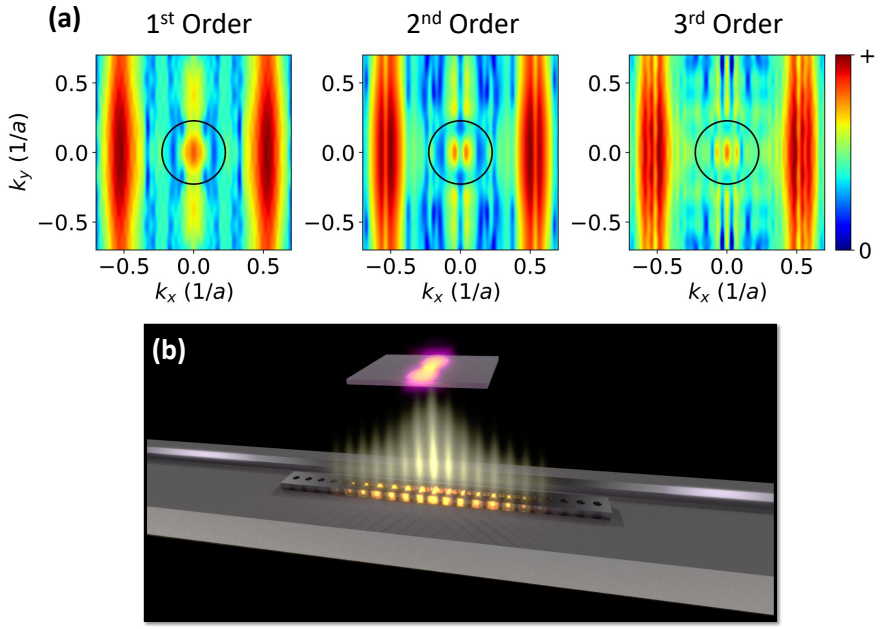

Figure 3.1: (a) k-space profiles for the first three resonance mode orders in a PCN cavity. The leaky region of k-space is enclosed in the black circles. Within the leaky region, we observe the mode shape changes with mode order. (b) Illustration of detection scheme. Resonance mode excitation in PCN cavities leads to out-of-plane scattering according to the mode shape in the leaky region. Excitation of different mode orders produces different scattering patterns in the far-field that can be detected by a camera.

3.2 Overview of Technique

3.2.1 k-Space and Modal Fingerprints

Optical modes of varying order in nanophotonic devices generally have distinct spatial field profiles and, consequently, have distinct profiles in k-space. The portion of the optical modes in k-space which overlap with k-vectors supported in free-space can be used to directly examine modal properties in the far-field. This leaky region of the mode in k-space, which can be measured in the far-field, may then act as a readily detectable ”fingerprint” by which mode order can be identified for a wide range of nanophotonic devices, including PCN cavities. The k-space profiles of the first three resonance mode orders in a PCN cavity are shown in Fig. 3.1(a). The design of this PCN cavity is specified in Sec. 3.3.1.

Figure 3.1(b) illustrates that the only requirements to measure the modal fingerprint of a PCN

resonance mode are to simply excite the resonant mode and then measure the scattering in the far-field with a camera. To excite PCN resonances, this work utilizes evanescent coupling (see Sec. 3.3), but we note it is also possible to fingerprint PCN modes using an in-line coupling configuration under certain circumstances (see Sec. 3.6.1).

3.2.2 Considerations for Out-of-Plane Detection

For the detection of out-of-plane resonance scattering in photonic devices, there are two primary considerations. (1) devices must have sufficient out-of-plane scattering and (2) non-resonant scattering should be minimized. In general, most fabricated, resonant photonic devices exhibit out-of-plane resonant scattering due to overlap of the resonance mode with the leaky region of k-space. Even high Q cavities that have been designed to minimize overlap with the leaky region in k-space may experimentally demonstrate out-of-plane scattering due to a non-zero overlap with the leaky regions in k-space and fabrication imperfections increasing the overlap of the resonance mode with the leaky region.

Measurement of resonance scattering profiles requires that the resonance scattering intensity is sufficiently large compared to the background signal noise. The intensity of background scattering will largely be dependent on the method of resonance excitation. In-plane, edge-coupling to resonant devices such as Fabry-Perot resonators or photonic crystal cavities can introduce large scattering intensities at the interface between the resonator and the feeding optical mode if the coupling efficiency to the resonator is low. Out-of-plane, free-space coupling to resonators will also introduce a significant amount of non-resonant scattering and reflections at the surface of the device, but this may be filtered out with the proper use of polarizers and resonator orientation [55, 67]. In-plane, evanescent coupling to resonant modes with a low-loss waveguide will generally produce low background scattering as energy is coupled between devices via evanescent tails with low field intensity.

3.3 Design and Simulations

3.3.1 Side-coupled PCN Cavity Specifications

To demonstrate modal fingerprinting using a camera, we choose to test an evanescently side-coupled PCN cavity because it is relatively straightforward to minimize non-resonant scattering in such a structure [62]. For the PCN cavity tested in this work, we utilized a cavity taper length of 20 unit cells from the center of the cavity to the edge of the mirror regions and mirror regions of 10 extra unit cells. Devices were designed for fabrication on a 220nm thick device layer on silicon-on-insulator (SOI) wafers with a 3 μm buried oxide layer (BOX) for insulating the cavity mode. A hole period of 350 nm and PCN width of 700 nm were utilized to move the resonance mode away from the light cones in air and glass. The mirror strength curve utilized for the unit cells in the cavity taper was computed from MIT Photonic Bands (MPB) simulations and is shown in Fig. 3.2(a). We linearly tapered the hole radius from 127nm in the center of the cavity to 108nm at the edges of the cavity. To adequately side-couple into resonance modes, we utilize a coupling gap of 400nm and straight bus waveguide width of 410nm for appropriate overlap of bus waveguide and cavity modes in both physical and k-space [62].

3.3.2 Addressing Considerations for Out-of-Plane Detection

To (1), verify our designed PCN geometry had adequate out-of-plane scattering on resonance, we simulated resonance mode excitation (specified in Sec. 3.3.3) and monitored the optical flux both out of plane and at the edge of the cavity. Figure 3.2(b) shows significant out-of-plane scattering on resonance for our PCN design when excited.

To (2), reduce non-resonant scattering, we chose to utilize a side-coupled configuration with a straight bus waveguide to evanescently excite PCN resonance modes. We present guidelines on how to side-couple to PCN cavities with a straight bus waveguide in previous work [62]. Implementing a straight side-coupled bus waveguide instead of a curved side-coupled bus waveguide reduces scattering due to bending losses in a curved bus waveguide. We note it is possible to ob-

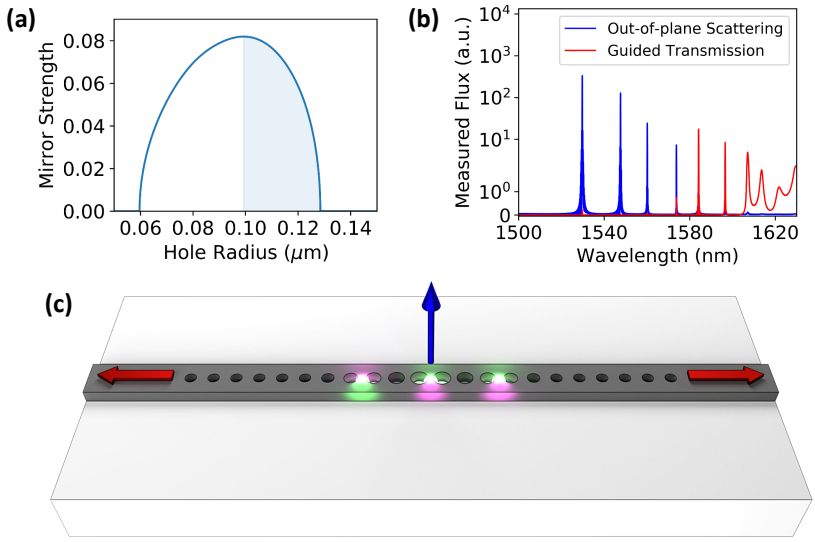

Figure 3.2: (a) Mirror strength curve used in cavity design. The shaded region under the curve corresponds to hole radii used in creating PCN cavities with dielectric mode cavity resonances. (b) Measured flux from out-of-plane scattering (blue) and in-plane guided transmission (red) from PCN resonance excitation with 3 dipole sources. Lower order, more well confined modes are observed to scatter more selectively out-of-plane rather than coupling into guided modes. (c) Illustration of dipole configuration used to excite resonance modes. Actual dipole positions used were at the center of the cavity and $\pm 2.1 \mu$m from the center of the cavity. The two outer sources had a π phase offset to excite even order modes.

serve mode-dependent resonance scattering with an in-line configuration which couples light in directly from the edge of the PCN cavity. Scattering noise from coupling through the edges of the cavity can be reduced by increasing the coupling efficiency to resonance modes, but this generally reduces the loaded Q of resonance modes (see Sec. 3.6.1).

3.3.3 Simulation Specifications and Modal Profiles

Far-field scattering profiles of resonance modes were computed via 3D calculations in Lumerical FDTD Solutions. These simulations were run for 6000fs simulation time and with an auto non-uniform meshing factor of 5. To computationally excite PCN resonance modes, we utilized 3 dipole sources placed at different points in the PCN cavity, as illustrated in Fig. 3.2(c). Two dipole sources were placed at $\pm 2.1 \mu$m from the cavity center with separate phases of 0 and π. Another dipole source was placed at the center of the cavity with a phase of 0. The phase offset between the

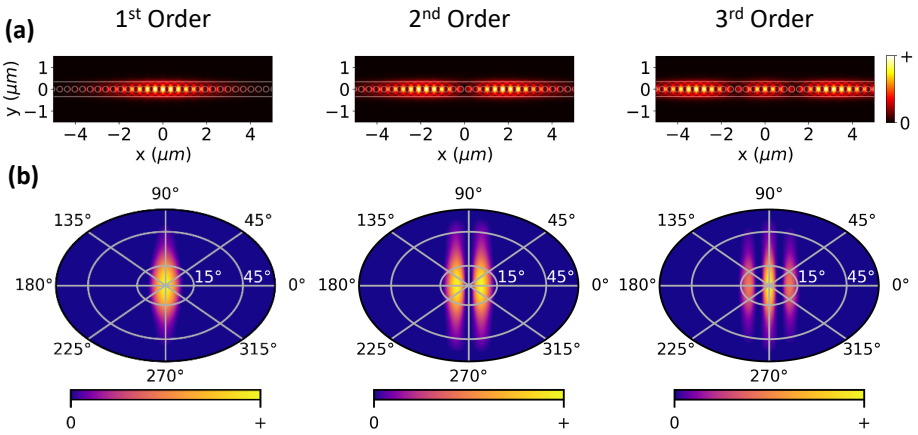

Figure 3.3: (a) Spatial field profiles for the first three resonance modes in the designed PCN cavity. (b) Calculated scattering in the far field for the first three resonance modes. It is clear that each near field profile in (a) is uniquely connected to a far-field pattern in (b).

non-central sources was utilized to excite even order modes in the PCN while the central dipole source was used to excite odd order modes. The placements of the sources were chosen to tune the spatial field overlap between the dipole sources and the modes into which they constructively coupled.

The spatial field profiles of the first three PCN cavity modes are illustrated in Fig. 3.3(a). To calculate the far-field of the resonance modes, a field monitor was utilized to capture the electric and magnetic field components of the resonance modes $\sim$ 170nm above the cavity. The far-field scattering profile was then extrapolated using the near field components and propagating them into the far-field using standard FDTD methods [90, 91]. The calculated far-field scattering profiles are shown in Fig. 3.3(b). The far field patterns for each resonance mode simulated are uniquely dependent on the mode order and are similar in shape to the k-space profiles of each mode in the leaky region shown in Fig. 3.1(a). The dependence of scattering on mode order enables the use of resonance scattering patterns as ”fingerprints” for identifying resonance modes. Scattering patterns from higher order modes are discussed in Sec. 3.6.2.

3.4 Experiments

3.4.1 Fabrication Method and Characterization Setup

To experimentally demonstrate modal fingerprinting and compare scattering and transmission line measurements, we fabricated side-coupled PCN cavities using electron-beam lithography (EBL) and reactive ion etching (RIE). Devices were fabricated on chips from a silicon-on-insulator (SOI) wafer with a 220nm thick silicon device layer and a 3μm thick buried oxide layer (SOITEC). To pattern devices on the chips, we spin-coated 300nm of ZEP520A photoresist at 6000rpm for 45s and exposed the resist using a JEOL93000FS EBL tool. The photoresist was patterned with an electron beam at 100kV and 400 $\mu C/cm^2$ areal dosage. Patterns were developed after exposure with gentle agitation in xylenes for 30s followed by a rinse in isopropyl alcohol. The photoresist pattern was then transferred to the SOI device layer via RIE using an Oxford PlasmaLab100. RIE was carried out with C_4F_8/SF_6/Ar gases. Samples were cleaved after fabrication to expose the edges of the feeding waveguides to enable characterization in an end-fire transmission setup. An SEM image of a fabricated, side-coupled PCN cavity is shown in Fig. 3.4(a).

The transmission spectra of the side-coupled PCN cavities were measured by coupling near-infrared light from a tunable laser (1500 to 1630nm, Santec TSL-510) into and out from the bus waveguides using polarization-maintaining lensed fibers (OZ Optics Ltd.), and detecting the output light intensity with a fiber-coupled avalanche photodiode photoreceiver (Newport 2936-C). TE polarized light was utilized in the experiments.

The scattered optical profile was measured in an InGaAs camera (New Imaging Technologies WiDy SWIR 640U-S) through a 20x, large working distance (20 mm) objective (Mitutoyo Plan Apo NIR) with a numerical aperture (NA) of 0.40. We note that an essential element in detecting resonant cavity scattering requires matching the cavity scattering angles with the measurable angle range associated with the NA of the implemented objective. As much of the simulated scattering depicted in Fig. 3.3(b) occurs within 15° of normal incidence, we found it sufficient to use NA = 0.40 in this work, which corresponds to an acceptance angle of $\sim 24°$ for the objective.

Utilizing the end-fire setup to couple light into a bus waveguide, we evanescently excite the cavity resonance mode and measure the scattered light with an IR camera. The captured video from the camera was processed with ImageJ to spatially isolate the scattering around the device for analyzing average scattering intensity as a function of wavelength. We additionally measure light transmitted through the bus waveguide for verification of resonance wavelength position and performance comparison. No extra polarizers or filters are used in our camera measurement. Objectives with larger NA could be used to resolve higher order resonance scattering from higher scattering angles.

3.4.2 Experimental Data

Experimentally measured resonant scattering profiles, transmission spectra, and scattered optical intensities for the fabricated PCN are shown in Fig. 3.4. For clarity, it is important to explain that the data in Fig. 3.4(b-d) and Fig. 3.4(e-g) are from the same physical device, but have been taken with different data collection parameters and with different levels of surface adsorbed water, which alter the measurement quality and position of resonance peaks, respectively. Accordingly, data from Fig. 3.4(b-d) will be referred to as measurement 1 (M1) and Fig. 3.4(e-g) will be referred to as measurement 2 (M2) in this paper. With this data, we demonstrate (I) modal fingerprinting of resonances, (II) scattered optical profile tolerance to resonance wavelength shifts and (III) improvement in SNR from spatial isolation of resonance structure. We also show how measurement considerations such as (i) data point density and (ii) digital detection range can be used to improve measurement quality.

To (I), demonstrate modal fingerprinting of resonances, we measured the transmission spectrum of side-coupled PCN devices while simultaneously recording video data of the scattered light. As the wavelength of the input laser light was swept, dips appeared in the transmission spectrum on resonance (Fig. 3.4(c,f)). At these resonance wavelengths, we additionally observed increased scattering in the video data from the camera (see Visualization 1 in Fig. 3.4). The peaks in scattering intensity shown in Fig. 3.4(d,g) correspond directly with dips in the transmission

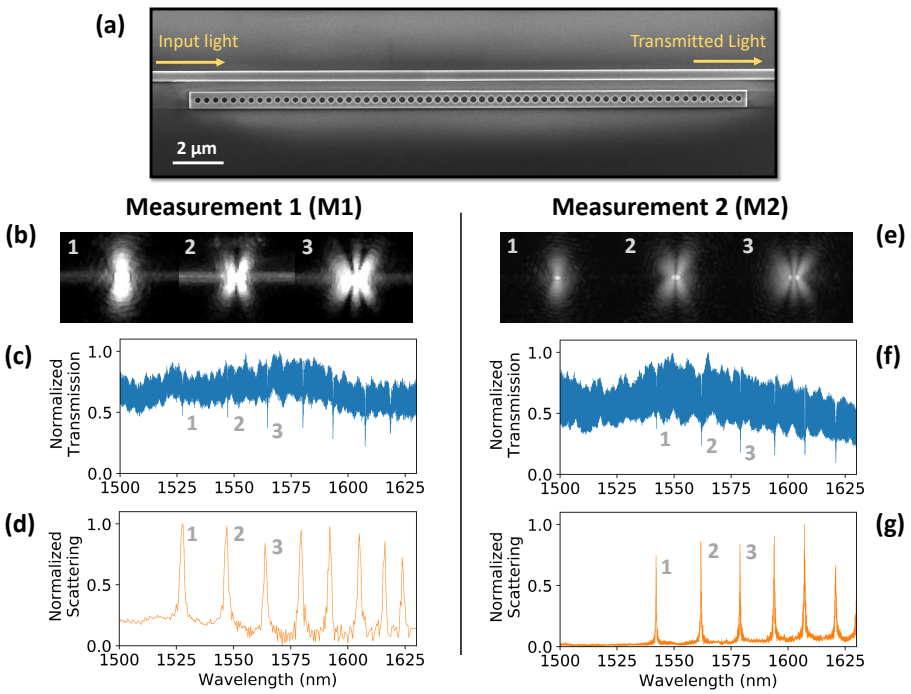

Figure 3.4: (a) SEM image of fabricated, side-coupled PCN cavity. The optical input from the end-fire setup feeds the bus waveguide. The transmitted light through the bus waveguide is sent to a detector to characterize resonance peaks. The out-of-plane resonantly scattered light from the cavity is captured with an IR camera (see Visualization 1 for video data used in M2). (b) Scattered optical profiles recorded by an IR camera for resonances labeled (1), (2) and (3) for M1. The resonance spectrum was measured via (c) transmission through bus waveguide and (d) average scattering detected by IR camera for M1. (e) Scattered optical profiles for resonances labeled (1), (2) and (3) in M2. The resonance spectrum was measured via (f) transmission through bus waveguide and (g) average scattering detected by IR camera for M2. A higher data point density and modified digital detection range were used for M2.

spectra shown in Fig. 3.4(c,f). As seen in Fig. 3.4(b,e), the first three resonance modes imaged by the camera yield unique scattering profiles, demonstrating that the scattered optical profile may be utilized to identify resonance mode order in these devices. Experimentally measured scattering profiles of higher order modes are discussed in Sec. 3.6.2.

In order to (II), show the scattered optical profile is tolerant to resonance peak shifts, we measured side-coupled PCN devices before (M1) and after (M2) prolonged exposure to ambient humidity in an unregulated environment. We utilized the exposure to ambient humidity to induce adsorption of water on the surface of the devices and increase the refractive index of the cavity, red-shifting the resonance wavelengths, as shown by comparing Fig. 3.4(c,d) and Fig. 3.4(f,g).

Because this prolonged humidity exposure was unregulated, we simply use it to qualitatively show the resonance scattering pattern is preserved upon resonance peak shifting, as the resonance profile in real and k-space is not significantly perturbed. While the pixel ranges and saturation settings are different between M1 and M2, we see that the shape of resonance scattering in Fig. 3.4(b,e) is clearly preserved between the two measurements. We note that the $\sim$ 15nm resonance red-shift between M1 and M2 from extended exposure to ambient atmospheric conditions occurs within a reasonable range when compared to previous results on photonic crystal cavities used as humidity sensors [92, 93].

We additionally show that (III), improvement in SNR from spatial isolation of the PCN resonance structure can result from implementing camera detection of resonant scattering. Noise in transmission line measurements from Fig. 3.4(c,f) results from Fabry-Perot interference caused by reflections from the waveguide facets at the edges of the end-fire coupling setup, waveguide edge roughness, and stitching errors which occur during EBL. In general, it is possible to reduce this noise in the transmission line by various means, but in practice this can be difficult and requires further development of fabrication processes. By utilizing a camera to detect local resonance scattering, we can spatially isolate the PCN cavity from imperfections and reflections in the bus waveguides. This results in an improved SNR relative to the transmission line measurements. In the data from M2 where we have improved our scattering measurement, Fig. 3.4(f,g), we calculate the SNR of the fundamental resonance mode to be 2.10 dB from transmission line measurements and 21.4 dB from measurement of scattered light. These SNR values were calculated by considering the resonance peak height with respect to the standard deviation of the local signal baseline. A Q of $\sim 6 \times 10^3$ was measured for the fundamental resonance by both techniques in M2. A comparison of the two SNR values from the two methods shows a 19.3 dB increase in the SNR by utilizing the scattered light to measure resonance peaks. We attribute this improvement to camera measurements enabling the spatial isolation of cavity scattering from guided and un-guided scattering in the feeding waveguides.

To improve the measurement quality of scattered optical profiles and resonance peak widths

with the camera, we altered (i) data point density and (ii) digital detection range between M1 and M2. To (i) alter the data point density in the spectrum measured by the camera, the wavelength scan rate of the tunable laser source and the captured frames per second (fps) of the camera were adjusted. In M1 (Fig. 3.4(d)), a laser scan rate of 10nm/s and a 24fps constant camera capture rate were utilized. In M2 (Fig. 3.4(g)), a laser scan rate of 1nm/s was utilized and each video frame capture was triggered by the laser at 0.04nm intervals, giving an average frame rate of 25fps. The reduced laser scan rate and higher frame rate of the camera enabled much higher point density in the measured spectrum. The difference in frame-rate and scan speed results in M1 having a spectral resolution of 0.42nm while M2 has a spectral resolution of 0.04nm. Further slowing of the scan rate can be achieved, but this can lead to increasingly large data files as each data point corresponds to a camera image. The uncompressed video file from the camera utilized for extracting the spectrum in M2 had a file size of $\sim$ 1.5 GB. More advanced spatial selection during data capture or file compression could reduce this data requirement.

The (ii) digital detection range of the camera measurements were also adjusted between M1 and M2 to improve measurement quality. The automatic, real-time adjusted image settings used in M1 show clipping behaviour in the images of resonance scattering profiles (Fig. 3.4(b)). This reduces the contrast in the scattered profile and potentially hinders resolution of resonance peak shape in the measured spectra shown in Fig. 3.4(d). To reduce clipping behavior, we manually adjusted the data capture range of the camera to make the maximum pixel capture value high enough to reduce clipping and the minimum pixel capture value low enough to not filter out resonant scattering. This results in data in M2 (Fig. 3.4(e)) showing more contrast and clarity in the resonant scattering image compared to M1.

3.5 Conclusions

The performance of nanophotonic devices hinges on the properties of their supported optical modes. As the different optical modes of a nanophotonic device have different properties and performance metrics, it is crucial to be able to identify different mode orders so the appropriate

mode(s) may used in applications. This is particularly true for photonic crystals, as their resonance Q, V_m and spatial field profiles achieved are highly dependent on mode order. We demonstrate it is possible to utilize mode dependent overlap with the leaky region as a "fingerprint" to identify mode order in nanophotonic devices by analyzing the far-field scattering from PCN cavity resonances. In this work, an IR camera and a side-coupled PCN are implemented to show (I) modal fingerprinting of resonances, (II) scattered optical profile tolerance to resonance peak shifts and (III) improvement in SNR from spatial isolation of resonance structure. It is also shown that measurement considerations such as (i) data point density and (ii) digital detection range can be used to improve measurement quality. Because PCN modes can be accessed by both in-line or side-coupled excitation, modal fingerprinting can identify modes in in-line devices either directly from device scattering or indirectly via scattering of a comparable test device which is either side-coupled or has high coupling efficiency for in-line excitation (see Sec. 3.6.1). By demonstrating modal fingerprinting via resonance scattering, we lower the technical threshold for more comprehensive characterization of modes in nanophotonic devices and leveraging the desired modal properties for targeted optical applications.

3.6 Supplementary Material

3.6.1 Modal Fingerprinting in In-Line PCN Cavities

Modal fingerprinting can be utilized for PCN cavities in an in-line configuration, although identification of resonance modes is more challenging in cases when there is significant scattering from the edges of the cavity. Figure 3.5 shows experimental resonant scattering profiles for PCN cavities in an in-line coupling configuration where light is coupled into resonance modes through the edge of the cavity. By varying the number of extra mirrors after the cavity taper, the confinement of resonance modes is altered and consequently changes the coupling efficiency for each mode. The coupling efficiency, η, for a PCN in an in-line coupling configuration is given by

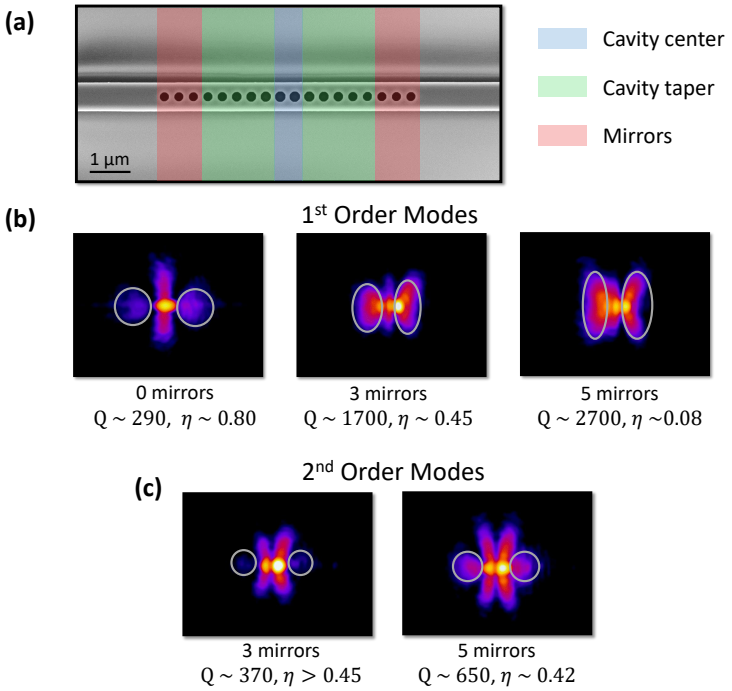

Figure 3.5: SEM of in-line PCN and experimental images of resonant scattering from in-line PCN cavities with no side-coupler present. Excess scattering from the edges of the cavity are circled in grey. False color is used to enhance contrast in the scattering images. Loaded Q and approximate η values are reported for resonances in (b) and (c). (a) SEM of a measured PCN cavity in an in-line coupling configuration. The blue, green and red highlighted regions correspond to the cavity center, cavity taper, and extra mirrors added, respectively. (b) Images of scattering from first order modes in separate devices with different numbers of extra mirrors added after the cavity taper. (c) Images of scattering from second order modes in separate devices with different numbers of extra mirrors added after the cavity taper.

$$\eta = \mathrm{T_{res}} = \frac{(Q_0/Q_c)^2}{(1+Q_0/Q_c)^2}, \tag{3.1}$$

where $\mathrm{T_{res}}$ is the transmittance on resonance, Q_0 is the intrinsic quality factor of the resonator and Q_c is the coupling quality factor of the resonator. Because η is related to the ratio Q_0/Q_c, PCN resonances with high Q_c relative to Q_0 demonstrate low η. Resonance modes with high Q_{loaded} often have high Q_c and low η, making them difficult to identify by modal fingerprinting in an in-line configuration.

An SEM image of one of the in-line coupled PCN cavities that was measured using the far-field scattering technique is shown in Fig. 3.5(a). All of the in-line PCN cavities that were measured

were designed with hole tapering from a hole radius of 127 nm at the cavity center to 112 nm at the edges of the cavities with a taper length of 5 unit cells. All other dimensions of the nanobeam are identical to the side-coupled devices discussed earlier. The number of mirror unit cells at each end of the PCN was varied to modify the coupling efficiency. The larger radius at the cavity edges and smaller cavity taper were utilized to lower Q_c and non-resonant scattering from the cavities. To estimate η, we compared the transmitted power of PCN cavities on resonance to the transmission through a reference waveguide. Fig. 3.5(b,c) shows that the edge scattering (the circled grey regions) tends to increase with reduced η.

To circumvent the difficulty of modal fingerprinting in-line, high Q (and low η) cavities, it is possible to identify resonances without direct modal fingerprinting of the cavity. The peak positions and modal fingerprints of a side-coupled cavity could be used to identify modes of an in-line cavity with the same geometry, as side-coupling does not significantly perturb the peak positions or modal fingerprint in the weak coupling regime. An in-line device with fewer mirrors or taper segments for higher η could also be used to identify the modes of the higher Q device so long as the device changes do not significantly alter the general resonance shape and peak positions between the devices.

3.6.2 Fingerprinting Higher Order PCN Modes

The simulated scattering for fourth and fifth order resonance modes in the side-coupled PCN cavity (see SEM image in Fig. 3.4(a)) are shown in Fig. 3.6(a). The tight angular packing and wider angle range of scattered light in these higher order modes makes them more difficult to resolve in the camera images shown in Fig. 3.6(b). Increasing camera resolution (640×512 pixels in the camera used here) or utilization of a higher power objective (20x used here) could further improve the ability to resolve higher order modal fingerprints.

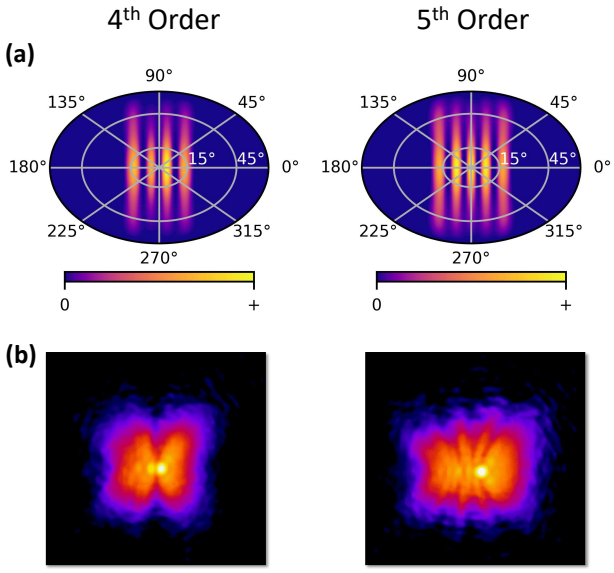

Figure 3.6: Side-by-side comparison of (a) simulated scattering profiles and (b) experimentally measured images of resonance scattering for the fourth and fifth order resonances of the fabricated side-coupled PCN cavity. False color is used in the measured scattering data to enhance contrast in the images.

Chapter 4

Wavelength Filtering with Photonic Crystals in a Monolithic Technology

The following chapter is taken from a publication in Photonics Technology Letters titled *"O-Band Subwavelength Grating Filters in a Monolithic Photonics Technology"* [94]. The work here focuses on the application of PCNs for wavelength filtering devices fabricated in a monolithic photonics technology. This work expands upon the previous investigation of photonic crystals in this thesis by shifting focus from photonic crystals which primarily use bandgap properties for applications to photonic crystals which operate farther away from the bandgap and use the periodic index variation for diffraction-based applications. PCN devices in this category of applications are often referred to as subwavelength grating (SWG) or Bragg filtering devices in the literature [95–103]. For a more detailed overview of the theory and formalism governing this class of devices, I personally recommend reading [101] for more depth. This chapter, however, should help provide a more intuitive overview of how these devices work and how to quickly design a SWG filter.

4.1 Introduction

As global datacom performance demands continue to increase, commercial and academic sectors continue to investigate how communications technology can evolve to satisfy growing consumer needs. One of the greatest factors currently limiting datacom bandwidth and energy efficiency lies in short-range (< 2 km) interconnects which transmit data inside datacenters. The recent trend to combat this bottleneck has been for companies to switch from electrical to optical interconnects, as optical interconnects are able to simultaneously reduce parasitic losses and increase bandwidth compared to their electrical counterparts [104].

The bandwidth increase for optical interconnects is enabled in large part by wavelength-division multiplexing (WDM). In WDM, various data channels are encoded onto separate wavelengths of light which can propagate together in a single waveguide or fiber and can be routed to other waveg-

uides and fibers. By combining multiple wavelength channels of light into a single optical interconnect, the interconnect bandwidth can be multiplied by the number of wavelength channels used. Since WDM techniques can be used in addition to pulse-amplitude modulation (PAM) and quadrature amplitude modulation (QAM), enormous data rates $>$ 1Tb/s could potentially be realized for individual optical interconnects [105].

Despite large improvements to power consumption, bandwidth and cost scaling of optical interconnects over their electrical counterparts, transitioning to optical interconnects incurs an implementation cost of purchasing optical transceivers that process the electro-optical signal conversion in the form of a discrete device [105]. To reduce the cost of optical transceivers, GLOBALFOUNDRIES (GF) have pioneered monolithic silicon photonics technologies that enable the large-scale fabrication of photonics and CMOS technologies on the same chip [106].

To realize WDM functionality in photonic integrated circuits (PICs) on a CMOS technology platform, many photonic filtering approaches have been explored, including arrayed waveguide gratings (AWGs), Echelle gratings, cascaded Mach-Zehnder interferometers (MZIs) and coupled rings [107–109]. While these devices work with features readily compatible with commercial photolithography, demonstrated performance in the categories of channel width, insertion loss, channel shape and active tunability either make them unsuitable for many commercial applications or leave significant room for improving performance or implementation.

Prior work has explored utilizing subwavelength structuring to improve the performance of photonic devices [110]. Recent work on add/drop subwavelength grating (SWG) filters has shown great promise for achieving low losses, low crosstalk, flat-top channel shapes and channel widths spanning CWDM and DWDM requirements in a serially cascadable and modular platform [96, 99–101]. However, the small feature sizes of SWG filters are typically realized using electron beam lithography, which is incompatible with commercial fabrication. Pushing UV lithography in CMOS foundries to resolve such features has been explored to overcome this hurdle [95, 101, 111, 112]. Moreover, most prior work with add/drop SWG filters has been conducted in the C-band [96, 99–101] while the industry standard for datacenter applications is O-band operation [105].

Investigating the performance and manufacturability of SWG filters in the O-band is critical for exploring their potential to advance integrated photonics in data communications [95]. Towards this goal, we demonstrate the first add/drop SWG filters in the O-band manufactured in a CMOS foundry using a tape-out on the 90nm, monolithic silicon photonics technology at GF.

4.2 Device Operation Concept

Many SWG filters are designed to operate based on contra-directional reflection [101]. Compared to conventional Bragg gratings, this configuration produces low back-reflection, which is advantageous for implementation with a laser [95, 97]. Contra-directional reflection is generally induced by a periodic corrugation (a general form of a grating) acting on the field of a waveguide mode. In the configuration reported here (Fig. 4.1), a SWG acts on the evanescent field of a bus waveguide mode and, for one frequency band, couples the waveguide mode to the backward propagating SWG mode. An intuitive explanation of this effect is that for one frequency band, first order grating diffraction provides sufficient momentum change in the waveguide mode to evanescently couple it into the backwards propagating SWG mode.

More formally, as the evanescent field of the waveguide mode interacts with the grating, the propagation vector of the mode, β_{wvg}, changes according to the grating diffraction relation:

$$\beta_m = \beta_{wvg} + \frac{2\pi \cdot m}{\Lambda} \tag{4.1}$$

where Λ is the pitch of the grating (shown in 4.2), m is an integer (either positive or negative) and β_m is the resulting wave-vector from mth order diffraction. Given a SWG guided mode with propagation vector β_{SWG}, it is possible to contra-directionally diffract the evanescently coupled waveguide mode, with propagation vector β_{wvg}, into the SWG by choosing $m = -1$ in (4.1) and setting $\beta_{-1} = -\beta_{SWG}$, giving

$$-\beta_m = \beta_{wvg} - \frac{2\pi}{\Lambda} \tag{4.2}$$

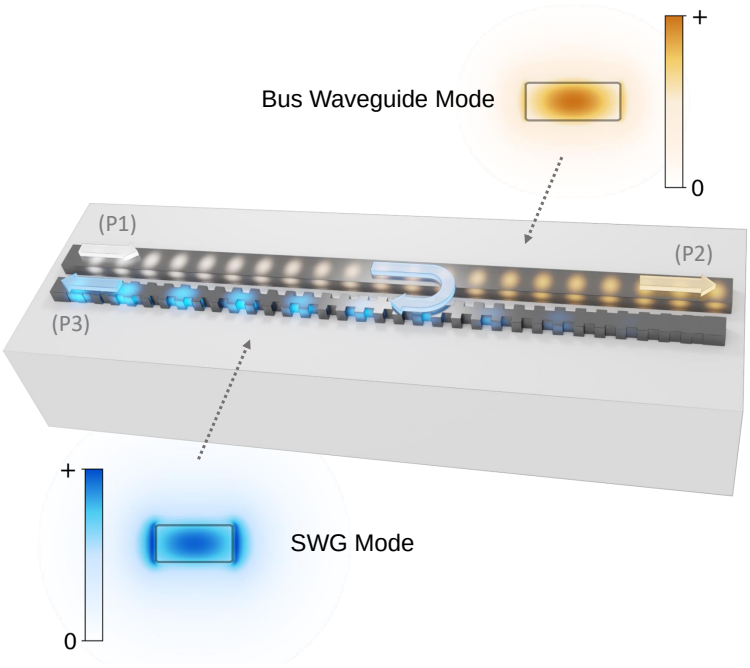

Figure 4.1: Illustration of operation of SWG filter. P1, P2 and P3 refer to the input, through, and drop ports, respectively. The SWG filter is designed such that a select band of frequencies (shown in blue) is dropped into P3 while the remainder of the spectrum passes from P1 to P2. The drop frequency depends on the effective indices of the SWG and bus waveguide modes.

Placing (4.2) in terms of effective index and the dropped wavelength, λ_{drop} , then gives

$$-\frac{n_{SWG}}{\lambda_{drop}} = \frac{n_{wvg}}{\lambda_{drop}} - \frac{1}{\Lambda}, \tag{4.3}$$

where n_{SWG} and n_{wvg} are the effective indices of the SWG mode and waveguide modes at λ_{drop}, respectively. By re-arranging (4.3) to solve for λ_{drop}, we arrive at a convenient expression for the contra-directional coupling condition.

$$\lambda_{drop} = \Lambda\,(n_{wvg} + n_{SWG}) \tag{4.4}$$

At this point, it is important to note that a SWG can enable diffraction between any two available modes that satisfy (4.1) in its proximity. Back-reflections occur in the waveguide at $\lambda = \lambda_{b.r.1}$ and SWG at $\lambda = \lambda_{b.r.2}$, where:

$$\lambda_{b.r.1} = \Lambda(2 \times n_{wvg}) \tag{4.5}$$

$$\lambda_{b.r.2} = \Lambda(2 \times n_{SWG}) \tag{4.6}$$

To space back-reflections away from λ_{drop}, one must design the waveguide and SWG to have a sufficient contrast between n_{SWG} and n_{wvg}. The spacing between the dropped wavelength and back-reflected waves, $\Delta\lambda$, can be roughly estimated by

$$\Delta\lambda \sim \Lambda \times (n_{wvg} - n_{SWG}) \tag{4.7}$$

4.3 Design Constraints and Method

To readily implement a SWG filter in GF's 90 nm technology, we designed devices to respect the minimum feature size (MFS) of $\sim$ 150 nm and function inside the local material stack with a 155 nm thick silicon device layer, buried oxide layer and doped oxide (BPSG) cladding, illustrated in Fig. 4.2(a). We additionally limited our devices to be constructed using photonic elements available in GF's product design kit (PDK). No new proximity effect corrections (PECs) were needed for the lithographic steps required to fabricate the SWG filters because GF has used SWG waveguides for spot-size conversion [113]. The SWG filter configuration used here (Fig. 4.2(b)) is similar to designs previously reported to exhibit good performance metrics in the C-band [97].

A bus waveguide width of 420 nm was chosen to attain a balance between having high effective index and evanescent field extent sufficient for coupling. The designed widths of the periodic high index "rib" regions and low index "core" regions of the SWG, indicated in Fig. 4.2(b), and the filling fraction of the rib section (FF) were selected to be $w_{rib} = 350$ nm, $w_{core} = 150$ nm, and FF $= 50\%$ to ensure sufficient index contrast in the effective indices of the SWG and bus waveguide. The effective index of the SWG mode can be expressed as

$$n_{swg} = \sqrt{FF \times n_{rib}^2 + (1 - FF) \times n_{core}^2}, \tag{4.8}$$

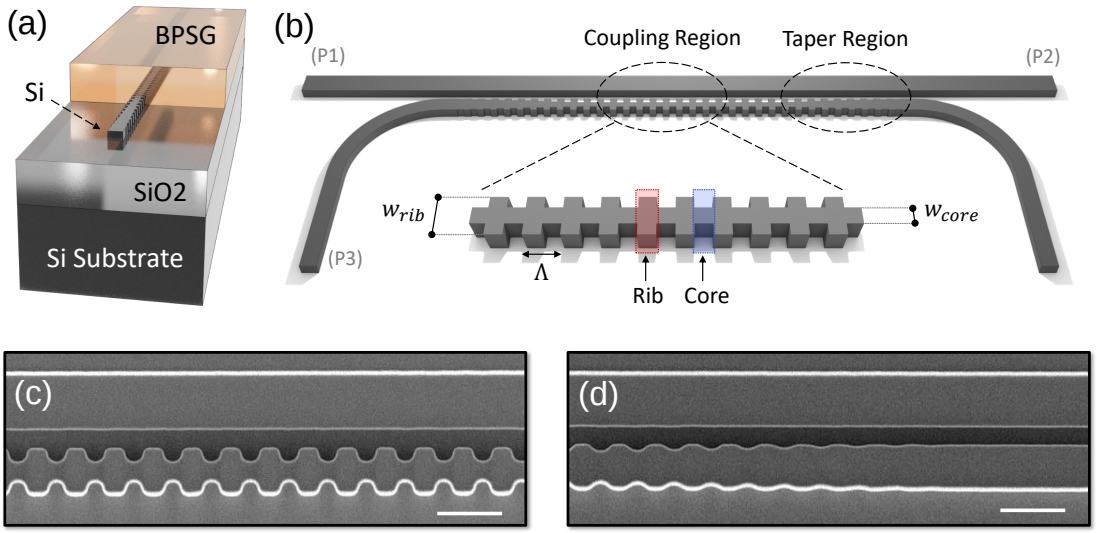

Figure 4.2: (a) The material stack used for the SWG filter. (b) Schematic of the full device and port routing with P1, P2 and P3 representing the input, through and output ports, respectively. SEM images of the coupling section and taper region circled in (b) are shown in (c) and (d), respectively. The SEM images clearly show that photolithography can be used to achieve the subwavelength features in the grating. The white scale bars in (c) and (d) are 500 nm long.

where n_{rib} is the effective index of the rib section and n_{core} is the effective index of the core section [97]. Effective indices were calculated in Lumerical MODE Solutions using the cross sections of the rib and core segments and computing the fundamental TE eigenmode for each. The SWG mode in Fig. 4.1 was approximated using (4.8) and the rib geometry. Because the bus waveguide was designed to have a higher effective index, we designed the SWG to have a low enough effective index to place reflection-bands outside of the measurement window while still supporting a guided mode. After the calculation of n_{wvg} and n_{SWG}, we chose $\Lambda = 330$ nm to filter light in the O-band while respecting the usable MFS. Lumerical FDTD was used to simulate and fine-tune devices. A small taper region (indicated in Fig. 4.2(b)) reduces reflections at the interface of the SWG and the output waveguide. A coupling gap of 160 nm between the waveguide and SWG was chosen. Altering the coupling gap size enables tuning of the drop channel width [97].

4.4 Experimental Results

Filter designs were fabricated in GF's 300 mm foundry in Fishkill, NY (Fab 10). The overall filter footprint was $\sim 0.002\text{mm}^2$. Scanning electron microscope (SEM) images of the SWG coupling and taper regions, indicated in Fig. 4.2(b) are shown in Fig. 4.2(c) and (d), respectively. With the PEC implemented in the 90 nm photonics technology, the MFS necessary for the SWG filter ($\sim$ 150 nm) is obtained with photolithography.

After fabrication, devices were characterized at GF's modeling lab in Burlington, VT (Fab 9). As many photonic devices utilize heaters for active tuning, we tested not only the wavelength response of the filter, but also the dependence on filter location and shape with respect to wafer temperature. The ports used in the experiment are indicated in Fig. 4.1 and Fig. 4.2(b): (P1) is the input port, (P2) is the through port and (P3) is the drop port used for results in Fig. 4.3.

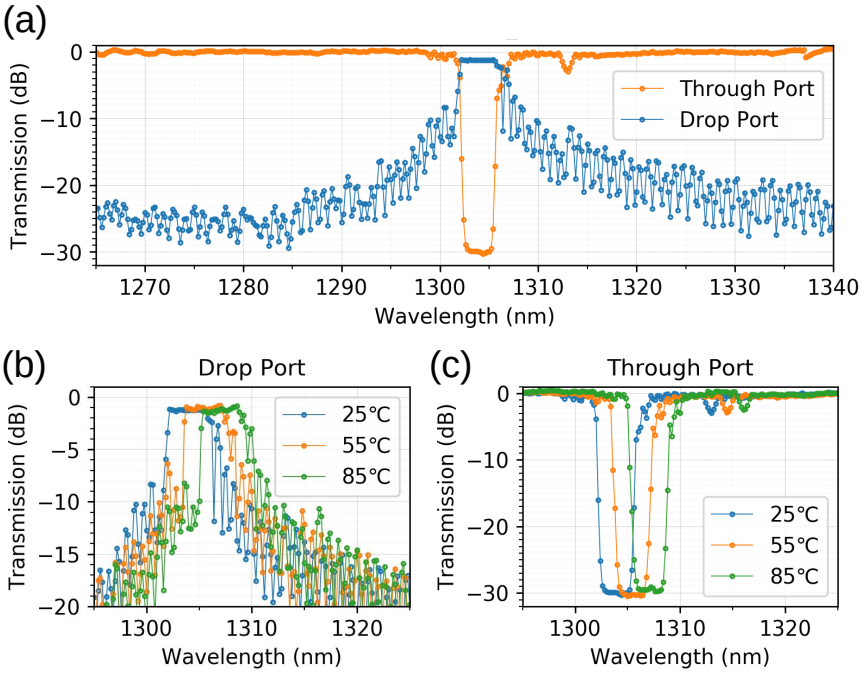

Figure 4.3: (a) Transmission spectra of through and drop ports of fabricated device. Thermal response of the (b) drop port and (c) through port. The data clearly shows shape preservation during thermal tuning and a maintained low loss of $\sim$ 1.2 dB in the drop port.

The transmission spectra for the through and drop ports of a typical device are shown in Fig. 4.3(a), demonstrating an extinction ratio in the through port of $\sim$ 30 dB for the dropped channel, an

insertion loss of $\sim$ 1.2 dB of the channel in the drop port and a 3 dB channel width of $\sim$ 5 nm with a flat-top response. The flat-top characteristic of this platform is due to a distribution of power drop rates centered around the drop wavelength specified by (4) and a sufficiently long coupling region to saturate this response in the total dropped power. We note that there is minor device variability across the wafer but these results represent typical device performance.

The thermal response of the drop port and through port are shown in Fig. 4.3(b,c), respectively. The channel center red-shifts by $\sim$ 4 nm as the wafer chuck temperature increases from 25°C to 85°C. As this temperature was monitored on the wafer chuck, it is possible the local device temperature is lower than the chuck set-point, suggesting that integrated heaters could match or exceed the thermal tuning capabilities reported in Fig 4.3(b,c).

4.5 Discussion of Results

The SWG filter device realizes low loss (-1.2 dB) in the drop channel and high extinction ratio (-30 dB) in the through port with no increase in loss in the through port compared to a reference waveguide. These results suggest the SWG filter platform could enable a modular design where channels could be independently added, adjusted or removed from a WDM device. The compact footprint of $\sim 0.002\text{mm}^2$ for the single filter could enable WDM MUX and DEMUX devices with extremely low footprint compared to interferometric platforms.

As the drop position solely depends on Λ, n_{SWG} and n_{wvg}, the position can be shifted with a single heat source without shape distortion. While many interferometric filters require tuning of all channels simultaneously via multiple heaters, the results here suggest SWG filters require only a single heat source to tune each channel independently, with the tradeoff being that heaters can only red-shift the drop port.

While the filter shown in this work demonstrates desirable performance metrics, there are design modifications that could improve performance. The proximity of the two straight waveguide segments near the SWG taper (Fig. 4.2(d)) results in a small reflection peak at $\sim$ 1313 nm in the through port, as shown in Fig. 4.3(a). Additionally, the abrupt coupling of power to the SWG re-

sults in side-band fringes around the drop channel. Prior work reported that the side-band fringes can be reduced significantly with gradual coupling, which can be accomplished by replacing the straight bus waveguide with multiple S-bends [17]. The switch to S-bends could also eliminate coupling between the straight waveguide sections by placing them farther away, removing the reflection peak at $\sim$ 1313 nm.

4.6 Conclusion

As datacenters have moved to optical interconnects, the cost of increasing bandwidth is closely tied to the cost of optical transceivers accommodating WDM. To mitigate this cost and address the scale of datacenters, integrated photonic solutions are needed to enable WDM in optical interconnects. Toward this goal, we demonstrate the manufacturability and performance of SWG filters in GF's 90 nm monolithic photonics technology. The device, which was designed using GF's PDK and manufactured at Fab 10, demonstrates low channel loss of -1.2 dB, high extinction ratio of -30 dB, 3 dB channel width of $\sim$ 5 nm, a small footprint of $\sim 0.002\text{mm}^2$ and a MFS of $\sim$ 150 nm. Single-source thermal tuning of $\sim$ 4 nm was achieved in the drop channel without shape distortion. This work demonstrates the first O-band SWG filter in a monolithic technology and continues the push towards translating high-performance photonics from academia to industry.

Chapter 5

Conclusions and Future Directions

In the investigation of photonic crystals, this work has outlined a means of efficiently coupling photonic crystal nanobeam cavities via state-space overlap (Chap. 2), developed a rigorous method to identify optical modes via modal fingerprinting (Chap. 3) and engineered a subset of photonic crystal nanobeams, named subwavelength gratings, for filtering applications in a monolithic photonics technology (Chap. 4). By defining explicit methodologies for highly efficient resonator coupling and modal analysis, we hope to improve the performance and reliability of future works leveraging photonic crystal properties for optical applications. By demonstrating the manufacturability of subwavelength-grating filters in a monolithic technology, we hope to continue pushing the adoption of advanced photonic platforms from academia into industry.

While this work has helped to answer some questions on the feasibility and applicability of photonic crystals for nanophotonic applications, it has also raised other questions regarding the general implications of this work and new possibilities for future projects. Two suggestions of paths for continuing this line of work are briefly outlined in the following sections.

5.0.1 Inverse Design of Scattering and Emission

Using the methodology in Chap. 3, it is possible to predict the far-field scattering of any given photonic device mode. Given this powerful tool and through leveraging inverse design optimization, it would be almost certainly possible to design photonic devices for specific scattering shapes and optical linewidths. This would be incredibly useful for potential beam-steering applications, sensing or lasing/light emission on a chip. To realize this, one would simply need to pick their favorite inverse design method (adjoint method, particle swarm, Monte Carlo, genetic algorithm, deep/machine learning etc.) and optimize based on an overlap integral with the desired response in k-space and frequency space. For active devices, one could use phase-change or non-linear ma-

terials to construct a compact photonic device in ”pixel-like” segments and use inverse design to define electrical biasing configurations of the devices for specific scattering behaviour. These pixels could be unit cells of a photonic crystal, scattering elements in a metamaterial or pieces of any other nanophotonic device. The concept of this work is fairly general and thus could be conducted in a wide range of material systems.

5.0.2 Further Translation of Advanced Photonic Platforms to Industry

With the success of our collaboration with GlobalFoundries (GF) in Chap. 4, it could be of great benefit to both academia and industry to explore the implementation of many advanced photonic devices in a monolithic technology for difficult-to-realize functionality, including high-tolerance photonic elements, optical isolators, compact modulators and commercial optical sensors (including LiDAR). While many such possibilities of continuing this area of work could be quite ambitious, projects on passive devices could have a large degree of success. As there is a significant focus on tolerance and loss in industry, creating high-tolerance, low loss versions of simple devices, such as a waveguide, waveguide bend, MZI or y-splitter would be invaluable to industry. Designing these devices using an inverse design approach (either for parameterized shapes or topology optimization) would also add novelty and translate a powerful computational tool into the industry setting. Using this CMOS technology for testing thin-film optics, such as multi-layer meta-surfaces using both the silicon and metal layers of the stack could also be quite interesting and novel. Designing optical isolators using edge states in topological photonics could also be incredibly novel and practical for industry.

Appendix A

Methods and Notes to Future Students

The following appendix focuses on experimental methods which supported the research in Chapters 2-4 or adjacent projects in the lab, but did not make it into publication. As this type of section in theses is often utilized by new and incoming graduate students to help with learning new concepts, troubleshooting or reproducing work, I have opted to compose this section with regard to accessibility toward that target audience. I have additionally opted to include snippets of my personal experience which may prove a useful tool in imparting some research intuition at the cost of a non-traditional usage of active voice. It is the hope of this section to fill in some of the gaps in understanding that come with reading papers, starting new experiments or generally conducting research for the first time.

A.1 A Note to Future Students

In my experience conducting graduate research at Vanderbilt University, one of the greatest lessons I have learned is the devil is in the details, and details are always in short supply. During my graduate experience, I struggled countless hours troubleshooting and investigating how to make projects work using the resources and information from papers and previous graduate student theses. For any future graduate student reading this, I want to reassure you, this struggle is not only shared among ALL of your colleagues, but it is REQUIRED to fuel your development as a researcher and problem solver. As with other processes of extreme growth, this will likely be a painful process, but the personal and professional rewards are well worth it. My personal advice is to hang in there, dedicate time for self-care and recovery, and find all the resources you have available to help fuel your growth. While the go-to resources are often books, videos, papers and knowledge bases, do not forget the people you share your time with and that you are not alone in research. Your friends, family, colleagues and advisor are invaluable resources for emotional,

intellectual and professional support along the way. Find the way(s) you prefer learning/recovering and understand what motivates you. Use this information to find resources to propel you forward. The rewards and outcome of a PhD vary greatly from person to person and are strongly determined by the magnitude and strategic allocation of the efforts you put into it.

Perhaps the biggest frustration I have as a graduating researcher is that after struggling so hard to gain the competency to conduct research, I realize it is impossible to fully transfer that knowledge in a document such as a thesis. While I may be able to provide procedures and steps for executing experiments, subtle yet important research details will inevitably be omitted. This is why, in my opinion, the most important resource I can provide is intuition and direction for your journey in research.

A.2 Appendix Overview

The content of this appendix includes sections on the following elements that enabled the research in this thesis and related projects in the group:

(1) General design methodology for experimental photonic devices

(2) Device fabrication workflow at Oak Ridge National Labs (ORNL)

(3) Procedure for undercutting photonic devices

The intent of this appendix is to be brief, but provide intuition which can translate beyond the scope of current and previous projects in the lab. At the end of the day, you will need to independently troubleshoot and search for details. Toward this end, I highly recommend consulting the expertise of the Weiss group and our collaborators. When unsure of where to reach out, leverage the expertise of your advisor and colleagues to guide your search for information.

As one last word of advice before transitioning into further sections, I implore you to be open to, but skeptical of any information you receive, including any information in this thesis. ALWAYS be sure to check any new information for consistency with your intuition and across multiple external sources. While other researchers often mean well, they are not impervious to mistakes

and providing misleading information. It is my belief you will frequently encounter this on your journey and it is ultimately up to you to vet any new information you choose to act on.

A.3 General Design Methodology for Experimental Photonic Devices

In the Weiss group, much of the research conducted revolves around the design of photonic devices for various applications. The success of these applications and experiments hinges on the integrity and robustness of the device design. A generalized list of design steps applicable to work in this thesis is outlined in Table A.1.

#	Step
1	Device Selection
2	Design Optimization and Simulation
3	GDS Creation and Checking
4	Fabrication and Test
5	Data Collection and Analysis

Table A.1: List of design steps for making photonic devices. Though this list may not comprehensively address all research situations for photonic devices, executing each step in a robust way has played a significant role in the success of every project included in this thesis.

While Table A.1 was constructed based on the limited experience gained in this thesis, I believe it is applicable to a wide range of device work. To outline the importance of this thought process when creating devices for research, I will first go through how this applied to work in Chap. 4 on subwavelength grating (SWG) filters in Sec. A.3.1, and then pose questions in Sec. A.3.2 which could be asked at each step to generally assist in creating robust device work-flows for research and troubleshooting issues.

A.3.1 Application to Work on Subwavelength Grating Filters

As mentioned previously, this section takes a look at the application of Table A.1 to work in Chap. 4, as it is the most compact section in this thesis. *Before reading this section, please read Chap. 4 to provide context.* The idea of using SWG devices as filters in a monolithic technology

came from the research question posed to me by my manager at GLOBALFOUNDRIES (GF) during an internship. The question posed here was *"Can you make a filter out of a photonic crystal which is competitive with the filters we currently use?"*. Based on this research question we can see our first step in the design process:

(1: Device Selection) In this case, device selection is limited to photonic crystal devices by the research question asked. After limiting my search of filtering devices down to photonic crystals, I simply had to limit my consideration of devices further based on how they performed in the literature relative to the cascaded Mach-Zehnder interferometer (MZI) filters used by GF [106]. The only devices I found in the literature to do this in a way that could be quickly designed and fabricated were the SWG filters discussed in Chap. 4. The specific metrics of value to GF used in this selection were channel width, channel shape and insertion loss.

Once a device has been selected for study, it needs to be properly designed/optimized in order to have good enough results for publication. It is also necessary to verify the design works in simulation before fabricating the device. This can prevent redesigns and multiple fabrication runs which can expend a significant or sometimes unallowable amount of time. In the case of this project, getting the design wrong would have meant no publishable results after 6+ months of work and potentially having GF throttle back their support for the project or effectively ending their support. To emphasize the importance of gaining competence in simulation and optimization, the SWG filter designs had to be optimized in a span of $\sim$ 4 days near the beginning of the internship (for reference, the first photonic crystal simulations I ran in graduate school took multiple months of iteration to match results in literature). As some icing on the cake, I had the remaining 4-5 months in the internship before device results came back to wonder if I missed anything. For this project, step 2 was as follows:

(2: Design Optimization and Simulation) The designs were optimized for O-band performance

using a combination of equations in Chap. 4, which were compiled from the available literature, and a significant number of manually tweaked (in a script) 3D Lumerical FDTD simulations of full devices in GF's material stack. Many of the tweaks were driven by intuition on what factors could reduce loss and increase bandwidth given design limitations imposed by the team at GF to protect the foundry. To build this intuition, I drew from my general nanophotonics background and spent dozens of hours adjusting various parameters and simulating to confirm or challenge this intuition. As a result, the main way I adjusted the design to reduce loss was by playing with the taper length to the drop port waveguide. The main ways I increased bandwidth were by making the coupling gap as short as allowed and delocalizing the fields of the SWG and bus waveguide as much as possible while maintaining the index contrast needed to prevent back-reflections from getting too close to the drop channel.

After the important, albeit painful, process of optimizing the designs with checking and rechecking simulations, designs must be translated to a GDS (Graphic Data Stream) file for fabrication. This is the generally used design format for lithographic techniques including electron beam lithography (EBL) and photolithography. To emphasize the importance of gaining competency in scripting/checking GDS files, designs for this project were done on a time crunch of 1 day (my first photonic crystal GDS file designs I did without scripting in graduate school took $\sim$1 month). To do this, step 3 was as follows:

(3: GDS Creation and Checking) The GDS files for the SWG filters were designed using Cadence Virtuoso, as it was the standard design tool at GF. Much of the design creation and checking was done manually in this case, as I was not proficient at scripting in Cadence at the time. By looking through the filters, confirming design parameters and running the standard design rule check (DRC) program used by GF to check layouts, I was able to catch errors made in the design and quickly submit the layout. If there was more time for checking the layouts, I would have wanted to import the device portions of these layouts into Lumerical FDTD to simulate the GDS file directly,

as this provides an even more robust method of checking errors in the layout file.

After submitting the GDS file to the fabrication team, most of the difficult parts of the project were actually done. For the SWG filter work, is a perfect example of where having exceptional, motivated and dependable collaborators made all the difference. In general, however, fabrication and testing should be completed with several steps of troubleshooting steps in between, including imaging the devices to check for proper fabrication of performance-critical features and characterizing the test setup to ensure proper polarization/alignment. With the the help of the team at GF, step 4 was as follows:

(4: Fabrication and Test) Fabrication of the SWG devices was handled entirely by GF over the course of ~ 4 months using their monolithic photonics technology exclusive to GF. After first hardware was available, a wafer was pulled and scrapped by the GF team for characterization in the modeling lab at GF's Fab 9 in Burlington, VT. At that time, test engineers there worked with me to help me write up a test plan for characterizing the devices over multiple wavelengths and wafer temperatures. Once this test plan was submitted, the characterization team took over on testing and reached out when some brief troubleshooting and test plan adjustments were needed.

After fabrication and test plan submission, devices were tested and data collected by the GF modeling team. While this data was already organized in a compact, well organized file for analysis, it can often be the case that file organization or mislabeling can impede research results. It is ESSENTIAL to the success of your projects to establish a file organization system early which can scale to maintain and organize 4+ years of data for your PhD. Additionally, mistakes in analysis can result in incorrect assumptions or conclusions on device performance. This can create mistrust among your immediate colleagues or even whole paper rejections (this unfortunately happened for my first paper, which is now revised in Chap. 2). These setbacks cause an immense amount of frustration and can prolong your PhD. To avoid these issues, step 5 was as follows:

(5: Data Collection and Analysis) Shortly after the submission of the test plan and correcting some initial test errors, results were provided by the test team in a compact .csv file which could easily be read. I chose to analyze and plot this data using the Pandas package in Python, as the data was easily convertable to dataframes for use. The data from the through ports was then fitted at specified intervals around the drop channel in python and used to subtract the losses due to the grating coupler response curve. This way a clean loss measurement could be extracted for the device. These results are what is presented in the SWG filter work in Chap. 4.

A.3.2 General Questions to Photonic Device Research

While the example in Sec. A.3.1 demonstrates specifically how the design rules in Table A.1 applied to the problem in Chap. 4, there are some questions and considerations which can assist in making the photonic device design workflow more robust in a more general sense. When designing photonic devices, I recommend to consider the following questions for each step:

1: Device Selection

- What is my research question?
- What device design is best for addressing my research question?
- Is this device design novel?
- What is required from this device to have publishable results?
- What is required to implement and characterize this device?

2: Design Optimization and Simulation

- What is the best way to optimize this device?
- Does this optimization add novelty?

- What is the best simulation software for this task?
- How can I reduce simulation time?
- How do I check that the simulation results are real?
- What could go wrong in the optimization or simulation?
- How would I troubleshoot optimization or simulation errors?

3: GDS Creation and Checking

- What is the best software for me to use to make GDS files?
- Is scripting enabled in my GDS design software?
- How can I design GDS files for quick adjustments and redesigns?
- How can I reduce mistakes in making GDS files?
- What is the best way for me to check my GDS files?
- What could go wrong in GDS creation?
- How would I troubleshoot problems in GDS creation?

4: Fabrication and Test

- How much time is needed to develop new fabrication processes or testing setups?
- Does the process or testing add novelty?
- How can I improve process reliability and repeatability?
- What can go wrong in fabrication or testing?
- How would I troubleshoot problems in fabrication and testing?

5: Data Collection and Analysis

- Does my data organization method scale over time?
- What is the best file format for organizing data?
- What is the best software for analyzing data?
- Do my data collection or analysis methods add novelty?
- What could go wrong in data collection and analysis?
- How would I troubleshoot problems in data collection and analysis?

Going through these questions, it is important to keep in mind, it is not the expectation to know the answer to all these points going into a project. In fact, the more novel the work, the less likely you will be to answer these questions initially. In my opinion, the true test of a researcher lies in the journey to search for these answers and build intuition which can compound and assist in future projects. As mentioned previously, I recommend probing your colleagues and advisor in addition to independently researching literature and knowledge bases to search for these answers. I also hope that the example research problem in Sec. A.3.1 can assist or even act as an exercise in addressing these questions as one progresses through research.

A.4 Device Fabrication at ORNL

Much of the device fabrication in the Weiss group is completed at the Center for Nanophase Technology (CNMS) at Oak Ridge National Labs (ORNL). The support from our collaborators at Oak Ridge, the experience of their staff, and the maturity of their fabrication processes has made fabrication at Oak Ridge an ESSENTIAL part our group's success in research. Before delving into our processing steps at CNMS, I feel it is important to acknowledge the members of the CNMS team who have helped our group immensely and will likely be excellent resources for future graduate students to reach out to for research support. For troubleshooting and support, please consider reaching out to the people in Table A.2

CNMS Collaborator	Email (as listed on website)
Bernadeta Srijanto	srijantobr@ornl.gov
Dale Hensley	hensleydk@ornl.gov
Dayrl Briggs	briggsdp1@ornl.gov
Ivan Kravchenko	kravchenkoii@ornl.gov
Kevin Lester	lesterkc@ornl.gov
Scott Retterer	rettererst@ornl.gov

Table A.2: ORNL collaborators who have been excellent resources during the research in this thesis.

A.4.1 A Note for Developing New Processes

In my opinion, process development is one of the most tedious and time-consuming endeavors that a graduate student can undertake. Part of the reason CNMS has been a cornerstone in our group's success is due to their assistance in process development. My personal advice is to avoid process overhauls in favor of successive, minor process adjustments which can be troubleshot more easily. If an overhaul or major change is needed, ensure you have the CNMS team onboard for assisting in process development. I can not reiterate enough that they will be one of your greatest resources when it comes to fabrication.

A.4.2 Overview of Fabrication Workflow at CNMS

#	Process Step	Description
1	Chip Cleaving	Cleave chips to fit in EBL tool
2	Surface Preparation	Ensure chips are clean and hydrophilic
3	Resist Coating	Spin coat resist using standard recipe
4	GDS Tweaking/Import	Adjust/bias GDS files and convert for EBL
5	Exposure Configuration	Arrange patterns on chips and set doseage parameters
6	Pattern Exposure	Load chips, calibrate EBL and expose patterns
7	Pattern Development	Develop resist using standard procedure for resist
8	Etching and Resist Strip	Use standard recipes to etch silicon and strip resist
9	Imaging	Note abnormalities/changes to critical dimensions
10	Iterate and Adjust	Bias/adjust designs and process steps based on imaging

Table A.3: Weiss group fabrication workflow at CNMS

The Weiss group's fabrication workflow for creating silicon photonic devices is outlined in Table A.3. The evolution of physical changes to the chip per the fabrication workflow in Table A.3 is illustrated in Fig. A.1. It can be seen in Fig. A.1 that the physical changes to the chip are only a direct result of a subset of the steps in Table A.3. The remainder of the steps support the preparation of the chip and layouts and assist in troubleshooting and design iteration. It is CRUCIAL to note that while going through this process workflow, always record details of what procedures are being run in your cleanroom notebook. Additionally, scan your notebook daily (using a phone camera) for your electronic records. You generally will not remove a cleanroom notebook from the CNMS cleanroom unless you expect to permanently retire it.

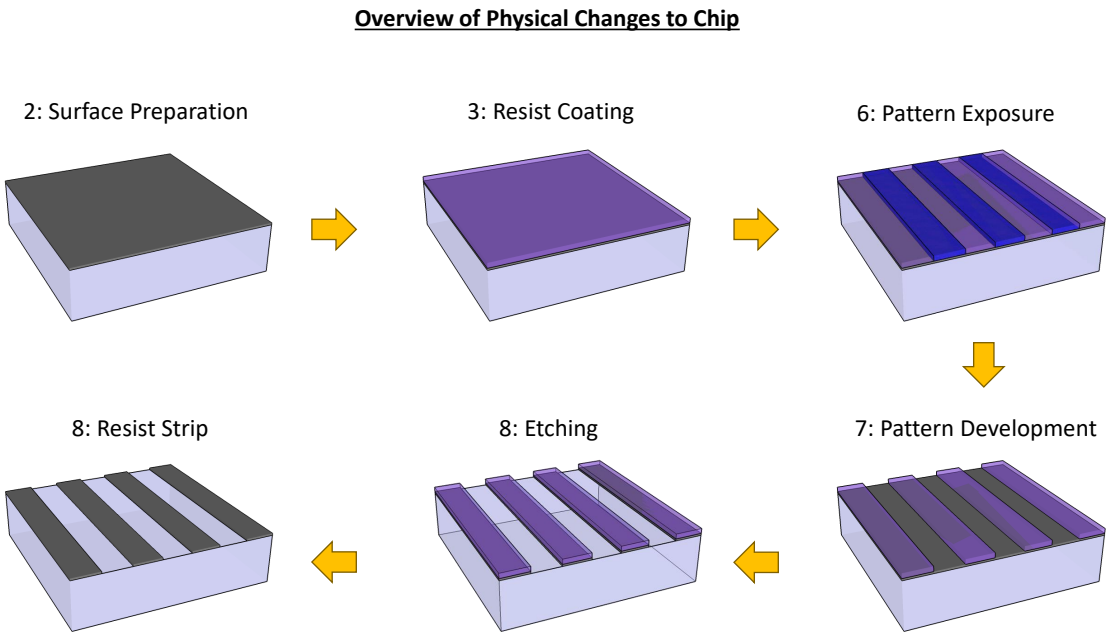

Figure A.1: Overview of physical changes to chip during fabrication process at CNMS. The chip shown is a thin silicon device layer (grey) on glass (light blue). Electron beam resist is shown in purple with exposed resist represented in dark blue.

A.4.3 Description of Steps in Workflow at CNMS

It is the intent of this section to provide a brief description of each step in the fabrication process to provide intuition of how the process is structured and steps are tied together. The list of steps are as follows:

(1: Chip Cleaving) Chips for fabricating devices are cleaved from a silicon on insulator (SOI) wafer stored at CNMS. The purpose of cleaving chips is to utilize SOI as efficiently as possible for device fabrication, as SOI for photonics is significantly more expensive than standard silicon wafers. The EBL chuck used by the Weiss group at CNMS accepts specific chip sizes, requiring chips be cleaved to specific dimensions for optimal space utilization. The chip slot dimensions for this chuck and optimal chip cleaving dimensions are illustrated in Fig. A.2.

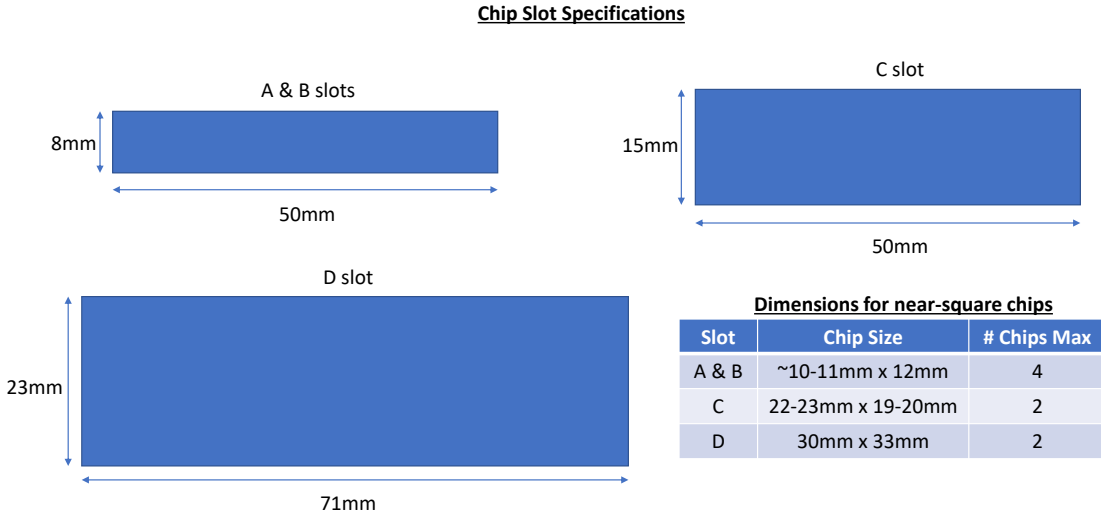

Slot	Chip Size	# Chips Max
A & B	~10-11mm x 12mm	4
C	22-23mm x 19-20mm	2
D	30mm x 33mm	2

Figure A.2: Slot dimensions for EBL chuck at CNMS. These slots act as the window for writing patterns on loaded chips. The chips are clamped from behind these slots within a larger holding area. This setup requires chips which are larger than the vertical slot dimension to secure chips. The dimensions of cleaved chips used in these chucks and number of chips acceptable in these chucks are listed here.

Chips can be cleaved manually via a diamond scribe or via the dicing saw tool in the cleanroom. In both cases, approximately square chips are typically used, as they work better for uniform spin-coating of resist while providing slightly more write area along their larger dimension. I recommend cleaving chips manually to allow more customization of chip sizes extracted from a wafer and to reduce re-deposition of silicon dust on the chip, which can scratch the surface and be difficult to remove. The dicing saw limits cleaving on a chip to uniform chip size and requires an

adhesive backing, which can make chip removal difficult if left attached to the wafer too long. Removal of closely packed chips from this adhesive can result in chip edges rubbing, which can deposit significant amounts of silicon dust on the surface of the chips. This being said, the dicing saw is a valuable tool and there are clever ways to get around these issues, but this requires further exploration. Please use Table A.2 to consult the owner of the dicing saw tool (currently Kevin Lester) to learn more about its capabilities.

(2: Surface Preparation) The surface of SOI chips needs to be properly prepared to ensure devices resolve clearly during lithography. This requires no contaminants or particulates being present on the sample and that the surface is hydrophilic. The presence of contaminants or particulates on the chip surface will degrade device performance and fabrication reliability. A hydrophilic surface enables adequate resist adhesion, which is important for properly resolving small features in the EBL. To clean particulates, I recommend blowing the sample with nitrogen (available under most hoods in the cleanroom). If this does not adequately remove particles, an IPA or DI water rinse followed by a nitrogen blow dry can help mechanically remove stubborn particles. To make the surface hydrophilic, I recommend using the TePla dedicated O_2 resist stripper/plasma cleaner. The O_2 resist stripper/plasma cleaner can also be used for clearing the chip from a bad (non-uniform or streaking) coat of resist. The O_2 plasma clean removes residual organics present on the surface and creates a thin oxide ($<$ 1nm) on the surface of the silicon, leaving the chip in pristine condition for spin-coating resist. Always visually inspect chips after surface preparation to check for irregularities or residual organics and use cleaning times based on the recommendations of CNMS staff and Weiss group members.

(3: Resist Coating) EBL resist is used for creating the patterns for photonic devices on the chip. The standard resist used by the Weiss lab is ZEP 520A, a positive resist (exposed areas of resist are **removed** in development). This resist is coated on an SOI chip using the following parameters:

- Center the chip on the spin-coater chuck

- Coat chip fully with ZEP 520A resist using plastic pipette
- Spin at 6k rpm for 45 sec.
- Bake at 180°C for 2 minutes
- Let chip cool on metal surface for 1 minute before storing

After coating, inspect the chip to ensure the resist has coated the sample uniformly and there are no significant irregularities or streaks on the sample, as this can affect the quality of pattern exposure. Sample handling and resist coating in this tool are described in greater detail via the training given by staff at CNMS. Again, please use the recommendations of CNMS staff and Weiss group members when conducting this step of fabrication.

(4: GDS Tweaking/Import) GDS patterns are used to define the photonic devices to be made on SOI chips. Before importing these designs into the file format used by the EBL, it is important to spot-check the GDS files for accuracy and make adjustments based on previous pattern writes and/or imaging results. Be sure to record notes on file naming and design specifications in your cleanroom notebook, as it can be the case you will want to reuse the designs that have been imported in subsequent fabrication runs at CNMS.

While importing designs into the EBL write format, pay careful attention to the details of the exported design, including position of write fields, layer definitions for dosing, exposure path and shot packing. Many of these details are well understood by CNMS staff including Scott Retterer and Ivan Kravchenko as well as Weiss group members. During the work on this thesis, I payed special attention to shot packing to improve the reproducibility of designs and resolution of small features. To improve shot packing of designs, I recommend only including low-poly elements in your GDS files with LRFT (large rectangle fine trapezoid) fracturing and using exposure dose to round out these features. An example of the shot packing difference between high-poly and low-poly features is shown in Fig. A.3. It can clearly be seen that by using low-poly shapes, we can

increase the consistency and overall density of shot-packing which leads to better consistency in pattern exposure and resolution of small features.

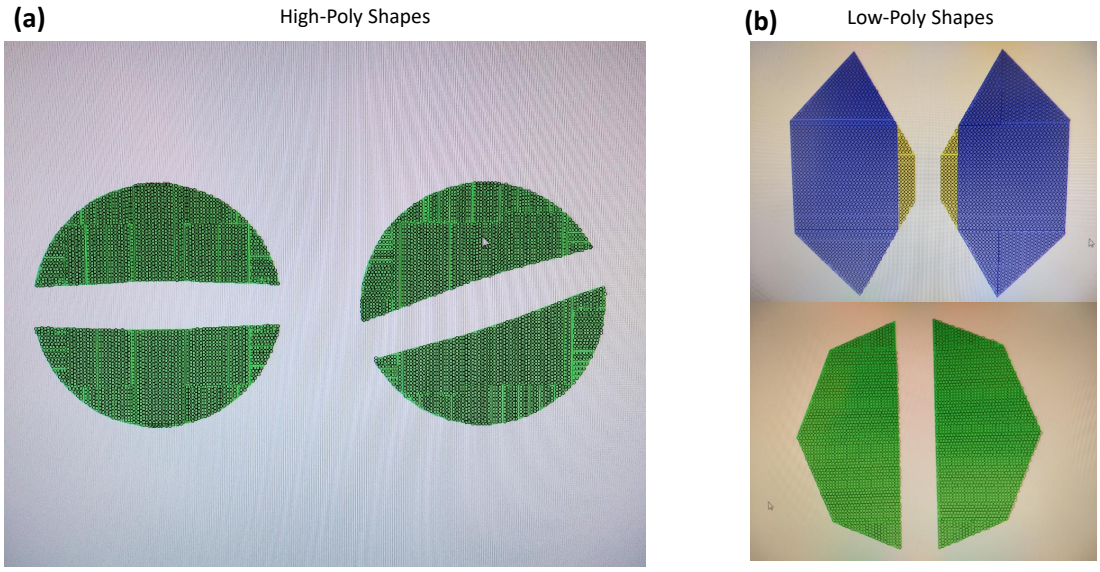

Figure A.3: Difference in shot packing between high-poly shapes (a) and low-poly shapes (b). The high-poly shapes in (a) show more gaps between shots (black circles) and less consistent packing across the shapes. Low-poly shapes in general show higher shot packing consistency.

(5: Exposure Configuration) Exposure configuration consists of arranging how patterns will be exposed on the chips loaded into the EBL and what electron beam doses will be used for exposure. Advanced features also include virtual chip markers for height map corrections (this calibrates for height on the chip and improves stitching errors between write fields) and local alignment for secondary lithography (this is quite difficult, please ask Ivan Kravchenko for support if attempting this). The steps for configuring exposure on ORNL's JOEL JBX-9300FS EBL include:

- Load chips into chuck and use a ruler to measure/record chip positions/sizes
- Use chip positions/sizes to create a plan of how to set up patterns on each chip
- Specify pattern placement and dosage in chip design file
- Include virtual chip markers if desired in chip design file
- Compile chip design files for scheduling run and fix errors

- Check chip layout from compiled file against planned layout and chip borders
- Estimate pattern write time and be sure it is below the available run time

When laying out patterns on a chip, be sure to consider:

- Where the chip edges are
- How much space you need to cleave patterns out of the chip for characterization
- How many exposure doses you would like to sweep
- How much time you have for writing
- If there are different thicknesses of SOI chips loaded

Exposure configuration can be a bit of a stressful and time-consuming step initially. With proper planning for this step and gaining experience in scripting up the configuration files, it will likely become second nature. Many of the details of this process will be outlined in formal training through CNMS and working with senior graduate students in the Weiss group. Be patient in this learning process and make sure you get plenty of experience completing this step before senior graduate students leave.

(6: Pattern Exposure) Pattern exposure is how the EBL directly exposes the resist (via an electron beam) to transfer the patterns defined in your GDS files to the resist on the chip surface. This step also involves the calibration of the EBL for this process in addition to sending the command to execute a write. While this part of the process may initially look difficult, it is one of the easier ones to execute. This is largely due to the staff at CNMS having a written, step-by-step procedure for loading the sample chuck, calibrating the EBL and beginning exposure. Even after my many visits to CNMS, I still use this procedure every time and 99.9% of the time things turn out perfectly. Some notes for executing this procedure include:

- Begin the sample load process as soon as possible, it takes $\sim$ 20 min.

- Always refer to the procedure and execute each step in order
- If there is any hiccup or error in the process, contact CNMS staff. DO NOT attempt to fix anything odd on your own

Once the pattern exposure has been initiated, there will be a little cartoon of the exposure being executed. This will let you know the exposure has executed successfully and you're good to leave the EBL alone until the run is done.

(7: Pattern Development) Pattern development uses a chemical reaction between the exposed resist and a developer to reveal the pattern that was printed on the chip in the EBL. Once the EBL run has been completed, check the final screen for any error messages and contact CNMS staff if there are any errors. If there are no errors, unload the sample chuck and set up for the development process while it is unloading. For development, you need:

- A face shield
- Two tupperwares, one small one for developer and one large one for rinsing
- Xylenes developer
- An IPA squirt bottle
- Chemical labels by each tupperware including your name and the date

When running this process, be sure to log chemical waste and afterwards be sure to rinse all tupperware multiple times with DI water and store for drying. After your chips are unloaded, you may execute the development process as follows:

- Develop chip in Xylenes bath (small tupperware) for 30 sec. w/ gentle agitation
- Rinse chip thoroughly w/ IPA spray bottle over large tupperware
- Gently blow dry chip with nitrogen line under hood

- Visually inspect sample for pattern exposure
- Store sample after completely dry

Details and suggestions on handling chips during this development can be obtained from senior graduate students. Unfortunately, manual development is a bit of an art, so you may need to play around with how you handle and agitate chips to get the best results.

(8: Etching and Resist Strip) Etching involves transferring the pattern from the resist mask to the silicon via a plasma which removes silicon in regions not covered by resist. A resist strip is then used after this etch to remove the resist, leaving a clean SOI chip with your photonic devices etched into it. The steps for etching and resist stripping in the Oxford PlasmaLab System 100 at CNMS include:

- Run a pre-clean in the etching tool to clean the chamber
- Place chips on a carrier wafer with Krytox thermal adhesive
- Load the carrier wafer into the etch chamber
- Edit any necessary parameters of the etch and run
- Visually check chips after etch and reload for resist strip
- Visually check chips after strip and unload
- Clean carrier wafer and chip backs w/ IPA to remove Krytox
- Repeat as needed for remainder of chips
- Run a post-clean in the etching tool to clean the chamber

While there is a great amount of detail lost in the steps in this brief overview, I will attempt to outline some important points when going through and etch/strip. It is important to have a clean

chamber for any etch process to promote repeatability. As the etch process depends partly on the temperature of the material being etched, it is important to use a thermal adhesive, such as Krytox, to thermally connect the chip to the carrier wafer. When applying Krytox, it is important to not use too much or too little. When in doubt on how much Krytox to use, please consult senior lab members or the CNMS staff. Before executing the etch process (named "OPT Si Waveguide 2" at CNMS) our lab changes the strike power (1800 used by our lab) and etch time (2 min. for 220nm and 270nm SOI). Be sure these parameters are edited properly before beginning the etch. After the etch, visually inspect the chip for changes (just in case something went horribly wrong) and begin the resist strip. Historically, we have used a 10 min. run of the "DESCUM" recipe at CNMS which is a low powered O_2 clean, but it is also feasible to use a 5 min. run of the "ICP Chamber Clean 20C " etch. The chamber clean etch is a higher powered O_2 clean. Resist can also be stripped in the TePla dedicated resist stripping tool mentioned in **(2: Surface Preparation)**. Be sure to visually inspect chips after stripping to be sure all resist was removed and the patterns have been etched. After removing the samples from the Oxford, remove the chips from the carrier wafer and clean off the Krytox from the chip backs and carrier wafer using IPA. After running the full etch and strip process for all chips, run a post-clean on the chamber to prepare it for other users.

(9: Imaging) While visual inspection along the whole fabrication process is a good way to troubleshoot catastrophic issues, it is necessary to more closely inspect the devices using scanning electron microscopy (SEM) in CNMS's Merlin SEM. This tool is the same model as the SEM used by VINSE at Vanderbilt. While imaging at CNMS, be sure to check:

- If the SEM scale bars are accurate (no joke this has been a big issue at CNMS)
- If critical features in the photonic devices are close enough to desired result
- Which doses used produce the best results

To check if the scale bars are accurate, measure a periodic structure on the sample and note the difference between the scale bar measurement and the target period. The period in the JOEL is

generally quite good and should be relied upon in favor of the Merlin SEM's scale bars. Use this difference to normalize any scale bar measurements to extract more accurate dimensions. Note offsets in critical dimensions for use in biasing future designs and record which doses produced the cleanest features.

(10: Iterate and Adjust) After collecting information on how patterns turned out during imaging, it is important to iterate through the process workflow and adjust design files and potentially process steps to improve the quality of devices. For much of the work in this thesis, most of the adjustments needed were biasing dimensions in the GDS files for import and the dosages used in the EBL writing process. To gather information on how to do this for your specific project and devices, please leverage the experience of senior Weiss group members and CNMS staff.

A.5 Procedure for Undercutting Photonic Devices

Many photonic devices achieve higher performance metrics when their cladding and substrate materials have equivalent refractive indexes and when the surrounding refractive index is low. These conditions work to improve the symmetry of the mode and help improve confinement by increasing the index contrast between the photonic device and surrounding environment. For photonic devices in SOI, this can be done by suspending the silicon device via an undercut of the buried oxide layer.

The process of undercutting silicon photonic devices is often done via wet etching using a buffered hydrofluoric acid (HF) solution (often referred to as buffered oxide etchant (BOE)). From my experience, this process can be incredibly frustrating and requires a significant amount of care and finesse to execute with some degree of repeatability. During my time conducting research at Vanderbilt, I worked on developing a repeatable undercut process for delicate photonic structures, with some limited success. The following section will outline and discuss the process I believe to be capable of repeatable undercutting and present some intuition of how to troubleshoot and further optimize the process, should it be necessary for future devices. It should be noted that I

explicitly avoided having my research rely on an undercut, as it requires a significant amount of attention and can dramatically reduces the reliability of your overall workflow. If possible, I advise to avoid undercutting devices unless they are already quite mechanically robust.

Process Step	#	Procedure List
Surface Preparation	1	Acetone/IPA clean to remove particulates
	2	10 min. O_2 plasma clean in dedicated O_2 plasma cleaner
	3	5 min. heating on 100°C hotplate for surface dehydration
Spin/Bake	4	After sample at room temp., use S1813 resist
	5	4000 rpm, 60 sec.
	6	2 min bake at 100°C
Pattern	7	Local alignment in Heidelberg Laserwriter
	8	1x1 write setting at 40mW, 50% dose
Develop/Post-Bake	9	1 min. develop with MF-319 developer w/ DI water rinse
	10	12 min. post bake at 120°C
Etch in BOE	11	2 min. etch intervals w/ rinsing and imaging between
Resist Strip	12	10-20min O_2 plasma clean in dedicated O_2 plasma cleaner

Table A.4: Procedure outline for undercutting silicon devices on SOI

The undercut process workflow is indicated in Table A.4. The general challenge with a BOE etch masked by resist is that the BOE can attack the resist and peel it off of your sample, making the etch spread uncontrollably across the sample. To combat this, I advise you to focus on the the following points:

- Make sure the surface is clean, dry and hydrophilic for good surface adhesion
- For more delicate structures, you may be able to brace the structure with patterning supports in the photoresist, this can help prevent device breakage
- After development, make sure the post-bake is sufficient for hardening the resist
- Initially etch and rinse in small intervals to check the process
- As you gain confidence in the process, feel free to increase the etch time to get deeper undercuts

To give some more detail and intuition about each step in the process I will elaborate on each step in Table A.4:

(Surface Preparation) Surface preparation revolves around properly preparing the surface of the chip for strong adhesion to the photoresist. Any weakness in this adhesion will dramatically reduce the quality and selectivity of your etch. This is due to the tendency for BOE to attack the resist and peel it off while simultaneously etching the sample. To properly prepare the sample, there are three steps which I suggest for surface preparation:

1. Remove large particulates with an Acetone/IPA clean. I recommend a 2 min. acetone bath in a sonicator followed by an immediate transfer to an IPA bath. To finish this off I suggest an IPA rinse and nitrogen blow-dry.

2. Clean off remaining organics and create a thin oxide using an O_2 plasma clean.

3. Heat the sample to evaporate any surface adsorbed water. If adsorbed water is still a concern, this temperature or time can be increased.

(Spin/Bake) The spin/bake steps work to coat the sample in a uniform layer of resist and prepare the resist for exposure by baking it. After the sample has cooled down from the water evaporation process in **(Surface Preparation)**, center the chip on the spin coater and follow the standard spin/bake recipe for S1813 resist used at VINSE. The parameters of this are listed in Table A.4.

(Pattern) The pattern step involves locally aligning the photolithography tool (in this case the Heidelberg laserwriter) with your sample so the desired regions can be exposed for the undercut. This exposure is specified by a GDS file that will be prepared prior to entering the cleanroom and loaded for exposure. For this GDS file, I recommend simply adding a new layer to the original GDS file used to define the silicon devices (whatever you used for fab at ORNL) so you can overlay the undercut windows. When importing the GDS file into the laserwriter, you can then choose this new undercut window layer to extract. To do the local alignment, I recommend following the

standard operating procedures for the tool kept by the VINSE cleanroom. The dosage and write settings I used for work on SOI are included in Table A.4. These dose setting definitions are a bit ambiguously defined by the Heidelberg manual, but the 1x1 setting refers to each raster only having 1 pass with a 1x slowdown. Other settings can multiply the number of passes and slowdown to produce smoother shapes. I believe the % dose has to do with the laser pulse width, higher gives more exposure energy. The power setting is the laser power.

(Develop/Post Bake) The develop/post-bake step involves developing the pattern exposed in **(Pattern)** and hardening the resist to prevent peeling in the BOE etch. The recipe recommendations for this are given in Table A.4. It is important after the develop step to image your sample to ensure the patterns printed properly. If the sample printed properly, follow up the development with a post-exposure bake. This post-bake smooths out side-walls in the resist and hardens the resist to be more resilient against the BOE. If there is a misprint, the best procedure is to strip the sample with an O_2 clean and start again from **(Spin/Bake)**. However, if the sample misprinted far enough from the desired area and no developer came into contact with the silicon in the desired undercut window location, you may be able to get away with re-exposing the sample as is and running another develop. Re-expose like this at your own risk.

(Etch in BOE) The etch in BOE works to remove the buried oxide layer to suspend the silicon device. If all of the sample preparation steps before this etch worked properly, the BOE etch should not peel off the resist and will remove the oxide in a controlled way. You can quickly tell the oxide is peeling by running the etch in small segments, rinsing and imaging between each step. If you observe non-uniformly spreading discoloration across the sample, this means the resist is peeling and the etch is uncontrolled. A controlled etch is shown in Fig. A.4 and Fig. A.5.

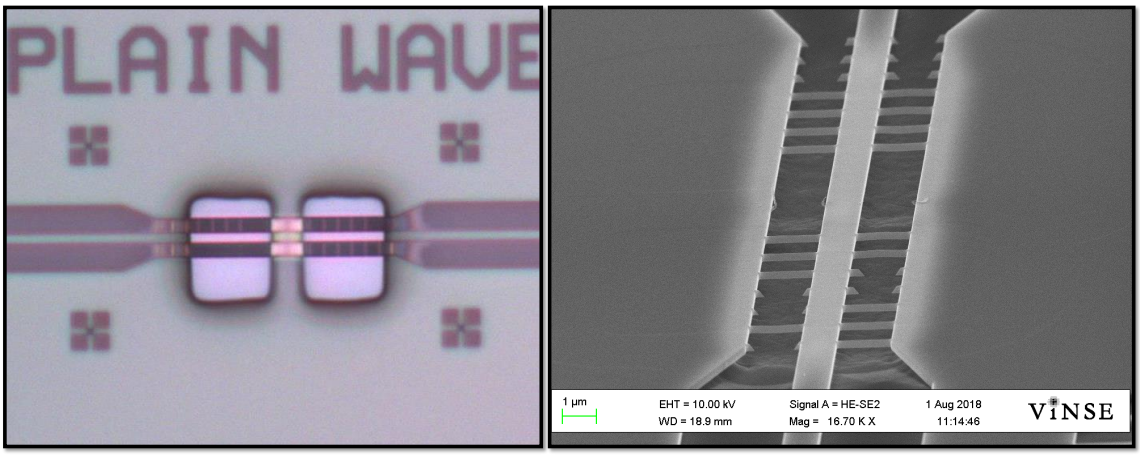

Figure A.4: Images of an undercut on a plain waveguide in both an optical microscope (left) and SEM (right). The optical microscope image shows the device under photoresist. The spread of the etch after 8 minutes of total etch time can be seen to the left and right of the resist windows. The SEM image shows the undercut in greater detail. An oxide ridge in the middle of the device can be observed in this SEM, demonstrating the etch was strongly controlled by the resist mask.

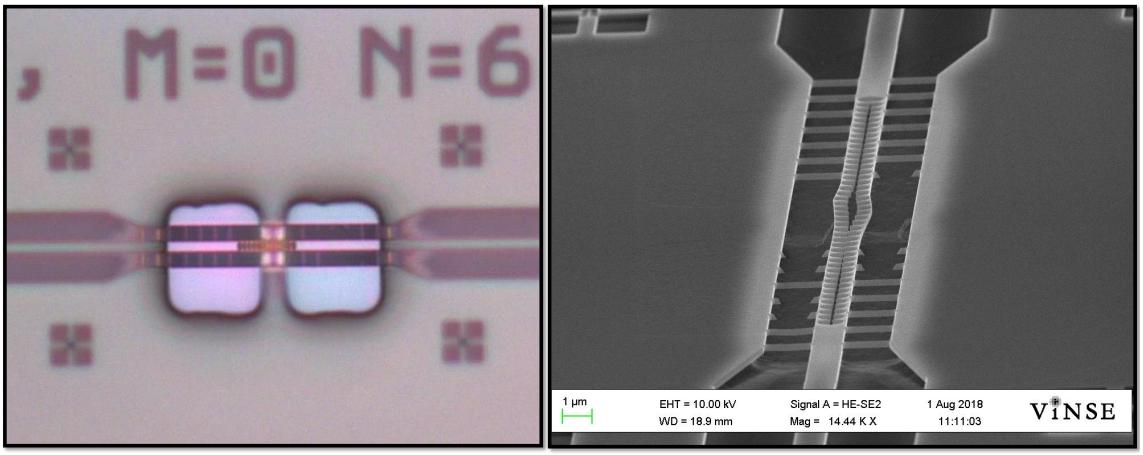

Figure A.5: Images of an undercut on pinched waveguide cavities in both an optical microscope (left) and SEM (right). The optical microscope image shows a device under photoresist. The spread of the etch after 8 minutes of total etch time can be seen to the left and right of the resist windows. The SEM image shows the undercut in greater detail. An oxide ridge in the middle of the device can be observed in this SEM, demonstrating the etch was strongly controlled by the resist mask. The bending of the device due to the process and device flexibility can be readily seen.

This etch was executed in 2 minute intervals with a total etch time of 8 minutes. It can be seen in these figures that the discoloration spreads uniformly away from the etch window, indicating the etch is unable to peel off the resist. Now at this point, you're likely wondering why the etch is not spreading uncontrollably, even though the silicon surface has been coated in a thin oxide from the O_2 plasma clean, which the BOE should handily etch away. It is my belief that due to how thin this oxide layer is ($<$ 1nm), surface forces prevent the BOE solution from infiltrating and etching between the silicon and the resist. It can even be seen that due to the resist strip placed in the middle of the device that an oxide ridge is present in the SEM and microscope images, demonstrating the etch was controlled by the resist mask.

(Resist Strip) The resist strip step works to clear the photoresist from the sample. For this step, I opted to run a dry resist strip, as a wet resist strip can often damage delicate structures from nanoscale forces due to evaporation and fluid motion. It should be mentioned that critical point drying (CPD) was explored to reduce device strain, but ultimately the dry resist strip showed greater device survival rates. It can be seen in Fig. A.5 that while the extremely flexible pinched waveguide has been stretched out by the overall process, it remains intact after resist stripping. For context on how delicate these pinched waveguides are, it is possible to break suspended pinched waveguides by simply charging them up from looking at them too long in the SEM. A video of one such device flexing from charging can be found at **https://www.youtube.com/watch?v=f3GJ1l7B7VM**.

BIBLIOGRAPHY

[1] R. Dewan, V. Jovanov, S. Hamraz, and D. Knipp, "Analyzing periodic and random textured silicon thin film solar cells by rigorous coupled wave analysis," Scientific Reports **4**, 6029 (2014).

[2] C. Battaglia, C. Hsu, K. Soderstrom, J. Escarre, F. Haug, M. Charriere, M. Boccard, M. Despeisse, D. T. L. Alexander, M. Cantoni, Y. Cui, and C. Ballif, "Light trapping in solar cells: can periodic beat random?" ACS Nano **6**, 2790–2797 (2012).

[3] G. K. Shirmanesh, R. Sokhoyan, R. A. Pala, and H. A. Atwater, "Dual-gated active metasurface at 1550 nm with wide $(> 300^{\circ})$ phase tunability," Nano Letters **18**, 2957–2963 (2018).

[4] W. Zhang, L. Huang, C. Santschi, and O. J. F. Martin, "Trapping and sensing 10 nm metal nanoparticles using plasmonic dipole antennas," Nano Letters **10**, 1006–1011 (2010).

[5] S. Mandal, X. Serey, and D. Erickson, "Nanomanipulation using silicon photonic crystal resonators," Nano Letters **10**, 99–104 (2010).

[6] Q. Ouyang, S. Zeng, L. Jiang, L. Hong, G. Xu, X. Q. Dinh, J. Qian, S. He, J. Qu, P. Coquet, and K. T. Yong, "Sensitivity enhancement of transition metal dichalcogenides/silicon nanostructure-based surface plasmon resonance biosensor," Scientific Reports **6**, 28190 (2016).

[7] J. Valentine, J. Li, T. Zentgraf, G. Bartal, and X. Zhang, "An optical cloak made of dielectrics," Nature Materials **8**, 568–571 (2009).

[8] D. Schurig, J. J. Mock, B. J. Justice, S. A. Cummer, J. B. Pendry, A. F. Starr, and D. R. Smith, "Metamaterial electromagnetic cloak at microwave frequencies," Science **10**, 977–980 (2006).

[9] D. Lu and Z. Liu, "Hyperlenses and metalenses for far-field super-resolution imaging," Nature Communications **3**, 1205 (2012).

[10] M. Khorasaninejad, W. T. Chen, R. C. Devlin, J. Oh, A. Y. Zhu, and F. Capasso, "Metalenses at visible wavelengths: Diffraction-limited focusing and subwavelength resolution imaging," Science **352**, 1990–1994 (2016).

[11] T. F. Oulton, V. J. Sorger, T. Zentgraf, R.-M. Ma, C. Gladden, L. Dai, G. Bartal, and X. Zhang, "Plasmon lasers at deep subwavelength scale," Nature **461**, 629–632 (2009).

[12] Y. Zhang, M. Khan, Y. Huang, J. Ryou, P. Deotare, R. Dupuis, and M. Loncar, "Photonic crystal nanobeam lasers," Applied Physics Letters **97**, 051104 (2010).

[13] R. Leijssen and E. Verhagen, "Strong optomechanical interactions in a sliced photonic crystal nanobeam," Scientific Reports **5**, 15974 (2015).

[14] F. Monifi, J. Zhang, S. K. Ozdemir, B. Peng, Y. Liu, F. Bo, F. Nori, and L. Yang, "Optomechanically induced stochastic resonance and chaos transfer between optical fields," nature photonics **10**, 399–405 (2016).

[15] A. P. Raman, M. A. Anoma, L. Zhu, E. Rephaeli, and S. Fan, "Passive radiative coolilng below ambient air temperature under direct sunlight," Nature **515**, 540–544 (2014).

[16] E. Rephaeli, A. Raman, and S. Fan, "Ultrabroadband photonic structures to achieve high-performance daytime radiative cooling," Nano Letters **13**, 1457–1461 (2013).

[17] T. Asano, Y. Ochi, Y. Takahashi, K. Kishimoto, and S. Noda, "Photonic crystal nanocavity with a Q factor exceeding eleven million," Optics Express **25**, 1769–1777 (2017).

[18] M. Minkov, V. Savona, and D. Gerace, "Photonic crystal slab cavity simultaneously optimized for ultra-high Q/V and vertical radiation coupling," Applied Physics Letters **111**, 131104 (2017).

[19] P. Seidler, K. Lister, U. Drechsler, J. Hofrichter, and T. Stoferle, "Slotted photonic crystal nanobeam cavity with an ultrahigh quality factor-to-mode volume ratio," Optics Express **21**, 32468–32483 (2013).

[20] S. Hu, M. Khater, R. Salas-Montiel, E. Kratschmer, S. Engelmann, W. M. J. Green, and S. M. Weiss, "Experimental realization of deep subwavelength confinement in dielectric optical resonators," Science Advances **4**, eaat2355 (2018).

[21] A. J. Bett, J. Eisenlohr, O. Hohn, P. Repo, H. Savin, B. Blasi, and J. C. Goldschmidt, "Wave optical simulation of the light trapping properties of black silicon surface textures," Optics Express **24**, A434–A445 (2016).

[22] Z. Zhang, L. Zhang, M. N. Hedhili, H. Zhang, and P. Wang, "Plasmonic gold nanocrystals coupled with photonic crystal seamlessly on tio2 nanotube photoelectrodes for efficient visible light photoelectrochemical water splitting," Nano Letters **13**, 14–20 (2013).

[23] C. T. Phare, Y. D. Lee, J. Cardenas, and M. Lipson, "Graphene electro-optic modulator with 30 GHz bandwidth," Nature Photonics **9**, 511–515 (2015).

[24] C. Wang, M. Zhang, B. Stern, M. Lipson, and M. Loncar, "Nanophotonic lithium niobate electro-optic modulators," Optics Express **26**, 1547–1555 (2018).

[25] M. A. Bandres, S. Wittek, G. Harari, M. Parto, J. Ren, M. Segev, D. N. Christodoulides, and M. Khajavikhan, "Topological insulator laser: Experiments," Science **359**, 1231 (2018).

[26] M. J. Burek, Y. Chu, M. S. Z. Liddy, P. Patel, J. Rochman, S. Meesala, W. Hong, Q. Quan, M. D. Lukin, and M. Loncar, "High quality-factor optical nanocavities in bulk single-crystal diamond," Nature Communications **5**, 5718 (2014).

[27] E. M. Purcell, "Spontaneous emission probabilities at radio frequencies," Physical Review **69**, 681 (1946).

[28] P. T. Kristensen, C. V. Vlack, and S. Hughes, "Generalized effective mode volume for leaky optical cavities," Optics Letters **37**, 1649–1651 (2012).

[29] E. A. Muljarov and W. Langbein, "Exact mode volume and Purcell factor of open optical systems," Physical Review B **94**, 235438 (2016).

[30] K. Qin, S. Hu, S. T. Retterer, I. I. Kravchenko, and S. M. Weiss, "Slow light Mach-Zehnder interferometer as label-free biosensor with scalable sensitivity," Optics Letters **41**, 753–756 (2016).

[31] N. Gutman, W. H. Dupree, Y. Sun, A. A. Sukhorukov, and C. M. de Sterke, "Frozen and broadband slow light in coupled periodic nanowire waveguides," Optics Express **20**, 3519–3528 (2012).

[32] C. Lin, X. Wang, S. Chakravarty, B. S. Lee, W. Lai, J. Luo, A. K.-Y. Jen, and R. T. Chen, "Electro-optic polymer infiltrated silicon photonic crystal slot waveguide modulator with 23 dB slow light enhancement," Applied Physics Letters **97**, 093304 (2010).

[33] F. Qiu, A. M. Spring, D. Maeda, M. Ozawa, K. Odoi, A. Otomo, I. Aoki, and S. Yokoyama, "A hybrid electro-optic polymer and TiO2 double-slot waveguide modulator," Scientific Reports **5**, 8561 (2015).

[34] A. H. J. Yang, S. D. Moore, B. S. Schmidt, M. Klug, M. Lipson, and D. Erickson, "Optical manipulation of nanoparticles and biomolecules in sub-wavelength slot waveguides," Nature **457**, 71–75 (2018).

[35] A. Densmore, D.-X. Xu, S. Janz, P. Waldron, T. Mischki, G. Lopinski, A. Delâge, J. Lapointe, P. Cheben, B. Lamontagne, and J. H. Schmid, "Spiral-path high-sensitivity silicon photonic wire molecular sensor with temperature-independent response," Optics letters **33**, 596– (2008).

[36] L. Lu, J. D. Joannopoulos, and M. Soljacic, "Topological photonics," Nature Photonics **8**, 821–829 (2014).

[37] M. R. Foreman, J. D. Swaim, and F. Vollmer, "Whispering gallery mode sensors," Advances in Optics and Photonics **7**, 168–240 (2015).

[38] M. L. Povinelli, S. G. Johnson, M. Loncar, M. Ibanescu, E. J. Smythe, F. Capasso, and J. D. Joannopoulos, "High-Q enhancement of attractive and repulsive optical forces between coupled whispering-gallery-mode resonators," Optics Express **13**, 8286–8295 (2005).

[39] T. J. Kippenberg, S. M. Spillane, and K. J. Vahala, "Demonstration of ultra-high-Q small mode volume toroid microcavities on a chip," Applied Physics Letters **85**, 6113–6115 (2004).

[40] X.-F. Jiang, C.-L. Zou, L. Wang, Q. Gong, and Y.-F. Xiao, "Whispering-gallery microcavities with unidirectional laser emission," Laser and Photonics Reviews **10**, 40–61 (2016).

[41] K. A. Willets and R. P. V. Duyne, "Localized surface plasmon resonance spectroscopy and sensing," Annual Review of Physical Chemistry **58**, 267–297 (2007).

[42] J. Becker, A. Trugler, A. Jakab, U. Hohenester, and C. Sonnichsen, "The optimal aspect ratio of gold nanorods for plasmonic bio-sensing," Plasmonics **5**, 161–167 (2010).

[43] X. Yu, L. Shi, D. Han, J. Zi, and P. V. Braun, "High quality factor metallodielectric hybrid plasmonic-photonic crystals," Advanced Functional Materials **20**, 1910–1916 (2010).

[44] W. Li, Z. J. Coppens, L. V. Besteiro, W. Wang, A. O. Govorov, and J. Valentine, "Circularly polarized light detection with hot electrons in chiral plasmonic metamaterials," Nature Communications **6**, 8379 (2015).

[45] J. D. Joannopoulos, S. G. Johnson, J. N. Winn, and R. D. Meade, *Photonic Crystals: Molding the Flow of Light* (Princeton University Press, 2008), 2nd ed.

[46] Y. Akahane, T. Asano, B. S. Song, and S. Noda, "High-Q photonic nanocavity in a two-dimensional photonic crystal," Nature **425**, 944–947 (2003).

[47] D. Yang, C. Wang, and Y. Ji, "Silicon on-chip 1d photonic crystal nanobeam bandstop filters for parallel multiplexing of ultra-compact integrated sensor array," Optics Express **24**, 16267 (2016).

[48] X. Ge, Y. Shi, and S. He, "Ultra-compact channel drop filter based on photonic crystal nanobeam cavities utilizing a resonant tunneling effect," Optics Letters **39**, 6973–6976 (2014).

[49] C. Husko, A. D. Rossi, S. Combrie, Q. V. Tran, F. Raineri, and C. W. Wong, "Ultrafast all-optical modulation in gaas photonic crystal cavities," Applied Physics Letters **94**, 021111 (2009).

[50] Y. A. Vlasov, M. O'Boyle, H. F. Hamann, and S. J. McNab, "Active control of slow light on a chip with photonic crystal waveguides," Nature **438**, 65–69 (2005).

[51] S. Mandal and D. Erickson, "Nanoscale optofluidic sensor arrays," Optics Express **16**, 1623–1631 (2008).

[52] P. Yu, H. Qiu, H. Yu, F. Wu, Z. Wang, Z. Jian, and J. Yang, "High-Q and high-order side-coupled air-mode nanobeam photonic crystal cavities in silicon," IEEE Photonics Technology Letters **28**, 2121–2124 (2016).

[53] Y. Halioua, A. Bazin, P. Monnier, T. J. Karle, G. Roelkens, R. R. I. Sagnes, and F. Raineri, "Hybrid III-V semiconductor/silicon nanolaser," Optics Express **19**, 9221–9231 (2011).

[54] S. Hu and S. M. Weiss, "Design of photonic crystal cavities for extreme light concentration," ACS Photonics **3**, 1647–1653 (2016).

[55] P. B. Deotare, M. W. McCutcheon, I. W. Frank, M. Khan, and M. Loncar, "High quality factor photonic crystal nanobeam cavities," Applied Physics Letters **94**, 121106 (2009).

[56] K. Schneider and P. Seidler, "Strong optomechanical coupling in a slotted photonic crystal nanobeam cavity with an ultrahigh quality factor-to-mode volume ratio," Optics Express **24**, 13850–13865 (2016).

[57] Q. Quan, D. L. Floyd, I. B. Burgess, P. B. Deotare, I. W. Frank, S. K. Y. Tang, R. Ilic, and M. Loncar, "Single particle detection in cmos compatible photonic crystal nanobeam cavities," Optics Express **21**, 32225–32233 (2013).

[58] J. D. Ryckman and S. M. Weiss, "Low mode volume slotted photonic crystal single nanobeam cavity," Applied Physics Letters **101**, 071104 (2012).

[59] R. Leijssen, G. R. L. Gala, L. Freisem, J. T. Muhonen, , and E. Verhagen, "Nonlinear cavity optomechanics with nanomechanical thermal fluctuations," Nature Communications **8**, 16024 (2017).

[60] X. Zhang, G. Zhou, P. Shi, H. Du, T. Lin, J. Teng, and F. S. Chau, "On-chip integrated optofluidic complex refractive index sensing using silicon photonic crystal nanobeam cavities," Optics Letters **41**, 1197–1200 (2016).

[61] Q. Quan and M. Loncar, "Deterministic design of wavelength scale, ultra high Q photonic crystal nanobeam cavities," Optics Express **19**, 18529–18542 (2011).

[62] F. O. Afzal, S. I. Halimi, and S. M. Weiss, "Efficient side-coupling to photonic crystal nanobeam cavities via state-space overlap," Journal of the Optical Society of America B **36**, 585 (2019).

[63] A. H. Safavi-Naeini, S. Groblacher, J. T. Hill, J. Chan, M. Aspelmeyer, and O. Painter, "Squeezed light from a silicon micromechanical resonator," Nature **500**, 185–189 (2013).

[64] C. Renaut, B. Cluzel, J. Dellinger, L. Lalouat, E. Picard, D. Peyrade, E. Hadji, and F. de Fornel, "On chip shapeable optical tweezers," Scientific Reports **3**, 2290 (2013).

[65] C. Wang, Q. Quan, S. Kita, Y. Li, and M. Loncar, "Single-nanoparticle detection with slot-mode photonic crystal cavities," Applied Physics Letters **106**, 261105 (2015).

[66] M. Kuttge, F. J. G. de Abajo, and A. Polman, "Ultrasmall mode volume plasmonic nanodisk resonators," Nano Letters **10**, 1537–1541 (2010).

[67] M. Galli, S. L. Portalupi, M. Belotti, L. C. Andreani, L. O'Faolain, and T. F. Krauss, "Light scattering and Fano resonances in high-Q photonic crystal nanocavities," Applied Physics Letters **94**, 071101 (2009).

[68] K. Li, J. Li, Y. Song, G. Fang, C. Li, Z. Feng, R. Su, B. Zeng, X. Wang, and C. Jin, "L_n slot photonic crystal microcavity for refractive index gas sensing," IEEE Photonics Journal **6**, 6802509 (2009).

[69] Y. Chen, W. S. Fegadolli, W. M. Jones, A. Scherer, and M. Li, "Ultrasensitive gas-phase chemical sensing based on functionalized photonic crystal nanobeam cavities," ACS Nano **8**, 522–527 (2014).

[70] P. Liu and Y. Shi, "Simultaneous measurement of refractive index and temperature using cascaded side-coupled photonic crystal nanobeam cavities," Optics Express **25**, 28398–28406 (2017).

[71] Z. Meng, A. Liang, and Z. Li, "Fano resonances photonic crystal nanobeams side-coupled with nanobeam cavities," Journal of Applied Physics **121**, 193102 (2017).

[72] P. Yu, T. Hu, H. Qiu, F. Ge, H. Yu, X. Jiang, and J. Yang, "Fano resonances in ultracompact waveguide Fabry-Perot resonator side-coupled lossy nanobeam cavities," Applied Physics Letters **103**, 091104 (2013).

[73] T. Lin, F. S. Chau, J. Deng, and G. Zhou, "Dynamic control of the asymmetric Fano resonance in side-coupled Fabry-Perot and photonic crystal nanobeam cavities," Applied Physics Letters **107**, 223105 (2015).

[74] A. Yariv, "Universal relations for coupling optical power between microresonators and dielectric waveguides," Electronics Letters **36**, 321–322 (2000).

[75] P. E. Barclay, K. Srinivasan, and O. Painter, "Design of photonic crystal waveguides for evanescent coupling to optical fiber tapers and integration with high-Q cavities," Journal of the Optical Society of America B **20**, 2274–2284 (2003).

[76] Y. Xu, Y. Li, R. K. Lee, and A. Yariv, "Scattering-theory analysis of waveguide-resonator coupling," Physical Review E **62**, 7389–7404 (2000).

[77] G. Cronier, D. Sanchez, A. Bazin, P. Monnier, S. Bouchoule, R. Braive, G. Beaudoin, I. Sagnes, R. Raj, and F. Raineri, "High Q factor InP photonic crystal nanobeam cavities on silicon wire waveguides," Optics Letters **41**, 579–582 (2016).

[78] Q. Quan, P. B. Deotare, and M. Loncar, "Photonic crystal nanobeam cavity strongly coupled to the feeding waveguide," Applied Physics Letters **96**, 203102 (2010).

[79] F. O. Afzal, J. M. Petrin, and S. M. Weiss, "Camera detection and modal fingerprinting of photonic crystal nanobeam resonances," Optics Express **27**, 14623 (2019).

[80] G. Crosnier, D. Sanchez, S. Bouchoule, P. Monnier, G. Beaudoin, I. Sagnes, R. Raj, and F. Raineri, "Hybrid indium phosphide-on-silicon nanolaser diode," Nature Photonics **11**, 297–300 (2017).

[81] B. J. M. Hasumann, B. J. Shields, Q. Quan, Y. Chu, N. P. de Leon, R. Evans, M. J. Burek, A. S. Zibrov, M. Markham, D. J. Twitchen, H. Park, M. D. Lukin, and M. Loncar, "Coupling of NV centers to photonic crystal nanobeams in diamond," Nano Letters **13**, 5791–5796 (2013).

[82] J. W. Silverstone, R. Santagati, D. Bonneau, M. J. Stain, M. Sorel, J. L. O'Brien, and M. G. Thompson, "Qubit entanglement between ring-resonator photon-pair sources on a silicon chip," Nature Communications **6**, 7948 (2015).

[83] D. Kleckner, B. Pepper, E. Jeffrey, P. Sonin, S. M. Thon, and D. Bouwmeester, "Optomechanical trampoline resonators," Optics Express **19**, 19708–19716 (2011).

[84] V. I. Belotelov, A. N. Kalish, A. K. Zvezdin, A. V. Gopal, and A. S. Vengurlekar, "Fabry-Perot plasmonic structures for nanophotonics," Journal of the Optical Society B **29**, 294–299 (2012).

[85] S. I. Halimi, S. Hu, F. O. Afzal, and S. M. Weiss, "Realizing high transmission intensity in photonic crystal nanobeams using a side-coupling waveguide," Optics Letters **43**, 4260–4263 (2018).

[86] J. Wang, Z. Yao, T. Lei, and A. W. Poon, "Silicon coupled-resonator optical-waveguide-based biosensors using light-scattering pattern recognition with pixelized mode-field-intensity distributions," Scientific Reports **4**, 7528 (2014).

[87] M. L. Cooper, G. Gupta, J. S. Park, M. Schneider, I. B. Divliansky, and S. Mookherjea, "Quantitative infrared imaging of silicon-on-insulator microring resonators," Optics Letters **35**, 784–786 (2010).

[88] J. Topolancik, F. Vollmer, R. Ilic, and M. Crescimanno, "Out-of-plane scattering from vertically asymmetric photonic crystal slab waveguides with in-plane disorder," Optics Express **17**, 12470–12480 (2009).

[89] R. Shankar, R. Leijssen, I. Bulu, and M. Loncar, "Mid-infrared photonic crystal cavities in silicon," Optics Express **19**, 5579–5586 (2011).

[90] J. Sun, E. Timurdogan, A. Yaacobi, E. S. Hosseini, and M. R. Watts, "Large-scale nanophotonic phased array," Nature **493**, 195–199 (2013).

[91] A. Taflove and S. C. Hagness, *Computational Electrodynamics: The Finite-Difference Time-Domain Method* (Artech House, 2005), 3rd ed.

[92] C. Zhao, Q. Yuan, L. Fang, X. Gan, and J. Zhao, "High-performance humidity sensor based on a polyvinyl alcohol-coated photonic crystal cavity," Optics Letters **41**, 5515–5518 (2016).

[93] A. Casas-Bedoya, S. Shahnia, D. D. Battista, E. Magi, and B. J. Eggleton, "Chip scale humidity sensing based on a microfluidic infiltrated photonic crystal," Applied Physics Letters **103**, 181109 (2013).

[94] F. O. Afzal, Y. Bian, B. Peng, S. Hu, A. Aboketaf, K. Dezfulian, K. Nummy, A. Stricker, C. Hedges, Z. Sowinski, M. Rakowski, W. S. Lee, R. Augur, D. Riggs, K. Giewont, and S. M. Weiss, "O-band subwavelength grating filters in a monolithic photonics technology," IEEE Photonics Technology Letters **32**, 1–1 (2020).

[95] J. St-Yves, S. Larochelle, and W. Shi, "O-band silicon photonic Bragg-grating multiplexers using UV lithography," in "2016 Optical Fiber Communications Conference and Exhibition (OFC)," (2016), pp. 1–3.

[96] H. Yun, M. Hammood, S. Lin, L. Chrostowski, and N. A. F. Jaeger, "Broadband flat-top SOI add–drop filters using apodized sub-wavelength grating contradirectional couplers," Optics Letters (2019).

[97] B. Naghdi and L. R. Chen, "Silicon photonic contradirectional couplers using subwavelength grating waveguides," Optics Express **24**, 23429–23438 (2016).

[98] B. Naghdi and L. R. Chen, "Spectral engineering of subwavelength-grating-based contradirectional couplers," Optics Express (2017).

[99] D. Charron, J. St-Yves, O. Jafari, S. LaRochelle, and W. Shi, "Subwavelength-grating contradirectional couplers for large stopband filters," Optics Letters **43**, 895 (2018).

[100] B. Naghdi and L. R. Chen, "Silicon Photonic Four-Channel Optical Add-Drop Multiplexer Enabled by Subwavelength Grating Waveguides," IEEE Photonics Journal **10**, 1–10 (2018).

[101] W. Shi, X. Wang, C. Lin, H. Yun, Y. Liu, T. Baehr-Jones, M. Hochberg, N. A. F. Jaeger, and L. Chrostowski, "Silicon photonic grating-assisted, contra-directional couplers," Optics Express **21**, 3633 (2013).

[102] H. Qiu, J. Jiang, P. Yu, D. Mu, J. Yang, X. Jiang, H. Yu, R. Cheng, and L. Chrostowski, "Narrow-Band Add-Drop Filter Based on Phase-Modulated Grating-Assisted Contra-Directional Couplers," Journal of Lightwave Technology **36**, 3760–3764 (2018).

[103] M. Hammood, A. Mistry, H. Yun, M. Ma, L. Chrostowski, and N. A. F. Jaeger, "Four-channel, Silicon Photonic, Wavelength Multiplexer-Demultiplexer With High Channel Isolations," (2020).

[104] D. A. Miller, "Optical interconnects to electronic chips," Applied Optics **49**, F59–F70 (2010).

[105] X. Zhou, R. Urata, and H. Liu, "Beyond 1 Tb/s Intra-Data Center Interconnect Technology: IM-DD OR Coherent?" Journal of Lightwave Technology **38**, 475–484 (2020).

[106] K. Giewont, K. Nummy, F. A. Anderson, J. Ayala, T. Barwicz, Y. Bian, K. K. Dezfulian, D. M. Gill, T. Houghton, S. Hu, B. Peng, M. Rakowski, S. R. Iii, J. C. Rosenberg, A. Sahin, I. Stobert, and A. Stricker, "300-mm Monolithic Silicon Photonics Foundry Technology," IEEE Journal of Selected Topics in Quantum Electronics **25** (2019).

[107] P. Dong, "Silicon photonic integrated circuits for wavelength-division multiplexing applications," IEEE Journal on Selected Topics in Quantum Electronics **22**, 370–378 (2016).

[108] C. Sciancalepore, R. J. Lycett, J. A. Dallery, S. Pauliac, K. Hassan, J. Harduin, H. Duprez, U. Weidenmueller, D. F. G. Gallagher, S. Menezo, and B. Ben-Bakir, "Low-crosstalk fabrication-insensitive echelle grating multiplexers and passives for the silicon photonics toolbox," in "Integrated Optics: Devices, Materials, and Technologies XIX," (2015).

[109] S. Dwivedi, P. De Heyn, P. Absil, J. Van Campenhout, and W. Bogaerts, "Coarse wavelength division multiplexer on silicon-on-insulator for 100 GbE," in "IEEE International Conference on Group IV Photonics GFP," , vol. 2015-Octob (IEEE Computer Society, 2015), vol. 2015-Octob, pp. 9–10.

[110] M. Teng, S. Fathpour, R. Safian, L. Zhuang, A. Honardoost, Y. Alahmadi, S. S. Polkoo, K. Kojima, H. Wen, C. K. Renshaw, P. Likamwa, and G. Li, "Miniaturized Silicon Photonics Devices for Integrated Optical Signal Processors," Journal of Lightwave Technology **38** (2020).

[111] E. W. Ong, T. Wallner, N. M. Fahrenkopf, and D. D. Coolbaugh, "High positional freedom SOI subwavelength grating coupler (SWG) for 300 mm foundry fabrication," Optics Express (2018).

[112] D. Vermeulen, S. Selvaraja, P. Verheyen, G. Lepage, W. Bogaerts, P. Absil, D. Van Thourhout, and G. Roelkens, "High-efficiency fiber-to-chip grating couplers realized using an advanced CMOS-compatible Silicon-On-Insulator platform," Optics Express **18**, 18278 (2010).

[113] C. Meagher, Z. Sowinski, C. Yu, S. Hu, K. Nummy, M. M. Ghosal, R. Viswanathan, A. Abdo, and T. Wiltshire, "Patterning challenges for monolithic silicon photonics: AP/DFM: Advanced patterning / design for manufacturability," in "2018 29th Annual SEMI Advanced Semiconductor Manufacturing Conference, ASMC 2018," (Institute of Electrical and Electronics Engineers Inc., 2018), pp. 155–158.